Deformation of Cohesive Granular Materials: Micro influences Macro

Hao Shi

DEFORMATION OF COHESIVE GRANULAR MATERIALS: MICRO INFLUENCES MACRO

Hao Shi

Thesis committee members:

Chair:
Prof.dr. G. P. M. R. Dewulf,   University of Twente

Promotor:
Prof.dr.rer.-nat. S. Luding,   University of Twente

Co-promotor:
Dr. V. Magnanimo,   University of Twente

Commission:
Prof.dr.ir. R. M. van der Meer,   University of Twente
Dr. M. H. G. Duits,   University of Twente
Prof. J. R. van Ommen,   Delft University of Technology
Prof. dr.-ing. A. Kwade,   Technical University of Braunschweig
Prof. J. Y. Ooi,   University of Edinburgh

Deformation of Cohesive Granular Materials: Micro influences Macro

DISSERTATION

to obtain
the degree of doctor at the University of Twente,
on the authority of the rector magnificus,
Prof.dr. T.T.M. Palstra,
on account of the decision of the graduation committee,
to be publicly defended
on Wednesday 3rd April 2019 at 16:45 hrs

by

Hao Shi
born on the 25th May 1989
in Donghai, China.

This dissertation was approved by the promotor:

Prof.dr.rer.-nat. S. Luding

and the co-promotor:

Dr. V. Magnanimo

To my beloved family.

CONTENTS

SUMMARY

Granular materials and particulate matter display interesting bulk behaviors from static to dynamic, solid to liquid or gas like states: sand can be compressed and behave like a solid, or flow in a slurry like a liquid or fly in the air as a sand storm. The mystery of bridging the gap between the particulate, microscopic state and the macroscopic, continuum description is one of the challenges of modern research.

Powders is a special class of granular materials that contain very fine particles that may flow freely when shaken or tilted, but may stick when left at rest or being compressed. During storage and transportation processes, the material undergoes various modes of deformation and stress conditions, e.g. due to compression or shear. In many applications, it is important to know when powders are yielding, i.e., when they start to flow under shear; in other cases it is necessary to know how much stress is needed to keep them flowing. The flow behaviour changes dramatically from very low to very high stress conditions.

The main focus of this thesis is to investigate how the micro-mechanical properties influence the macroscopic bulk responses of granular materials and it is structured as two parts: the former one devoted to laboratory experiments and the latter one to numerical simulations. The focuses of the first part are (i) characterization of granular materials at different length scales, for both dry non-cohesive and cohesive materials, (ii) investigate the flow behaviour in both low and high stress regimes using the same materials, (iii) explore different testing devices to identify the most appropriate techniques on powder flow measurement. While the focus of second part is (iv) the development of the constitutive model to describe granular flows based on micro-mechanical insights from discrete particle simulations.

In the first part of the study, we perform a wide and systematic experimental investigation to assess the influences of particle size and inter-particle cohesion on powder flows at various stress regimes. We choose limestone powders as a reference material because of its insensitivity to the environmental change through the whole study. Initially, we investigate the effect of particle size on limestone powder yielding in low to moderate stress regimes and we found an interesting non-monotonic trend of bulk friction and cohesive strength due to the interplay between inter-particle cohesion and geometrical interlocking. We also propose a simple empirical model based on van der Waals interaction to describe the behaviour of cohesive strength.

Next, we further enter the high stress regime by compacting our powders at high loads, and investigate the effect of particle size on the powder compaction and the tensile strength of the final tablet. The geometrical influence which dominates at low stress regime are found to be irrelevant at high pressure regime. Finally, we try to bridge the limit of different dynamic and quasi-static flow tests at low towards zero confining pres-

sure and found a good agreement between these two types of test. This novel approach gives access to a stress regime normally forbidden to conventional shear cell experiments.

In the second part of this study, instead of simulating each single case as presented in the first part, we aim on finding a good generalized rheological model with the help of discrete particle simulations (DPM) to describe different types of granular flow under various conditions. We first give an overview of recent progress and some new insights about the collective mechanical behavior of granular, deformable particles from diluted to jammed states. Then we systematically investigate the interplay between inter-particle friction and cohesion on sheared homogeneous and inhomogeneous granular media at steady state and therefore extend our rheological model towards a more generalized description.

SAMENVATTING

Granulaire en uit deeltjes bestaande materialen vertonen interessant bulk gedrag. Variërend van statisch tot dynamisch, vast tot vloeistof en gas toestand, kan zand bijvoorbeeld worden samengedrukt en zich gedragen als een solide materiaal, stromen in een slurry als een vloeistof, of door de lucht te vliegen in een zandstorm. Het overbruggen van de kloof tussen de microscopische toestand van de deeltjes en de macroscopische continuüm beschrijving is een van de uitdagingen van de moderne wetenschap.

Poeders zijn een speciale gradatie van granulaire materialen dat zeer fijne deeltjes bevat dat vrij kan stromen wanneer deze wordt geschud of op een helling komt te liggen, maar kan echter blijven kleven onder rust of na samendrukken. Tijdens opslag of transport processen, ondergaat het materiaal verscheidende toestanden van deformatie en mechanisch spanning, bijvoorbeeld door compressie of afschuiving. In vele toepassingen is het belangrijk om te weten wanneer het poeder zwicht, oftewel wanneer het begint te stromen onder afschuiving. In andere gevallen is het van belang te weten hoeveel afschuifkracht het kost om het te laten blijven stromen. Het vloeigedrag veranderd dramatisch onder zeer laag tot zeer hoge mechanische spanning condities.

Het hoofddoel van deze thesis is het onderzoeken hoe de micro-mechanische eigenschappen het macroscopische bulk gedrag beïnvloed van granulaire materialen. Hiervoor wordt het opgesplitst in twee delen. Het eerste wordt toegewijd aan het doen van laboratoriumexperimenten en het tweede spits zich toe tot numerieke simulaties. In het eerste deel (i) wordt gefocust op het karakteriseren van granulaire materialen over verschillende lengte schalen voor zowel droge niet plakkerige, als plakkerige materialen, (ii) onderzoek naar het stroom gedrag in zowel lage als hoge mechanische spanningstoestanden met dezelfde materialen, (iii) het verkennen van verschillende test apparatuur om de meest geschikte technieken voor het meten van poeder stromingen te vinden. De focus van het tweede deel is (iv) het vormen van een model om granulaire stromen te beschrijven gebaseerd op de micro-mechanische inzichten van de discrete deeltjes simulaties.

In het eerste deel van deze studie wordt een breed en systematisch experimenteel onderzoek uitgevoerd om de invloeden van deeltjesgrootte en de plaksterkte tussen de deeltjes op het stroomgedrag van het poeder over verschillende mechanische spanningstoestanden af te schatten. Wij kiezen voor kalksteen poeder als referentiemateriaal vanwege de ongevoeligheid voor milieuveranderingen over de gehele studie. Als eerste, onderzochten we de invloed van de deeltjesgrootte op het zwichten van het kalksteen poeder in lage tot matige mechanische spanningstoestanden. Hierbij vonden we een interessant niet-monotone trend van bulk frictie en bulk plaksterkte vanwege de wisselwerking tussen de plaksterkte tussen de deeltjes en het geometrische in elkaar grijpen van de deeltjes. We leggen ook een empirisch model voor gebaseerd op de van der Waals interactie om het gedrag van de plaksterkte te beschrijven.

Als tweede gaan we naar de hogere mechanische spanningstoestanden door het samen-persen van onze poeders onder hoge druk. Hierbij onderzoeken we het effect van de deeltjesgrootte op de compactheid en de sterkte van het gevormde tablet. De geome-trische invloed die dominant was onder de lagere mechanische spanningstoestanden blijkt irrelevant onder hoge druk. Ten slotte hopen we de limieten van de verschillende dynamische en quasi-statische stromingstesten met elkaar te verbinden door de druk-krachten naar nul te laten gaan. Hierbij vonden we een overeenstemming tussen de twee verschillende experimenten. Deze nieuwe benadering geeft toegang tot een me-chanische spanningstoestand die niet bereikt kan worden met een conventioneel "shear cell" experiment.

In het tweede deel van de studie wordt, in plaats van een simulatie van elk experiment zoals uiteengezet in het eerste gedeelte, gezocht naar een goed gegeneraliseerd reolo-gisch model doormiddel van discrete elementen methode simulaties (DPM) voor het weergeven van verschillende granulaire stromingen onder variërende omstandigheden. Als eerste geven we een overzicht over de recente voortgang en nieuwe inzichten over het collectieve gedrag van granulaire, vervormbare deeltjes in zowel verdunde als vast-gelopen toestand. Vervolgens onderzoeken we systematisch de wisselwerking tussen de wrijving en de plakkracht tussen de deeltjes onder een constante stabiele afschuiving van homogene en niet homogene granulaire materialen en hiermee wordt ons reolo-gisch model uitgebreid naar een gegeneraliseerde omschrijving.

1

INTRODUCTION

1.1. GRANULAR MATERIALS

Since I was a child, there was always a question arising in my mind: what matters constitute the current world we are living in? After I have learned science, my answer is now particulate material. One could focus on a scale as small as the length of atoms but also zoom out as large as the gap between galaxies, and we always observe particles. In our common sense, matter is usually categorized into solids, liquids and gases, and thus people study them separately or collectively. However, a collection of distinct macroscopic particles, namely granular material, can behave sometimes like a solid, e.g. sand castle; sometimes like a liquid, e.g. snow avalanche or landslides; sometimes like a gas, e.g. sand storm; or all three states together, e.g. hourglass [1, 2] and granular jet [3]. The evolution of the particles follows Newton's equation of motion, with repulsive forces between particles that are non-zero only when there is a contact. Although the motion of granular materials is rather simple to describe, they exhibit a tremendous amount of complex behaviour, which has not yet been satisfactorily explained. The mixed behaviour encompassing solid, liquid and gas makes granular materials so challenging and thus has led many researchers characterize granular materials as a new form of matter.

One commonly seen granular material in daily life are food spices (Figure 1.1), they come to our home in many formats: separate distinctively as single particles or sticking together as powders, agglomerates, or tablets. In order to put them into our cooking dishes, we treat them using different means: pour out of a container, get out with some vibrations/shaking, or sometimes dig out with a spoon. If you forgot to close the container, some powders will absorb moisture from the air and then get stuck inside the container like a solid "rock", which can happen especially for fine powders like spices. From these experiences, we know how to insert energy into these materials to make them flow, although it does not always work. But what most people do not know is that these materials (food grains, seasonings, etc.) are normally produced in huge bulk in food industry and possibly stored in a big container – silo, before they are packaged and shipped to the supermarkets.

Figure 1.1: One of the most commonly seen granular material in our life: food spices. (Copyright Food and Beverage Buzz Magazine).

1.2. Getting to Know More About Powders

Powders are a special sub-class of granular materials, although the terms powder and granule are sometimes used to distinguish separate classes of material. Typically, powders refer to those granular materials that have the finer grain sizes, and that therefore have a greater tendency to form clumps. As powders normally come into our life with a wide range of particle sizes and form unstable clusters of variable sizes under different situations, it is very difficult to characterize the mechanical behaviour of powder flows. During storage and transportation in the processing industry, the powders undergo various modes of deformation and stress conditions, e.g. due to compression or shear. In many applications, it is important to know when powders are yielding, i.e., when they start to flow under shear. While in other cases, it is necessary to know how much stress the materials generate or can sustain when they are at static or at flowing state. Investigation of these cases leads to a better understanding of various types of powders and thus one can create a more reliable design of storage silos to avoid the failure/collapse (Figure 1.2). Another important situation that many facing in their daily life is to make the powders flow as you wish, e.g. take jammed/wet milk powder out of a container, mixing different species in a blender or grinding/dosing of coffee beans in a coffee machine. These situations are normally tackled using empirical correlations due to the complexity of powder composition at micro scale. Thus the solutions found are not universal. In order to understand and get deeper insight of the flow problems of powders, one has to know more about the mechanical properties through various characterization experiments, both in microscopic scale and bulk scale.

1.2.1. Characterization at Microscopic Scale

Powder usually comes with particle sizes from a few hundred nanometers to a few hundred microns, which creates a lot of difficulties to focus on details of single primary particles. With the development of modern techniques, the micro level details have become

accessible in the last few decades. Basic information on the nature and origin of granular material can often be gathered from the size, shape and/or surface topology that characterize individual particles. This type of information can be readily obtained by examining the particles in the scanning electron microscope (SEM). Powders usually come with a mixture of different size particles, this makes a single size measurement meaningless. To solve this issue, a particle size analyzer based on the laser diffraction or fast imaging of a collection of particles can be used [4, 5]. The true particle density is also another important property which can be used to evaluate the porosity of the primary particles. The true density is often examined by Helium pycnometry [6]. In order to understand the hardness and surface roughness of a single particle, and to correlate to tangential frictional behaviours, one could use atomic force microscopy or nano-indentation [7, 8].

Figure 1.2: Grain silo in process of collapsing (Copyright Jenike & Johanson, Inc.).

1.2.2. Characterization at Bulk Scale

Meanwhile, it is also useful to characterize the bulk mechanical responses of different powders. A typical lab scale test is called element test if it is an ideally homogeneous macroscopic test in which the force (stress) and/or displacement (strain) path can be controlled. One of the most widely performed element tests in both industry and academia is the shear test, where a granular sample is sheared at pre-defined confining stress until failure is reached and the material starts to flow. Shear testers are usually classified into two groups: direct and indirect methods [9, 10]. In direct shear testers, the shear zone is pre-defined by the device design, and the shear failure is forced in a specific physical location. On the contrary, in the indirect devices, the shear zone develops according to the applied state of stress. The most common indirect devices are the uni-axial compression tester (Oedometer or Lambda-meter) [11–16] and bi-axial shear box [17–19]. Direct devices can be further categorised into two sub-groups: translational and rotational. Typical translational shear testers include the direct shear tester [20–22] and the Jenike shear tester [23], while torsional or rotational shear testers include the FT4 powder rheometer [24], the Schulze ring shear tester [25] and the Brookfield powder flow

1

tester [26]. By gathering different reliable material mechanical responses under different stress conditions, one could estimate how the powder will flow or not inside a silo and therefore draw a reliable design.

1.2.3. THE MISSING CONNECTION

On one hand, microscopic scale characterization tests offer us many details on both single primary particles as well as the statistics of a collection of particles. On the other hand, the bulk scale element tests neglect the details and offer us a global response and thus contribute more directly to the process design. There is a clear gap between these two types of tests, which is the link from micro/particle level information to the bulk flow behaviour. This link is the key element of modeling the powder or granular flows and therefore predict or even fully control the flow behaviour. However, this link is very difficult or even sometimes impossible to find due to the complexity of details in the microscopic scale, the combined influences from microscopic origins and different boundary conditions. Nevertheless, the first major goal of this thesis is to address this complicated question and shed a light on how to reconnect this micro-macro link by reducing the complexity from materials.

1.3. MODELING GRANULAR FLOW

The final goal of studying granular material is to fully understand the physical behaviours and then propose models that can predict the granular flow successfully. In general, there are two ways of modeling granular materials: the continuum approach and the microscopic approach. The former approach is developed based on the classical solid/fluid mechanics, while the latter one has only become available in the last few decades due to the fast development of computers as well as new experimental techniques.

1.3.1. THE CONTINUUM VERSUS MICRO-MECHANICAL APPROACH

The continuum approach normally refers to those models that are derived from the behaviour of continuum media, i.e., gas/liquid/solid, which offers a general description but neglecting small details, e.g. the discrete nature within the material themselves. Many people try to draw analogies between granular materials and gas/liquid/solid. For example, water, depending on the prevailing temperature and pressure, water may take on different states of matter. Water usually comes into our sight as liquid at room temperature and pressure. However, if we increase or decrease the temperature, water can change state and become vapor (gas) or ice (solid) with different properties than when it is in the liquid state. Due to this multi-variate nature, it is impossible to fully classify water as a perfect solid, liquid or gas. Yet water is so complicated to describe, the behaviour of granular material is even more complicated, due to the dissipative nature of collisions between the grains. Collisions are inelastic and thus lead to energy loss. Hence the granular materials are not in thermal equilibrium and the classical laws governing the flow of fluids and gases do not predict well granular flows in general.

For example, to model a granular flow in the gaseous regime, one can apply the traditional standard kinetic theory (SKT) to the granular gas [27, 28]. SKT was rigorously de-

rived under very restrictive assumptions. In particular, the granular system is assumed to be mono-disperse and composed of spherical, frictionless and rigid particles, interacting only through binary and uncorrelated collisions [29–31]. SKT was extended to include dissipation, friction, polydispersity, etc. and can then be used up to moderately dense fluids of volume fractions around 0.5. On the other hand, when a granular flow is getting very dense, the flow behaves closer to the plastic deformation of a solid. Therefore, elasticity/plasticity theories from solid mechanics are often used to model dense granular packing [32, 33]. Although many have attempted to find continuum models that cover both dilute and dense regimes, they are still not yet widely accepted due to the lack of simplicity and too many restrictive assumptions needed.

Unlike the continuum approach, micro-mechanical studies of granular materials can give a much deeper understanding of their macro-scale behavior, as dense granular materials are usually characterized by enduring contacts between particles and the existence of force chains [34–38]. The main drawback of this approach is time or/and computational power cost, which limits its applicability to only small scale systems. Many studies [34, 39–44] classify the contacts into subnetworks of strong and weak contacts, where it is shown that the anisotropic shear stress of granular materials is primarily carried by the strong contacts. From the perspective of granular flow, researchers have investigated different flow configurations like plane shear, Couette shear cell, silos, flow down inclined planes, or avalanches on piles and in rotating drums [45–49]. Shear bands, localized regions of concentrated shear, are an important feature of complex fluids like granular materials, when deformed irreversibly [50, 51]. However, the need for bulk predictions has restricted the studies of granular materials mainly to real systems which are far too complex for a microscopic approach. One rather uses continuum models, with empirical material laws as input which exhibit effects similar to those observed in the real systems of materials.

1.3.2. CLASSICAL $\mu - I$ RHEOLOGY

The $\mu - I$ rheology is one widely used phenomenological models in the last two decades, as proposed by GDR-Midi in 2004 [47, 48]. It can be expressed as relations between three non-dimensional quantities: volume fraction, shear to normal stress ratio, usually called $\mu = \tau/p$, and inertial number $I = \dot{\gamma} d \sqrt{\rho_p/p}$, defined as the ratio of the time scales associated with the motion perpendicular and parallel to the flow [49, 52]. The inertial number provides an estimate of the local rapidity of the flow, with respect to pressure, and is of significance in dynamic/inertial flows, as shown in [53]. In dense, quasi-static flows, particles interact by enduring contacts and inertial effects are negligible, as I goes to zero.

1.3.3. TOWARDS A MORE GENERALIZED $\mu - I$ RHEOLOGY

The classical $\mu - I$ rheology is only valid for dense granular flows of rigid particles over a limited range of the inertial regime. Thus various constitutive relations, based on this GDR-MiDi $\mu - I$ rheology, have been developed [48, 54–56] in order to extend the validity of the model. In particular, the influence of particle deformability has been accounted for in the soft $\mu(I)$-rheology proposed in [57–59]. This model tries to simplify the com-

plex behaviour by quantifying additional mechanisms by different dimensionless numbers, which are intrinsically the competition among different time scales.

Although these studies proposed many nice models that might work in many different situations, so far they were derived and tested but only for specific granular materials. It is still not yet clear how micro-mechanical properties influence granular bulk flow, and thus the model. Therefore, the second goal of this study is to address this complicated problem by focusing on how the microscopic particle properties influence the bulk flow behaviour using DEM simulations as a tool to further extend the classical $\mu - I$ rheology towards a more general description and to provide data for calibration and validation.

1.4. DISCRETE ELEMENT METHOD - A NUMERICAL TOOL

The Discrete Element Method (DEM) is a particle-scale numerical method for modeling the bulk behavior of granular materials and tracking the details at microscopic level. Based on the Newton's law of motion, it can capture the movement of each single particle in the system as well as their collision details at each contact. The main ingredient of this method is the force contact model, which defines how particles deform and interact with each other when they are at contact, e.g. the force-displacement behaviour of a single particle. Although it is computationally very costly, the method offers a much deeper insight at the microscopic level of a granular system and thus allows to investigate micro-mechanical influences separately. The popularity of this method increased dramatically in the last decades due to the development of computer hardware. People apply it widely to many granular materials such as coal, ore, soils, rocks, aggregates, pellets, tablets and powders, based on different kinds of contact/interaction models. The first application of DEM date back to the seventies of the last century and are associated with rock mechanics (In 1971, Peter Cundall completed his doctorate at Imperial College London: The Distinct Element Method for modeling jointed rock and granular material) that published in 1979 [60]. The work then has been extended and more generalized towards different granular assemblies.

1.4.1. FROM SHEAR BANDS TOWARDS CONTINUUM THEORY

Continuum constitutive relations for bulk granular flow, form the basis for a hydrodynamic theory are mostly derived and verified from small scale representative micro-scale simulations, e.g. DEM simulations [60–64]. Many studies have focused on the shear band formation for plastic granular flows in rectangular, vertical-pipe chute configurations. In these geometries, granular flows exhibit plug flow in the central region with shear bands near the side walls. Until 2001, it was mostly reported that granular shear bands are narrow, i.e., a few particle diameters wide. In a modified Couette cell, or socalled split-bottom shear cell, granular flow is driven from the bottom, instead from the side walls [65–69]. Typically, a disc of radius R_s, mounted at the bottom is rotated at a rate Ω while the outer container is fixed. The differential motion of the disc and the container creates a very thin shear band at bottom that becomes wide further upwards and remains away from the walls. The tails of the velocity profile decay as an error function, not an exponential function like in the Couette cell. These observations indicate that there is a continuum theory with its own domain of validity, that should capture this

1

smooth quasi-static granular flow regime even though one can not expect a "universal" continuum theory for all granular flow situations [70]. All the geometries with real walls have same influence from the boundaries and this will have to be included inside the theory. In order to remove the effect of boundaries, there is another commonly used geometry in numerical study, which is a cuboid box with periodic boundary and/or Lees-Edwards boundary [71–73]. Using this technique, one can focus on the flow behaviour of pure granular materials without any effects from the real walls/boundaries.

1.5. THESIS OUTLINE

The aim of this thesis is to study the deformation behaviour of a wide range of granular materials from free flowing to cohesive under different stress, strain and dynamic conditions, to bridge the gap between the micro-mechanical parameters and macroscopic bulk mechanical responses. Both laboratory tests and discrete element simulations are used as tools to understand the micro-macro responses. The thesis can be split into two distinct, yet interrelated parts:

1. The first part is accomplished *purely* using laboratory experiments. Both flow and compaction behaviours of limestone powders of different sizes are investigated in a wide range of confining stresses and presented in Chapter 2 to 4.

2. The second part (Chapter 5 and 6) focuses on the constitutive modeling of sheared granular flow, and on how to develop a generalized granular rheology. This part of study is conducted using discrete element simulations (DEM).

Both parts focus on investigating the correlations between microscopic and macroscopic granular deformation/flow behaviour. The micro-macro mechanical links we found in the experimental part are always a mix of various micro-mechanical factors and it is almost impossible to separate one from another. In simulations, one could use idealized spherical particle as well as simplified contact laws, to study one micro-mechanical factor per time and fully isolate from other parameters. Therefore, instead of reproducing exactly the bulk stress-strain response from a single experimental/element test, we focus more on the qualitative bulk behaviour influenced by both single/multiple micro-mechanical parameters.

In Chapter 2, we have systematically examined the powder flow behaviour of limestone powder samples with varying median particle sizes in different shear testers at different confining stress levels. All shear testers investigated show highly reproducible results and good overall, consistent agreement among each other, while automated devices minimize the operator influence. We observe that differences in the protocol can result in considerable differences in the measured material response even if the qualitative trends are found to be consistent among different shear testers. When the median particle size increases over three orders of magnitude, the macroscopic powder flow resistance shows a non-monotonic trend: first decreases then increases with a bottom plateau. From this observation, we further identify two regimes that are dominated by different mechanisms: contact cohesion between fine particles and geometrical sliding/rolling effects between coarse particles.

1

The confining pressure in Chapter 2 ranges from 5 to 35 kPa, which is typical for powder process engineering. One could ask how would these powders behave when pressure increases. Thus, Chapter 3 complements the study in Chapter 2 with the analysis of powder behaviour in the high compaction pressure regime. Here, we mainly focus on exploring the pressure and particle size influences on two different aspects: i) the density-stress-strain behaviour during a uniaxial compaction process; ii) the tablet quality parameters after the compaction process, e.g. the elastic recovery ratio and the tablet tensile strength.

In the other limit, we look at the material behaviour at very low confining pressure. This problem is approached by extending the limits of several types of test to lower stresses. In Chapter 4, we study differences between the static, quasi-static and the dynamic flow tests, namely GranuHeap (angle of repose), Schulze ring shear tester and GranuDrum (flowing angle). Goal is to stretch the quasi-static test towards lower stress, while the dynamic test is extended towards lower rotation speed, using both free-flowing and cohesive limestone powders. A good agreement of frictional angles among these tests are found for both free flowing and cohesive powders. This chapter closes the first part of the thesis.

For the second part of this work, in Chapter 5, we first give an overview of recent progress in understanding and theoretically describing the collective mechanical behavior of dissipative, deformable particles in different states, both fluid-like and solid-like. We also provide here a few methods and some phenomenology, as well as theories that can describe the systems residing in different states, and focus on their dependencies on the material properties, for example, the contact duration/deformation (stiffness), the dissipation (restitution coefficient) and the size distribution (polydispersity) of the particles.

Chapter 6 is a continuation of Chapter 5, in which we extend an existing rheological model [59] to predict the steady state volume fraction of granular flow including the influences of inter-particle friction and cohesion and find an interesting interplay between the two micro-mechanical parameters. This offers a deeper insight into the link between microscopic mechanical properties and macroscopic flow behaviour. We calibrated this extended steady state rheological model using two different simulation geometries: homogeneous stress controlled simple shear box and inhomogeneous split bottom shear cell.

Finally, we give our conclusion and an outlook in Chapter 7.

REFERENCES

[1] H. M. Jaeger, S. R. Nagel, and R. P. Behringer, *Granular solids, liquids, and gases,* Rev. Mod. Phys. **68**, 1259 (1996).

[2] H. M. Jaeger, S. R. Nagel, and R. P. Behringer, *The physics of granular materials,* Physics Today **49**, 32 (1996).

[3] D. Lohse, R. Bergmann, R. Mikkelsen, C. Zeilstra, D. van der Meer, M. Versluis, K. van der Weele, M. van der Hoef, and H. Kuipers, *Impact on soft sand: void collapse and jet formation,* Physical review letters **93**, 198003 (2004).

[4] M. Konert and J. Vandenberghe, *Comparison of laser grain size analysis with pipette and sieve analysis: a solution for the underestimation of the clay fraction,* Sedimentology **44**, 523 (1997).

[5] B. Y. Shekunov, P. Chattopadhyay, H. H. Tong, and A. H. Chow, *Particle size analysis in pharmaceutics: principles, methods and applications,* Pharmaceutical research **24**, 203 (2007).

[6] A. Ayral, J. Phalippou, and T. Woignier, *Skeletal density of silica aerogels determined by helium pycnometry,* Journal of materials science **27**, 1166 (1992).

[7] B. Briscoe, L. Fiori, and E. Pelillo, *Nano-indentation of polymeric surfaces,* Journal of Physics D: Applied Physics **31**, 2395 (1998).

[8] M. Paulick, M. Morgeneyer, and A. Kwade, *A new method for the determination of particle contact stiffness,* Granul. Matter. **17**, 83 (2015).

[9] J. Schwedes, *Review on testers for measuring flow properties of bulk solids,* Granul. Matter **5**, 1 (2003).

[10] J. Schwedes and D. Schulze, *Measurement of flow properties of bulk solids,* Powder Technol. **61**, 59+ (1990).

[11] A. Kwade, D. Schulze, and J. Schwedes, *Determination of the stress ratio in uniaxial compression tests - Part 1,* Powder handling & Processing **6**, 61 (1994).

[12] A. Kwade, D. Schulze, and J. Schwedes, *Determination of the stress ratio in uniaxial compression tests - Part 2,* Powder handling Processing **6**, 199 (1994).

[13] A. Kwade, D. Schulze, and J. Schwedes, *Design of silos: Direct measurement of stress ratio [Auslegung von Silos. Unmittelbare Messung des Horizontallastverhaeltnisses],* Beton- und Stahlbetonbau **89**, 58 (1994).

[14] A. Russell, P. Müller, H. Shi, and J. Tomas, *Influences of loading rate and preloading on the mechanical properties of dry elasto-plastic granules under compression,* AIChE J. **60**, 4037 (2014).

[15] S. C. Thakur, H. Ahmadian, J. Sun, and J. Y. Ooi, *An experimental and numerical study of packing, compression, and caking behaviour of detergent powders,* Particuology **12**, 2 (2014).

[16] O. I. Imole, M. Paulick, V. Magnanimo, M. Morgeneyer, B. E. Montes, M. Ramaioli, A. Kwade, and S. Luding, *Slow stress relaxation behavior of cohesive powders,* Powder technol. **293**, 82 (2016).

[17] M. Morgeneyer, L. Brendel, Z. Farkas, D. Kadau, D. E. Wolf, and J. Schwedes, *Can one make a powder forget its history?* Proc. of the 4th international conference for conveying and handling of particulate solids, Budapest , 12 (2003).

[18] M. Morgeneyer and J. Schwedes, *Investigation of powder properties using alternating strain paths,* Task Quarterly **7**, 571 (2003).

1

[19] H. Feise and J. Schwedes, *Investigation of the Behaviour of Cohesive Powder in the Biaxial Tester,* Kona Powder Part. J. **13**, 99 (1995).

[20] A. Casagrande, *The determination of the pre-consolidation load and its practical significance,* in *Proceedings of the international conference on soil mechanics and foundation engineering*, Vol. 3 (Harvard University Cambridge, 1936) pp. 60–64.

[21] J. Schwedes, *Vergleichende betrachtungen zum einsatz von schergeräten zur messung von schüttguteigenschaften,* Proc. PARTEC, Nürnberg , 278 (1979).

[22] S. Shibuya, T. Mitachi, and S. Tamate, *Interpretation of direct shear box testing of sands as quasi-simple shear,* Geotechnique **47**, 769 (1997).

[23] A. W. Jenike, *Storage and Flow of Solids, Bulletin No. 123,* Bulletin of the University of Utah **53**, 198 (1964).

[24] R. Freeman, *Measuring the flow properties of consolidated, conditioned and aerated powders - A comparative study using a powder rheometer and a rotational shear cell,* Powder Technol. **174**, 25 (2007).

[25] D. Schulze, *Entwicklung und Anwendung eines neuartigen Ringschergerätes,* Aufbereitungs-Technik **35**, 524 (1994).

[26] R. J. Berry, M. S. A. Bradley, and R. G. McGregor, *Brookfield powder flow tester-Results of round robin tests with CRM-116 limestone powder,* Proceedings of the Institution of Mechanical Engineers, Part E: Journal of Process Mechanical Engineering **229**, 215 (2015).

[27] J. T. Jenkins and S. B. Savage, *A theory for the rapid flow of indentical, smooth, nearly elastic, spherical particles,* J. Fluid Mech. **130**, 187 (1983).

[28] C. Lun, S. B. Savage, D. Jeffrey, and N. Chepurniy, *Kinetic theories for granular flow: inelastic particles in couette flow and slightly inelastic particles in a general flowfield,* Journal of fluid mechanics **140**, 223 (1984).

[29] J. T. Jenkins and C. Zhang, *Kinetic Theory for Identical, Frictional, Nearly Elastic Spheres,* Physics of Fluids **14**, 1228 (2002).

[30] M. Alam, J. T. Willits, B. O. Arnarson, and S. Luding, *Kinetic theory of a binary mixture of nearly elastic disks with size and mass disparity,* Physics of Fluids **14**, 4087 (2002).

[31] D. Berzi and D. Vescovi, *Different singularities in the functions of extended kinetic theory at the origin of the yield stress in granular flows,* Physics of fluids **27**, 013302 (2015).

[32] P. V. Lade and R. B. Nelson, *Modelling the elastic behaviour of granular materials,* International journal for numerical and analytical methods in geomechanics **11**, 521 (1987).

1

[33] G. Gudehus, *A comprehensive constitutive equation for granular materials,* Soils and Foundations **36**, 1 (1996).

[34] T. S. Majmudar and R. P. Behringer, *Contact force measurements and stress-induced anisotropy in granular materials,* Nature **435**, 1079 (2005).

[35] B. Miller, C. O'Hern, and R. P. Behringer, *Stress Fluctuations for Continously Sheared Granular Materials,* Phys. Rev. Lett. **77**, 3110 (1996).

[36] D. Howell, R. P. Behringer, and C. Veje, *Stress fluctuations in a 2D granular Couette experiment: A continuous transition,* Phys. Rev. Lett. **82**, 5241 (1999).

[37] A. Ferguson, B. Fisher, and B. Chakraborty, *Impulse distributions in dense granular flows: Signatures of large-scale spatial structures,* EPL (Europhysics Letters) **66**, 277 (2004).

[38] A. Ferguson and B. Chakraborty, *Stress and large-scale spatial structures in dense, driven granular flows,* Physical Review E **73**, 011303 (2006).

[39] F. Radjai, D. E. Wolf, M. Jean, and J. Moreau, *Bimodal Character of Stress Transmission in Granular Packings,* Phys. Rev. Lett. **80**, 61+ (1998).

[40] S. Luding, R. Tykhoniuk, and J. Tomas, *Anisotropic material behavior in dense, cohesive-frictional powders,* Chemical Engineering and Technology **26**, 1232 (2003).

[41] S. Luding, *Micro-macro transition for anisotropic, frictional granular packings,* International Journal of Solids and Structures **41**, 5821 (2004).

[42] C. O'Sullivan and L. Cui, *Micromechanics of granular material response during load reversals: Combined DEM and experimental study,* Powder Technol. **193** (2007), 10.1016/j.powtec.2009.03.003.

[43] E. Azéma and F. Radjai, *Force chains and contact network topology in sheared packings of elongated particles.* Phys. Rev. E **85**, 31303 (2012).

[44] O. I. Imole, M. Wojtkowski, V. Magnanimo, and S. Luding, *Force correlations, anisotropy, and friction mobilization in granular assemblies under uniaxial deformation,* Powders and Grains, AIP Conf. Proc. **601**, 601 (2013).

[45] Y. Forterre and O. Pouliquen, *Flows of Dense Granular Media,* Annu. Rev. Fluid Mech. **40**, 1 (2008).

[46] P. Schall and M. van Hecke, *Shear bands in matter with granularity,* Annu. Rev. Fluid Mech. **42** (2010).

[47] G. D. R. MiDi, *On dense granular flows,* Eur. Phys. J. E **14**, 341 (2004).

[48] P. Jop, Y. Forterre, and O. Pouliquen, *A constitutive law for dense granular flows,* Nature **441**, 727 (2006).

1

[49] O. Pouliquen, C. Cassar, P. Jop, Y. Forterre, and M. Nicolas, *Flow of dense granular material: towards simple constitutive laws,* J. of Stat. Mech.: Theory and Experiment **2006**, P07020 (2006).

[50] P. A. Cundall, *Numerical experiments on localization in frictional materials,* Ingenieur-Archiv **59**, 148 (1989).

[51] H. B. Mühlhaus and I. Vardoulakis, *The thickness of shear bands in granular materials,* Géotechnique **37**, 271 (1987).

[52] J. Gray and A. Edwards, *A depth-averaged μ(I)-rheology for shallow granular free-surface flows,* Journal of Fluid Mechanics **755**, 503 (2014).

[53] N. Berger, E. Azéma, J. F. Douce, and F. Radjai, *Scaling behaviour of cohesive granular flows,* EPL (Europhysics Letters) **112**, 64004 (2016).

[54] F. Da Cruz, S. Emam, M. Prochnow, J.-N. Roux, and F. Chevoir, *Rheophysics of dense granular materials: Discrete simulation of plane shear flows,* Physical Review E **72**, 021309 (2005).

[55] R. C. Daniel, A. P. Poloski, and A. Eduardo Sáez, *A continuum constitutive model for cohesionless granular flows,* Chem. Eng. Sci. **62**, 1343 (2007).

[56] P. Jop, *Hydrodynamic modeling of granular flows in a modified Couette cell,* Phys. Rev. E **77**, 32301 (2008).

[57] A. Singh, V. Magnanimo, K. Saitoh, and S. Luding, *The role of gravity or pressure and contact stiffness in granular rheology,* New J. Phys. **17**, 043028 (2015).

[58] S. Roy, A. Singh, S. Luding, and T. Weinhart, *Micro-macro transition and simplified contact models for wet granular materials,* Computational particle mechanics **3**, 449 (2016).

[59] S. Roy, S. Luding, and T. Weinhart, *A general(ized) local rheology for wet granular materials,* New Journal of Physics **19**, 043014 (2017).

[60] P. A. Cundall and O. D. L. Strack, *A discrete numerical model for granular assemblies,* Géotechnique **29**, 47 (1979).

[61] F. Alonso-Marroquin, S. Luding, H. J. Herrmann, and I. Vardoulakis, *Role of anisotropy in the elastoplastic response of a polygonal packing,* Phys. Rev. E **71** (2005).

[62] S. Luding, *Anisotropy in cohesive, frictional granular media,* J. Phys. Condens. Matter **17** (2005).

[63] S. Luding, *Cohesive, frictional powders: contact models for tension,* Granul. Matter **10**, 235 (2008).

[64] J. Sun and S. Sundaresan, *A plasticity model with microstructure evolution for quasi-static granular flows,* in *AIP Conference Proceedings*, Vol. 1227 (AIP, 2010) pp. 280–289.

[65] D. Fenistein and M. van Hecke, *Kinematics – Wide shear zones in granular bulk flow,* Nature **425**, 256 (2003).

[66] D. Fenistein, J. W. van de Meent, and M. van Hecke, *Universal and wide shear zones in granular bulk flow,* Phys. Rev. Lett. **92**, 94301 (2004).

[67] X. Cheng, J. B. Lechman, A. Fernandez-Barbero, G. S. Grest, H. M. Jaeger, G. S. Karczmar, M. E. Möbius, and S. R. Nagel, *Three-dimensional shear in granular flow,* Phys. Rev. Lett. **96**, 038001 (2006).

[68] J. A. Dijksman and M. van Hecke, *Granular flows in split-bottom geometries,* Soft Matter **6**, 2901 (2010).

[69] D. L. Henann and K. Kamrin, *A predictive, size-dependent continuum model for dense granular flows,* Proceedings of the National Academy of Sciences **110**, 6730 (2013).

[70] M. Depken, W. van Saarloos, and M. van Hecke, *Continuum approach to wide shear zones in quasistatic granular matter,* Physical Review E **73**, 031302 (2006).

[71] A. W. Lees and S. F. Edwards, *The computer study of transport processes under extreme conditions,* J. Phys. C: Solid State Phys. **5**, 1921 (1972).

[72] D. Vescovi and S. Luding, *Merging fluid and solid granular behavior,* Soft matter **12**, 8616 (2016).

[73] H. Shi, D. Vescovi, A. Singh, S. Roy, V. Magnanimo, and S. Luding, *Granular flow: From dilute to jammed states,* in *Granular Materials,* edited by M. Sakellariou (In-Tech, 2017).

2

EFFECT OF PARTICLE SIZE AND COHESION ON POWDER YIELDING AND FLOW

The bulk properties of powders depend on material characteristics and size of the primary particles. During storage and transportation processes in the powder processing industry, the material undergoes various modes of deformation and stress conditions, e.g. due to compression or shear. In many applications, it is important to know when powders are yielding, i.e., when they start to flow under shear; in other cases it is necessary to know how much stress is needed to keep them flowing. The measurement of powder yield and flow properties is still a challenge and will be addressed in this study.

In the framework of the collaborative project T-MAPPP, a large set of shear experiments using different shear devices, namely the Jenike shear tester, the ELE direct shear tester, the Schulze ring shear tester and the FT4 powder rheometer, have been carried out on eight chemically-identical limestone powders of different particle sizes in a wide range of confining stresses. These experiments serve two goals: i) to test the reproducibility/consistency among different shear devices and testing protocols; ii) to relate the bulk behaviour to microscopic particle properties, focusing on the effect of particle size and thus inter-particle cohesion.

The experiments show high repeatability for all shear devices, though some of them show more fluctuations than others. All devices provide consistent results, where the FT4 powder rheometer gives lower yield/steady state stress values, due to a different pre-shearing protocol. As expected, the bulk cohesion decreases with increasing particle size (up to 150 µm), due to the decrease of inter-particle cohesion. The bulk friction, characterized in different ways, is following a similar decreasing trend, whereas the bulk density increases with particle size in this range. Interestingly, for samples with particle sizes larger than 150 µm, the bulk cohesion increases slightly, while the bulk friction increases considerably

– presumably due to particle interlocking effects – up to magnitudes comparable to those of the finest powders. Furthermore, removing the fines from the coarse powder samples reduces the bulk cohesion and bulk density, but has a negligible effect on the bulk friction. In addition to providing useful insights into the role of microscopically attractive, van der Waals, gravitational and/or compressive forces for the macroscopic bulk powder flow behaviour, the experimental data provide a robust database of cohesive and frictional fine powders for industrially relevant designs such as silos, as well as for calibration and validation of models and computer simulations.

2.1. Introduction

Granular materials are omnipresent in our daily life and widely used in various industries such as food, pharmaceutical, agriculture and mining. Interesting granular phenomena like yielding and jamming [2–5], dilatancy [6–8], shear-band localization [9, 10], history-dependence [11], and anisotropy [12, 13] have attracted significant scientific interest over the past decades [14–23]. Various laboratory element tests can be performed to study the bulk behaviour of granular materials [24]. Element tests are also a valuable tool to understand the influence of particle properties, e.g. density, size-distribution and shape, on the macroscopic bulk response. Moreover, such element tests are commonly used for the industrial designs of silos [25–27].

Element tests are (ideally homogeneous) macroscopic tests in which the force (stress) and/or displacement (strain) path are controlled. The most widely performed element test in both industry and academia is the shear test, where a granular sample is sheared until failure is reached and the material starts to flow. Shear testers are usually classified into two groups: direct and indirect methods [24, 26]. In direct shear testers, the shear zone is pre-defined by the device design, and the shear failure is forced in a specific physical location. On the contrary, in the indirect devices, the shear zone develops according to the applied state of stress. The most common indirect devices are the uniaxial compression tester [11, 28, 29] and bi-axial shear box [30–32]. Direct devices can be further categorised into two sub-groups: translational and rotational. Typical translational shear testers include the direct shear tester [33–35] and the Jenike shear tester [36], while torsional or rotational shear testers include the FT4 powder rheometer [37], the Schulze ring shear tester [38] and the Brookfield powder flow tester [39]. Detailed reviews of testers have been presented by several authors [24, 40, 41], and more (non-commercial) shear testers with higher complexity can be found in literature [42–44].

Quality and reproducibility of results are key aspects for proper material characterization. Although shear testing technologies have been developed and studied extensively, significant scatter in measurements is still common when testing powder flowability using different devices in different labs/environments [37–39, 45–47]. Previous studies have been focusing on this problem by performing round-robin experimental studies on the Jenike tester [48], the Schulze ring shear tester [45] and the Brookfield powder flow tester [39] as well as comparing different devices [49]. The earliest round-robin study [48] resulted in a certified material (CRM-116 limestone powder) and a common standard experimental testing procedure for determining the yield locus. Schulze [45] has collected 60 yield loci obtained using the small Schulze shear tester RST-XS (21 labs)

and 19 yield loci using the large Schulze shear tester RST-01 (10 labs) on one limestone powder (CRM-116). Results have been compared among them as well as with the results from reference Jenike tester. While results from RST-01 and RST-XS are in good agreement, a considerable deviation (up to 20 %) was observed when comparing results from the Schulze ring shear tester to the Jenike shear tester. Similar outputs are found by other researchers [39, 49, 50], where yield loci from the Brookfield powder flow tester, the Schulze ring shear tester, the FT4 powder rheometer and the Jenike shear tester are compared. The Brookfield powder flow tester and the FT4 powder rheometer show systematically lower shear responses in comparison to the other two shear testers.

Other studies have compared different industrially relevant powders but only in a single device [51, 52]. Moreover, these comparative studies have been limited to relatively low stresses. A deeper understanding of the flow behaviour of powders in several shear devices over a wide stress range is still missing.

Our collaborative network, EU/ITN T-MAPPP (www.t-mappp.eu), offers the unique possibility to shed light on the complex topic of powder yielding and flow, extending beyond the boundaries of previous projects. The network involves 16 partners in both academia and industry across Europe. The present study has multiple goals. Firstly, we want to investigate the consistency and repeatability of yield loci measurements between commonly used shear testers. This can provide a robust platform to establish the reliability of the testing methodology and procedures. Secondly, we aim to study the influence of cohesion on powder flowability by testing powders that have same chemical composition but different particle size, leading to different degrees of bulk cohesion. Finally, once the agreement between the shear devices is established, measurements can be combined to characterise the powders over a wider stress range, which is not achievable with a single device. To achieve this goal, a systematic study has been carried out by testing 8 powders (Eskal limestone with median particle diameter from 2.2 to 938 μm) in 5 shear testers (the Jenike Shear Tester, the Direct Shear Tester, the Schulze Ring Shear Tester with two shear cell sizes, and the FT4 Powder Rheometer) at 4 partner locations by different operators. Limestone powder has been chosen due to its negligible sensitivity towards humidity and temperature changes.

The work is structured as follows: In section 2.2, we provide information on the limestone samples/materials, in section 2.3 the description of the experimental devices and in section 2.4 the test procedures. Sections 2.5 and 2.6 are devoted to the discussion of experimental results with focus on shear devices and materials, respectively, while conclusions and outlook are presented in section 2.7.

2.2. MATERIAL DESCRIPTION AND CHARACTERIZATION

In this section, a brief description of the limestone samples along with their material properties is provided. Eight size grades with the same chemical composition, i.e., Eskal limestone (calcium carbonate), are used, with median particle sizes that almost span three orders of magnitude from μm to mm.

The Eskal series (KSL Staubtechnik GmbH, Germany) is extensively used in many fields including construction and automotive industries. Eskal is also used as a reference pow-

Table 2.1: Material parameters of the experimental samples. The initial bulk density represents bulk density from raw materials. Here, K0.1-0.5 means Körnung 0.1-0.5, which follows the commercial product naming. The initial bulk density values are provided by the manufacturer.

Property (Eskal)		Unit	300	500	15	30	80	150	K0.1-0.5	K0.5-0.8
	d_{10}	μm	0.78	1.64	12	21	39	97	4.5	738
Particle Size	d_{50}	μm	**2.22**	**4.42**	**19**	**30**	**71**	**138**	**223**	**938**
	d_{90}	μm	4.15	8.25	28	43	106	194	292	1148
Span	$(d_{90}\text{-}d_{10})/d_{50}$	[-]	1.52	1.50	0.84	0.73	0.94	0.70	1.29	0.44
Particle density	ρ_p	kg/m^3	2737	2737	2737	2737	2737	2737	2737	2737
Moisture content	w	%	0.9	0.9	0.9	0.9	0.9	0.9	0.9	0.9
Roundness	Ψ	[–]	0.75	0.55	0.48	0.66	0.84	0.88	0.74	0.85
Initial bulk density	ρ_0	kg/m^3	540	730	1110	1230	1330	1370	1400	1276

der for standard testing and calibration of equipment in powder technology, for instance, shear testers [53, 54] and optical sizing systems due to the favourable physical properties: high roundness, low porosity and an almost negligible sensitivity towards humidity and temperature changes, which allows to avoid sample pretreatment.

Table 2.1 summarizes the physical properties of the Eskal samples. Median particle size d_{50} ranges from 2.22 μm (cohesive, sticky primary particles that form clumps) to 938 μm (free-flowing primary particles). In this study, all powders are named with their original commercial name (e.g. Eskal150, Eskal300), except for Eskal K0.1-0.5 and K0.5-0.8 (original product names are Eskal Körnung 0.1-0.5 and Körnung 0.5-0.8), which for sake of brevity, is referred to as "K". The particle size distributions were determined by laser diffraction (HELOS+RODOS, Sympatec GmbH) with the dry dispersion unit. The span of the particle size distribution decreases with increasing particle size from 1.52 to 0.7, whereas the initial bulk density (bulk density measured directly after filling) increases from 540 to 1400 kg/m^3. Primary particle density ρ_p is measured using a helium pycnometer at 0.9% moisture content and is found to be independent of size. Particle roundness, which is the ratio of the perimeter of the equivalent circle to the real perimeter of the projected primary particle, was measured with the Sympatec-QICPIC imaging system. The working principle of this technique consists of a high-speed image analysis sensor capable of capturing 500 frames per second with low exposure time below 1 ns; this set-up allows to capture and measure with a high detail size and shape information of an extremely large number of particles in the size range of 1 μm to 30 mm [55]. Values are the average over approximately the range between 20000 and 8000000 particles, depending on the median size of primary particles in the powders. The median particle size, d_{50}, is used in the following as reference to the different Eskal samples.

Figures 2.1 and 2.2 show the scanning electron microscopy images of EskalK0.1-0.5 and Eskal30, in two different length scales. The topography of the surfaces are created using secondary electron imaging (SEI) method. In Fig. 2.1, we see that all the Eskal30 primary particles have similar shapes (left) and rough surfaces (right). But for Eskal K0.1-0.5, in Fig. 2.2, we observe more fines between the coarse particles (left) as well as on the surface (right). The other Eskal samples have mostly similar shapes (difference in the range of 20%, considering the mean values of roundness) irrespective of median particle size of the samples.
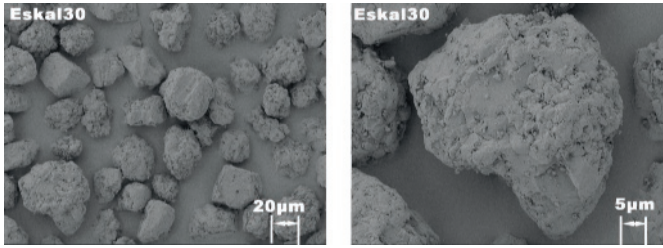
Figure 2.1: SEM topography images of Eskal30 ($d_{50} = 30\ \mu$m) in two different length scales as shown in the scale bars.
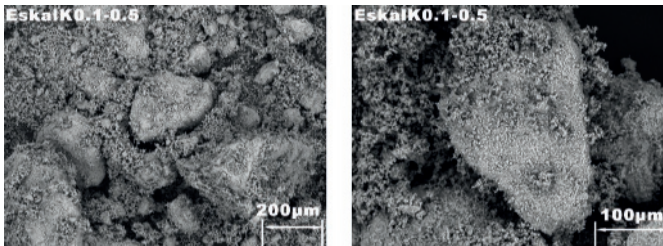
Figure 2.2: SEM topography images of EskalK0.1-0.5 ($d_{50} = 223\ \mu$m) in two different length scales as shown in the scale bars.

2.3. EXPERIMENTAL SET-UP

Many testers have been invented for measuring the yielding and flow properties of bulk solids in the last 70 years, ranging from the Jenike Shear Tester to the semi-automated or fully automated testers that are being developed in the present days [56]. Here we present a comparison between measurements in five direct shear devices, specifically the two "translational" devices, namely the ELE direct shear tester and the Jenike shear cell, and three "rotational" devices (The Schulze ring shear testers and the FT4 powder rheometer).

A detailed comparison between the main features of all testers is shown in Table 2.2 and a comparison of results from all these testers is presented in section 2.5. Two main characteristics of these devices are the degree of automation and the normal stress regime. The Schulze ring shear tester and the FT4 powder rheometer are in most of the operational stages completely automated, which strongly reduces the operator influences. The ELE direct shear tester can reach the highest normal stress among all the devices we investigated.

2.3.1. JENIKE SHEAR TESTER

The Jenike tester is a direct translational shear tester, developed in the 1960s [36] and it is recognized as one of the industrial standards for designing reliable bulk solids handling equipment such as storage bins, silos and hoppers. The tester consists of a shear cell ($D = 93$ mm) which includes a closed-bottom hollow base fitted to a fixed bearing plate.

A shear ring capable of moving horizontally is placed over the base with a top lid, used to close the cell, see Fig. 2.3(a). The shear cell is filled with the test sample, which rests within the base and the shear ring, as shown in Fig. 2.3(b). A normal force is applied to the shear lid by loading weight on a hanger. A shear force is then applied using a bracket and a pin on the shear ring. The bulk solid undergoes shear deformation due to the simultaneous displacement of the upper ring and the lid against the stationary bottom ring. The stem is moved by a motor at a constant speed of around 1-3 mm/minute and the shear force is measured by a force transducer and is recorded on a computer.

(a)   (b)

Figure 2.3: (a) Jenike direct shear tester and (b) the schematic representation of the Jenike shear cell. For technical details see Table 2.2. Fig. 2.3(b), reprinted with permission from author [57]. Copyright: (2002) Dietmar Schulze.

For conducting a shear test, a sample of powder is uniformly filled into the shear cell using a spatula and/or a sieve. The sample is initially pre-consolidated by twisting a special lid covering the powder bed under a certain normal load. Then the lid and the filling ring are replaced with a shear lid and the pre-consolidated sample is pre-sheared until a steady state flow is reached, which is defined as a state of constant shear force and bulk density for a given normal stress. After retracting the shear stem and reducing the normal load, the shearing process is re-initiated under a reduced normal load until a maximum shear stress is recorded. This peak value represents a single point on the yield locus. The pre-shear and shear process is repeated for lower normal loads in order to get the complete yield locus. A more detailed description of the standard testing procedure is reported in the ASTM standard D-6128 [58]. The laborious work of filling and sample conditioning as well as a potential influence of the operator are the major drawbacks of this technique.

2.3.2. ELE DIRECT SHEAR TESTER (DST)

The second direct shear tester (ELE International, United Kingdom), is illustrated in Fig. 2.4(a). It operates with specimens with a square cross-section of 60mm x 60mm and a height of 30mm. The apparatus is enclosed in a robustly constructed case. It is designed for and can reach shear stress up to 1250 kPa and normal stress up to 2778 kPa. The speed range is between 0.0001 to 2 mm/min. The ELE direct shear tester is designed for much higher load in soil testing, employs a simple shear principle as the Jenike shear cell, has a larger shear displacement range (up to 12 mm in horizontal direction) and the possibility of reverse box movement.
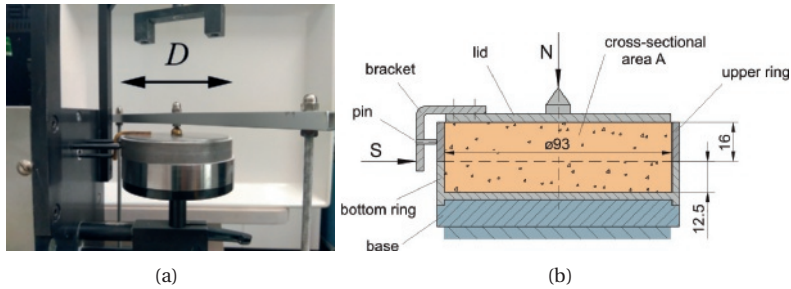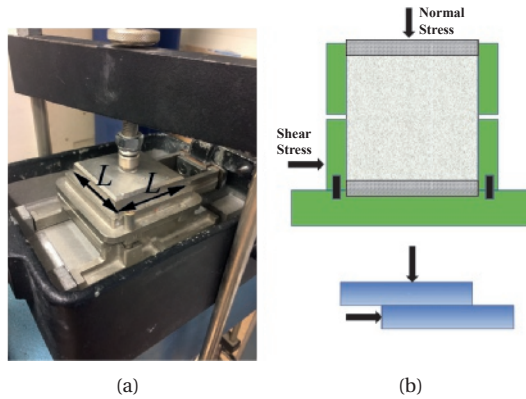
Figure 2.4: (a) The ELE direct shear tester and (b) the schematic representation of the ELE direct shear cell set-up. For technical details see Table 2.2.

The shear test sequence starts with the filling of the shear box by dry pluviation of the powder into the box until a height of approximately 40 mm is reached; then the top excess powder is removed by a scraper to ensure that the top surface of the sample is flat. Finally the top lid is mounted and the powder sticking to the sides of the box is removed carefully using a small paint brush. In addition to the typical direct shear testers as listed in Sec. 2.3.1, the main drawback for this tester is the possible ejection of powder through the inter-quadrate opening. In order to compare results in DST with other devices properly, shear tests in this study are performed following the same ASTM standard D-6128 [58] as in Jenike shear tester. For the steady state test, in analogy to the normal wall friction procedure, the sample is first sheared to steady state at the highest normal load chosen. Then step by step the normal load is decreased and shear is continued until steady state is reached.

2.3.3. SCHULZE RING SHEAR TESTER - RST-01 AND RST-XS

Among the shear devices for powder characterization, the Schulze rotational ring shear tester (1994) is one of the most widely used testers. The Schulze ring shear tester (RST-01) operates connected to a personal computer running a control software that allows the user to obtain, among other things, yield loci and wall yield loci. A smaller version of the ring shear tester with exactly the same working principle is the so-called RST-XS, developed for smaller specimen volumes (3.5 ml to 70 ml, rather than 204 ml for the RST-01). For both testers, ring-shaped (annular) bottom ring of the shear cell contains the bulk solid specimen. An annular-shaped lid is placed on top of the bulk solid specimen and it is fixed at a cross-beam (Fig. 2.5).

A normal force, F_N, is exerted on the cross-beam in the rotational axis of the shear cell and transmitted through the lid onto the specimen. Thus a normal stress is applied to the bulk solid. In order to allow small confining stress, the counterbalance force, F_A, acts in the centre of the cross-beam, created by counterweights and directed upwards,
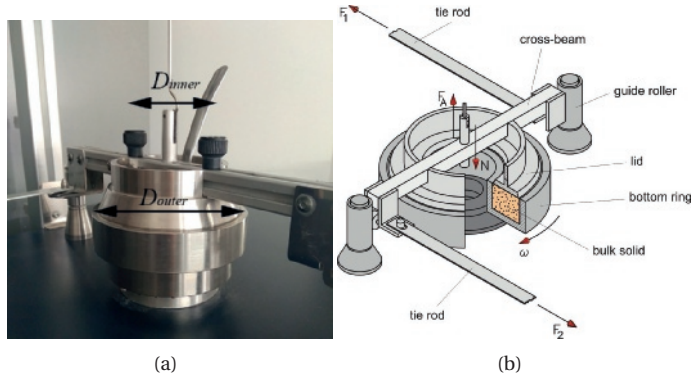
Figure 2.5: (a) The Schulze ring shear tester RST-01 and (b) the working principle of the Ring shear cell set-up. The difference between RST-XS and RST-XS is the shear cell size. For technical details see Table 2.2. Fig. 2.5(b), reprinted with permission from author [59]. Copyright: (2003) Dietmar Schulze.

counteracting the gravity forces of the lid, the hanger and the cross-beam. Shearing of the sample is achieved by rotating the bottom ring with an angular velocity ω, whereas the lid and the cross-beam are prevented from rotation by two tie-rods connected to the cross-beam. Each of the tie-rods is fixed at a load beam, so that the forces, F_1 and F_2, acting on the tie-rods can be measured. The bottom of the shear cell and the lower side of the lid are rough in order to prevent sliding of the bulk solid on these two surfaces. Therefore, rotation of the bottom ring relative to the lid creates a shear deformation within the bulk solid. Through this shearing the bulk solid is deformed, and thus a shear stress τ develops, proportional to the forces on the tie-rods ($F_1 + F_2$). All the tests performed here follow the ASTM standard [60].

2.3.4. FT4 Powder Rheometer

The last experimental equipment used in this work is the FT4 Powder Rheometer (Freeman technology Ltd., UK), depicted in Fig. 2.6(a). Standard accessories for the shear test include the 50-mm-diameter blade for sample conditioning, the vented piston for compression, the shear head for the shearing process and the 50-mm-high with 50 mm diameter borosilicate test vessel. One advantage of the commercial FT4 Powder Rheometer is the automated nature of the test procedure requiring minimal operator intervention.

The shear test sequence under the ASTM standard D7891 [61] can be summarized as follows: the test vessel is carefully filled with the powder of interest using a spatula after obtaining the tare weight. The conditioning procedure involves the movement of the conditioning blade into the test sample to gently disturb the powder bed for a user-defined number of cycles before it is removed slowly. A cycle consists of the inward and outward movement of the conditioning blade into the powder bed with a constant rotation movement all the time. In order to prevent the conditioning blade from touching the base of the vessel, the direction of the blade movement is reversed as soon as it is within 1 mm of the vessel base. It is believed that this creates a uniform, loosely packed
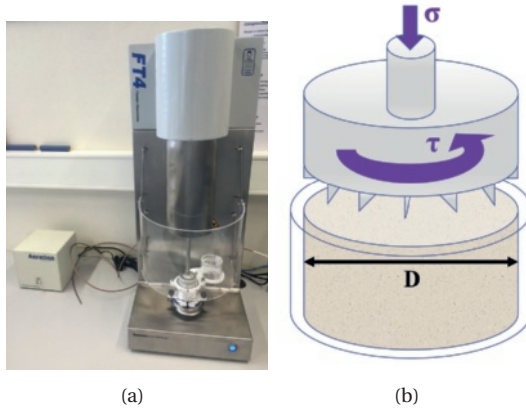
Figure 2.6: (a) The FT4 Powder Rheometer and (b) the working principle of the FT4 shear cell set-up. For technical details see Table 2.2.

test sample that can be readily reproduced [37].

In this study, we perform three pre-conditioning cycles before the shear tests are carried out (pre-conditioning does not involve a confining stress like in the other 3 testers). The portion of the base insert of the test vessel are excluded from the calculation of the vessel height, leading to a maximum vessel height of 44 mm instead of 50 mm and an aspect ratio α of 0.88. Subsequent to pre-conditioning, the blade is replaced with a vented piston, which incorporates a stainless steel mesh to allow the enclosed air in the powder to escape uniformly across the surface of the powder bed. The vessel assembly is then split (and thus levelled) after the vented piston executes the compression until the pre-shear normal stress level is reached. Then the powder mass is recorded after splitting to compute the bulk density before the shear tests start. A detailed description of the vessel split-and-levelling procedure is reported by [62].

A shear test begins after changing the vented piston to the shear head as shown in Fig. 2.6(b). The shear head moves downwards inserting the blades into the powder and induces a normal stress as the shear head bottom surface is in contact with the top of the powder. The shear head continues to move downwards until the required pre-shear normal stress is reached. At this point slow rotation of the shear head begins, inducing an increasing shear stress. As the powder bed resists the rotation of the shear head, the shear stress increases until failure, at the point a maximum shear stress is observed. As a consequence, a shear plane is formed just below the ends of the blades. The shear head is kept moving until the shear stress does not change anymore for the pre-shear step and is stopped immediately after the maximum is reached for each shear step. A constant normal stress is maintained throughout each pre-shear or shear step. Note that pre-shear in FT4 is a multi-stage process and will be discussed in the next section. All the tests performed with the FT4 powder rheometer follow ASTM standard [61].

Table 2.2: Specification comparison of the Schulze ring shear tester (RST-01), ELE direct shear tester (DST), FT4 powder rheometer (FT4) and Jenike shear cell (Jenike). The actual shear velocities used are indicated in parentheses, stars refer to the default value from control software

Property	Jenike	DST	RST-01	RST-XS	FT4
Cell volume (cm^3)	189	126	204	31.4	86.4
Cell geometry	cylinder	box	ring	ring	cylinder
Wall material	aluminium	stainless steel	aluminium	aluminium	borosilicate glass
Diameter (D) or Length (L) (cm)	9.3	6	6 (inner) 12 (outer)	3.2 (inner) 6.4 (outer)	5
Height (H) (cm)	2.8	3.5	2.4	1.3	4.4
Aspect ratio H/D or H/L	0.30	0.58	0.27	0.27	0.88
Shear displacement limit (mm)	8	10	unlimited	unlimited	unlimited
Test control	Manual	Manual	Computer	Computer	Computer
Sample weighing	offline	offline	offline	offline	on-board
Compression device	top lid	top lid	top ring	top ring	vented piston
Driving velocity	1-3 (2) (mm/min)	0.001-2 (2) (mm/min)	0.0038-22.9 (*) (°/min)	0.0038-22.9 (*) (°/min)	6-18 (6) (°/min)
Max. normal stress (kPa)	10-30	2778	50	20	22
Sample conditioning before pre-shear	pluviation (manual)	pluviation (manual)	pluviation (manual)	pluviation (manual)	rotated blade (automatic)
Yield locus test duration	2 hours	2 hours	20 mins	20 mins	30 mins
Stress measure direction	horizontal	horizontal and vertical	rotational and vertical	rotational and vertical	rotational

2.4. TEST PROCEDURES

In this section, an overview of the testing procedures as well as all the details of the tests performed using shear devices for different limestone specimens are presented.
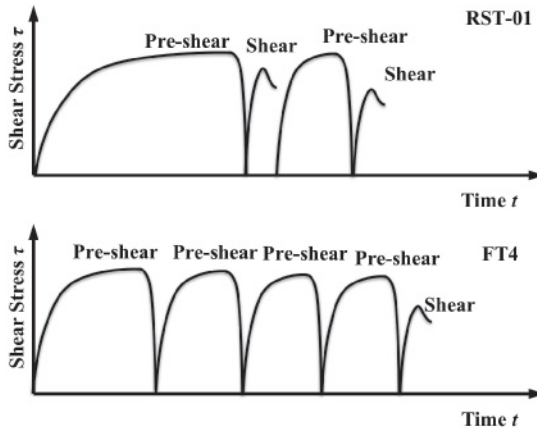
Figure 2.7: Schematic drawing of typical yield locus measurement steps for RST-01 (top) and FT4 (bottom).
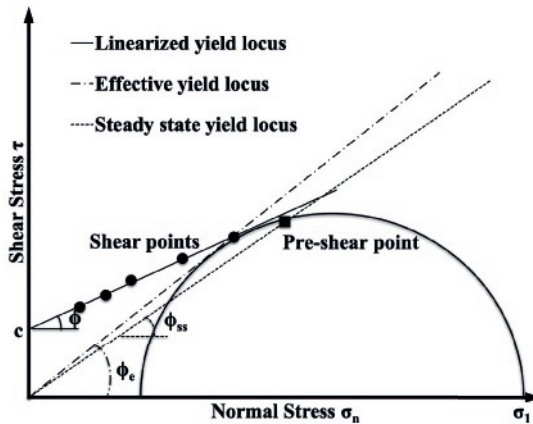
Figure 2.8: Schematic drawing of linearized yield locus, effective yield locus and steady state locus.

The diagram in Fig. 2.7 illustrates the common testing procedures used for measuring the yield locus. The Schulze ring shear tester RST-01 only requires one single pre-shear cycle before the first shear point and the steady state is reached (Fig. 2.7 top). And this pre-shear determination is also similar in the DST and Jenike. However, the FT4 powder rheometer involves multiple pre-shear cycles before the first shear is initiated, and it determines the steady state only when the difference between the end point shear stress values from two consecutive pre-shear cycles is within 1% (Fig. 2.7 bottom). The number

of multiple pre-shear cycles in the FT4 usually varies from 4 for cohesive powders to 6 for free-flowing powders. And the influence of this difference on powder flow properties will be further elaborated in Sec. 2.5.3.

The main quantities referred to in this study (linearized effective yield locus, yield locus and steady state/termination locus) are explained in Fig. 2.8, where the pre-shear and shear points are the measured values as indicated in Fig. 2.7. The connection among all the shear points is defined as yield locus, which represents the yield limit of a consolidated bulk solid. Here in Fig. 2.8, we show the linearized yield locus for only one normal stress at preshear, i.e., for one well-defined state of consolidation. If a different normal stress is applied at preshear, one will obtain a different yield locus. Then the angle of internal friction, ϕ, is represented by the slope of the linearized yield locus. A straight line through the origin of the $\sigma - \tau$ diagram, tangent to the large Mohr circle (steady-state flow), is the effective yield locus. The slope of the effective yield locus is called the effective angle of internal friction, ϕ_e. Similarly, the straight line goes through both the origin and the pre-shear point is called steady state yield locus and gives the steady state angle of internal friction, ϕ_{ss}, as depicted in Fig. 2.8 and the details are given by [41]. The intercept of yield locus for normal stress equals to zero is named as cohesive strength, σ_c, and it qualitatively indicates the bulk cohesion of a given sample under a given normal stress. Note that all the quantities measured from different testers are using the same definition here.
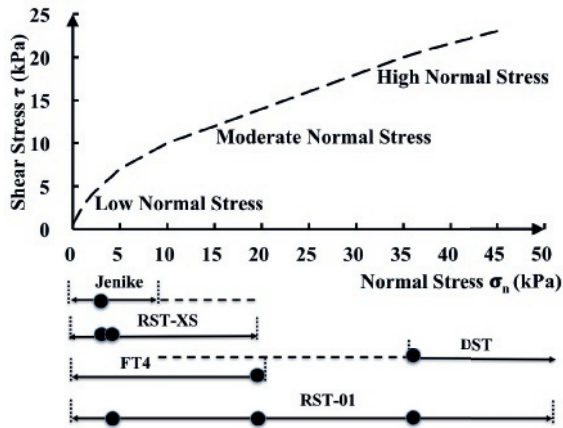
Figure 2.9: Schematic drawing of typical yield locus. Black arrows at the bottom: typical normal stress ranges used for each device; dashed lines are extended normal stress limits. Black points indicate the actual normal stress levels used for different shear testers.

Since all the devices investigated here have been designed for different purposes, they are adapted to test the materials in preferable normal stress ranges. In Fig. 2.9, we show schematically the range of normal stress that each device can cover with acceptable accuracy. In the same plot, we indicate the extended normal stress ranges of Jenike and DST (dashed lines). For Jenike in higher normal stress range, the data are highly difficult to acquire and less reliable due to insufficient shear path available in shearing direction.

Table 2.3: Summary of the tests performed. The numbering in the table are the number of powders tested with a certain device under a certain pre-shear stress level. For more details, see Table 2.5. Note that the values in the parentheses refer to the pre-shear normal stress values used for a specific device.

Stress in kPa Device	Low Stress 5 (4.3)	Moderate Stress 20	High Stress 35 (36.1)
Jenike	2 (4.3)	[-]	[-]
DST	[-]	[-]	4 (36.1)
RST-01	7	8	7
RST-XS	4 (4.3)	[-]	[-]
FT4	[-]	4	[-]

On the other hand, low/intermediate normal stress results from DST are less accurate due to the limit of the force sensor. The actual normal stresses used for this study are also highlighted with black dots on the solid lines and summarized in Table 2.5. In Fig. 2.9, we divide the whole normal stress range into three regimes: i) low normal stress, where Jenike, RST-0 1/RST-XS and FT4 can be used; ii) moderate normal stress, where RST-01 and FT4 are available; iii) high normal stress that DST and RST-01 can be relied on.

The Schulze RST-01 was chosen as a reference device and used to test all 7 Eskal samples at 3 different pre-shear normal stress levels since it covers the widest stress range. A limited number of cases were tested with the other devices depending on the accuracy and material availability. However, for each pre-shear normal stress, tests on one powder have been performed using at least two devices in order to check the reproducibility of the results between the testers. Each test was repeated three times (3 fresh samples) to investigate the repeatability within a single device.

Details on the pre-shear and shear normal stress levels used are given in Table 2.5. In addition, we have also performed steady state locus study using 4 powders in DST. We have chosen a pre-shear normal stress values between 1.4 and 36.1 kPa. The test details are summarized in Table 2.4.

2.5. COMPARISON OF SHEAR DEVICES

In this section, we compare the measurement from different shear devices and a general overview of the repeatability and reproducibility of the test results is given. In order to compare the yield loci from different testers, two limestone powders were chosen as reference powders (see Table 2.3), namely cohesive Eskal300 (2.22 μm) and free flowing Eskal150 (138 μm).

2.5.1. LOW NORMAL STRESS: SCHULZE RING SHEAR TESTER (RST-01) VS JENIKE TESTER

In the low normal stress regime, we first compare the RST-01 with the standard Jenike tester at pre-shear normal stress of 5kPa. Each shear point is measured with 3 fresh sam-

Figure 2.10: Yield locus (shear stress versus normal stress) of Eskal150 (138 μm) and Eskal300 (2.22 μm) using RST-01 and Jenike. The pre-shear normal stress is kept at 5 kPa for both devices. Points with and without lines are shear and pre-shear points, respectively. Lines are guides to the eye.

ples to acquire the standard deviations. The yield loci for Eskal150 (138 μm) and 300 (2.22 μm) are shown in Fig. 2.10. Both testers show quite good repeatability with a higher standard deviation from the Jenike tester. When we look at the individual powders, the agreement between the two shear testers for Eskal150 is good, with the difference increasing slightly with increasing normal stress. The pre-shear stress values are also close within the deviation range. For the finer Eskal300, the discrepancy between the two devices becomes higher, but still within the standard deviation. A big discrepancy is observed for the pre-shear points, where the Jenike shows lower values and higher standard deviations compared to RST-01. This may be related to the manual control procedure of the Jenike shear cell. Often the pre-shear must be stopped to prevent the risk of running out the shear displacement.

2.5.2. LOW NORMAL STRESS: SCHULZE RING SHEAR TESTER (RST-01) VS (RST-XS)

In the same low normal stress range, we have also tested the two reference powders using the smaller RST-XS, and the data are compared to RST-01 as shown in Fig. 2.11. For both devices, the repeatability is very high, with the standard deviations within the symbol size. For the free flowing Eskal150, the yield loci measured by the two devices demonstrate a very good agreement although a slightly different pre-shear normal stresses are used. For the cohesive Eskal300, data from RST-XS are consistently lower than data from RST-01. However, both devices show a non-linear behaviour with the slope (decreasing with increasing normal stress).

To further investigate RST-XS, we have tested Eskal300 in the RST-XS using the same pre-shear and shear stress levels as in RST-01, and results are also plotted in Fig. 2.11. We observe that, also in this case of same pre-shear normal stress, the RST-XS values are
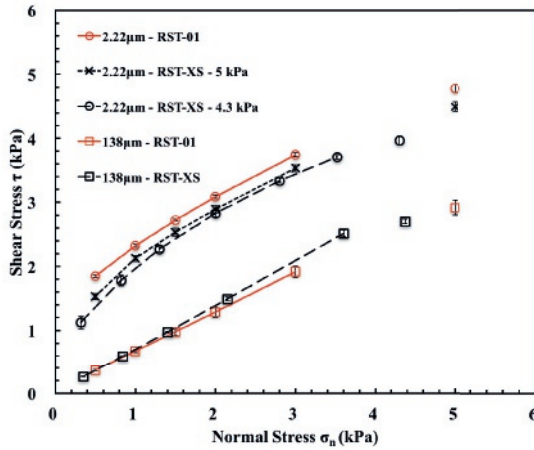
Figure 2.11: Yield locus (shear stress versus normal stress) of Eskal150 (138 μm) and Eskal300 (2.22 μm) using RST-01 and RST-XS. The pre-shear normal stresses are set to 5 and 4.3 kPa for RST-01 and RST-XS, respectively (Eskal300 has one extra 5 kPa pre-shear using RST-XS). Points with and without lines are shear and pre-shear points, respectively. Lines are guides to the eye. Note that here the data for RST-01 are the same as in Fig. 2.10.

systematically lower than the RST-01 values (around 5%). As the only known difference between RST-XS and RST-01 is the shear cell size, our results indicate that the powder response may be influenced by the system size in the case of cohesive material.

2.5.3. MODERATE NORMAL STRESS: SCHULZE RING SHEAR TESTER (RST-01) VS FT4 POWDER RHEOMETER

In the moderate normal stress regime, we compare the most commonly used rotational shear testers, the RST-01 and the FT4 rheometer. Both testers are automated and allow selection of a pre-shear normal stress value, σ_{pre}, which was set to 20 kPa for our comparison.

The yield loci for Eskal300 and Eskal150 are shown in Fig. 2.12. Both the RST-01 and the FT4 show good repeatability for each measurement point, with the standard deviations within the symbol size. For the free-flowing Eskal150, the yield loci measured by the two devices are in very good agreement except for the pre-shear points, where the FT4 gives a much lower value than the RST-01. However, for the cohesive Eskal300, we see a pronounced difference between results obtained by the two devices (around 10-20%), although the angle of internal friction (slope) between the two devices stays almost the same. A similar trend is observed with the other two cohesive samples: Eskal500 and Eskal15, with the values measured by FT4 systematically lower than the ones from RST-01 (data not shown here, for details see Tables 2.6 and 2.7).

We associate the difference in the behaviour between the two devices to the test protocols as explained in Sec. 2.4. The Schulze ring shear tester, based on the ASTM standard D-6773 [60], uses the conventional pre-shear determination criterion: the steady state shear stress plateau is determined in one pre-shear stage and the following pre-shear
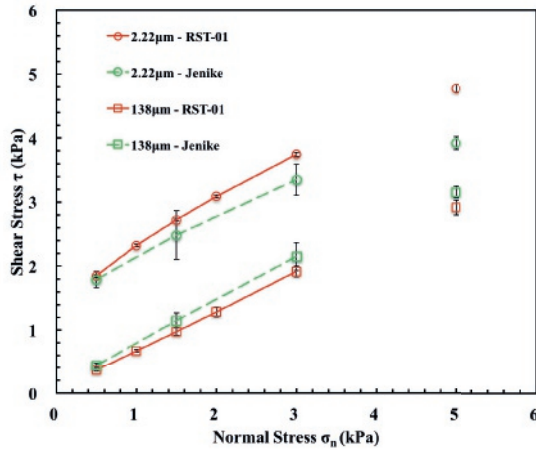
2

Figure 2.12: Yield locus (shear stress versus normal stress) of Eskal150 (138 μm) and Eskal300 (2.22 μm) using RST-01 and FT4. The pre-shear normal stress is kept at 20 kPa for both devices. Points with and without lines are shear and pre-shear points, respectively. Lines are guides to the eye.

stages after incipient flow follows this one pre-shear state value. On the other hand, for the FT4 powder rheometer, based on the ASTM standard D7891 [61], several pre-shear cycles are performed until the steady state reaches a constant shear stress value (within 1% difference). This value is the assumed as pre-shear steady state and the shear stage starts. In the case of cohesive powders, the samples need 3-10 repetitions for the pre-shear to fulfil the steady state criterion in the FT4. This may lead to formation of a pre-defined shear failure plane in the sample that reduces its shearing resistance along the shear direction. We point out here that both shear devices are automated using their own test software where the test protocols are in-built and therefore impossible to change by the users. In addition, there is another significant difference between the two testers in that the Schulze ring shear tester has an annular cross-section where the shear displacement is applied fairly uniformly over the solid shearing surface; whilst the FT4 rheometer has a circular cross-section where the shearing displacement is highly non-uniform with values decreasing towards zero at the centre of the cross-section. It is thus probable that critical shearing state may not be fully achieved particularly near the central zone of the cross-section, thereby producing a smaller overall critical shear stress.

2.5.4. High Normal Stress: Schulze Ring Shear Tester (RST-01) vs Direct Shear Tester (DST)

In the high normal stress regime, we compare the reference Schulze ring shear tester (RST-01) with the direct shear tester (DST) as shown in Fig. 2.13. The pre-shear stress σ_{pre} is set to 35 kPa for the RST-01 and 36.1 kPa for the DST. This small difference in the pre-shear normal stress applied is due to the design limitation of DST, where one can only change the normal stress discontinuously.

As we can see clearly from the figure, the results from DST and RST-01 are in good agree-
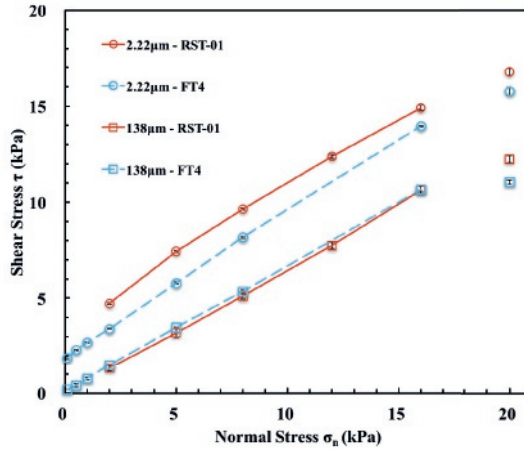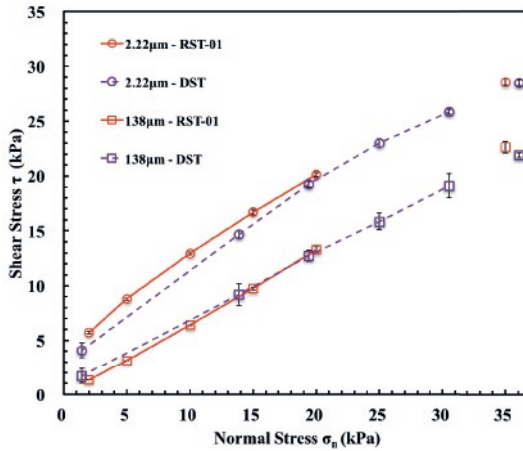
Figure 2.13: Yield locus (shear stress versus normal stress) of Eskal150 (138 μm) and Eskal300 (2.22 μm) using RST-01 and DST. The pre-shear normal stresses are kept at 35 and 36.1 kPa for RST-01 and DST, respectively. Points with and without lines are shear and pre-shear points, respectively. Lines are guides to the eye.

ment for both powders. The standard deviation of DST data is higher than the RST-01, and becomes more prominent for low stress levels as well as for the free-flowing sample Eskal150. In the case of pre-shear points, the DST shows a slightly lower value compared to the RST-01, but the difference is negligible. For the yield locus of Eskal150, data from the two devices overlap within the error bars. When we focus on Eskal300, DST underestimates the shear stress values on the yield locus with respect to the RST-01, especially for low normal stresses. We want to point out that the low stress data from DST may be less reliable that the shear force measurement system of DST has a lower limit value of 1 N (1 kPa).

Finally, in order to confirm the reproducibility between the two devices, we further test the steady state shear responses for EskalK0.1-0.5 and EskalK0.5-0.8, as shown in Fig. 2.14. Results from the two shear devices show good agreements for the tested two powders, with the data points following the two linearized yield loci within the standard deviations.

2.5.5. SUMMARY OF DEVICE COMPARISON

In order to validate the consistency of the results obtained from different shear devices, we extrapolate the linearized yield loci and compare both angle of internal friction as well as cohesive strength (interception of linearized yield locus on y-axis) for the two reference powders (Fig.s 2.15 and 2.16).

The data from different shear testers are interpreted in different ways. In the case of the yield locus from the Jenike tester and DST, the shear points are linearized using a least square method, while the RST-01, RST-XS and FT4 are linearized using the default software with pro-rating method. For a free-flowing powder, Eskal150 (138 μm), we get a good agreement among the RST-01, the RST-XS and the FT4 for the cohesive strength, c,
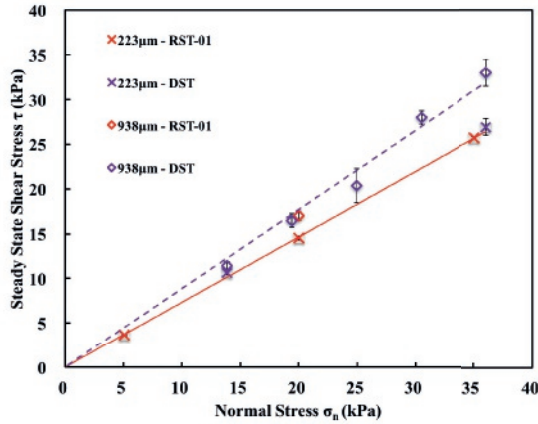
Figure 2.14: Steady state locus (shear stress versus normal stress) of EskalK0.1-0.5 (223 μm) and K0.5-0.8 (938 μm) using RST-01 and DST. The lines are the least mean square linear regression to the data with angle ϕ_{ss} = 36.2° for EskalK0.1-0.5 and 41.5° for EskalK0.5-0.8.
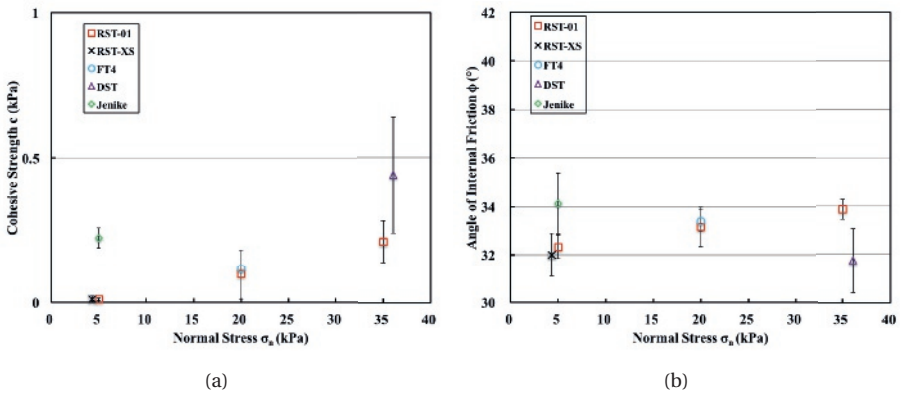
Figure 2.15: (a) Cohesive strength, c and (b) angle of internal friction, ϕ, plotted against normal stress, σ_n, for Eskal150 (138 μm tested using all the devices in this study..

but higher values from the Jenike and especially from the DST with also larger standard deviations (Fig. 2.15(a)). A similar observation is also found for the angle of internal friction as shown in Fig. 2.15(b), but the ϕ value obtained from the DST is lower than the other devices. This is caused by the limit of the direct shear tester in the low stress range (below 1.0 kPa). The direct shear tester is initially designed for measuring the strength of soil samples in civil engineering, where the stresses applied are usually high, whereas our tests were performed at much lower stress levels, close to the accuracy limit (around 0.5 kPa) of the force ring on direct shear tester, resulting in a decrease in measurement accuracy for the direct shear tester using free-flowing powders. In the case of the Jenike shear tester, the ϕ value is higher than the other devices, but still within the deviation

range.
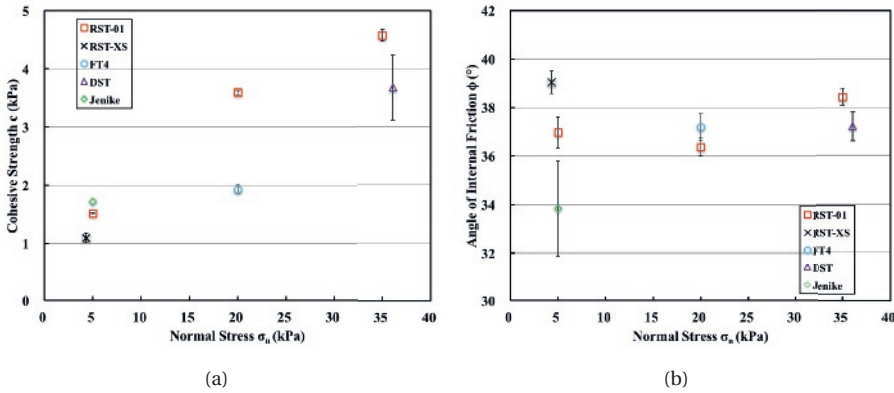
Figure 2.16: (a) Cohesive strength, c and (b) angle of internal friction, ϕ, plotted against normal stress, σ_n, for Eskal300 (2.22 μm) tested using all the devices in this study.

In Fig. 2.16, we investigate the reproducibility of all the devices by looking at the most cohesive Eskal300 powder (2.22 μm). DST shows a good agreement with the highest standard deviation for cohesive strength, c, (Fig. 2.16(a)). However, the difference between the DST and the RST-01 is around 20%. The RST-XS, Jenike and the RST-01 have a good agreement but FT4 shows a relatively lower value for c, thus underestimating the flowability of very cohesive powders. When we look at the ϕ value as shown in Fig. 2.16(b), Jenike unexpectedly gives the lowest value with the highest standard deviation. The DST shows slightly lower values than the RST-01 and the FT4 has a good agreement with the RST-01 (within deviation range). Similar behaviour is observed for two other Eskal powders tested using RST-01, RST-XS, FT4 and DST: cohesive Eskal500 and easy-flowing Eskal15 (data are not shown here, see the Tables in Appendix B). Note that the vertical axes on the left plots are different while on the right plots are the same.

2.6. EFFECTS OF VARYING PARTICLE SIZE

In this section, we present the comparison of seven Eskal powders tested by the Schulze ring shear tester (RST-01) at different pre-shear stresses as given in Table 2.3. For the analysis of RST-01 data, we used the standard RST-CONTROL 95 software with "N-RHOB-correction" activated [45]. The powders have sizes ranging from 2.22 to 938 μm, and identical chemical composition as explained in Table 2.1. We characterize the above mentioned seven powders in terms of bulk density, angle of internal friction, cohesive strength, steady state angle of internal friction, effective angle of internal friction and flow function.

2.6.1. BULK DENSITY AT STEADY STATE

As a first step, we look at the dependence of the bulk density on the normal stress and particle size for all the powders. Data are shown in Fig. 2.17(a). Zero normal stress (arrows on bulk density axis) corresponds to the initial bulk density of the fresh samples before applying any stresses (provided by the manufacturer). By increasing normal stress, the bulk density increases for all powders with different rates, higher for small-particle-size powder and almost zero for Eskal80 (71 μm) and 150 (138 μm). However, for EskalK0.1-0.5 (223 μm), the bulk density increases with increasing normal stress. We associate this trend to the wider particle size distribution (large span value 1.29 as shown in Table 2.1) and the visible huge amount of fines as shown in Fig. 2.2. A wider particle size distribution allows easy rearrangement of the packing structure when applying external load.
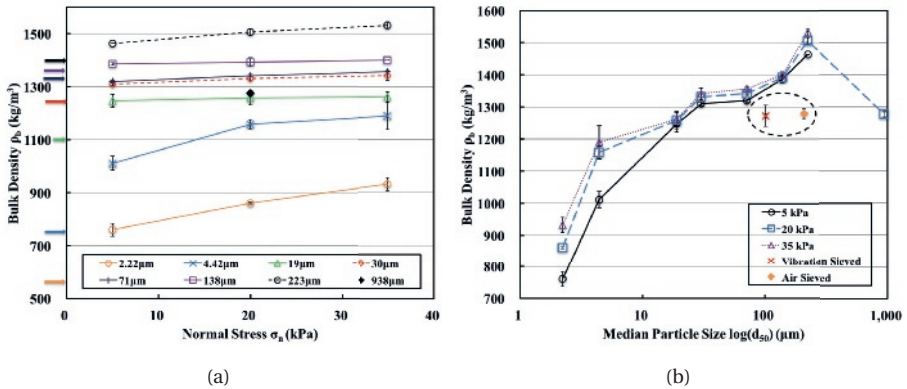
Figure 2.17: Bulk density in steady state, ρ_b, plotted against (a) normal (pre-shear) stress, σ_n, (b) median particle size, d_{50}. Arrows represent the initial bulk density of the raw samples before stress and shear are applied. Symbols in the dashed area are sieved EskalK0.1-0.5 (223μm) sample sheared at σ_n = 20 kPa. Lines are guides to the eye.

In Fig. 2.17(b), we plot the bulk density with respect to the median particle size for different normal stresses. We observe an increasing trend with increasing particle size consistent for all normal stresses. This can be explained by the presence of cohesive forces (van der Waals) between primarily particles other than gravitational forces. Since Eskal powders are relatively dry, the presence of liquid bridging and other forces are expected to be small, the dry cohesive interaction will result in forming clusters and create many voids in the bulk, and therefore decrease the bulk density. As cohesive forces become smaller with increasing size, particles will have mainly frictional and gravitational forces without forming clusters and therefore the material can form a denser bulk solid. One extra powder, EskalK0.5-0.8 (938 μm), is also tested under 20 kPa normal stress. This powder breaks the trend seen previously and shows a lower bulk density associated with the largest median particle size.

In order to investigate further the role of the span in the bulk density behaviour, we perform sieving on the sample with largest span, EskalK0.1-0.5 (223 μm). Two sieving

method are used: standard vibration sieving and high pressure air sieving. The median particle size reduce to 101 μm and 208 μm, in the case of vibration sieving and air sieving, respectively. The vibration sieving is only effective in removing the coarse particle but not the fines and thus leads to an increase of the span from 1.289 to 2.173. While the air sieving is effective enough to remove both coarse and fines and decrease the span to 0.395. The bulk densities for EskalK0.1-0.5 (223 μm) after sieving are plotted in the dashed area of the same Fig. 2.17(b). The bulk density of the sieved samples both decrease to values that are similar to the values of the largest median particle size powder, EskalK0.5-0.8 (938 μm). This indicates that for a given median particle size, the span has a dominating effect on the bulk density of a powder.

2.6.2. Bulk Responses from Incipient and Steady State Flow

Angle of Internal Friction from Incipient Flow

The angle of internal friction describes the bulk friction during incipient flow of a powder, which is determined from the linearized yield locus as shown in Fig. 2.8. Although the yield locus for cohesive powder is non-linear by nature, the linearized yield locus can still be used to estimate the angle of internal friction in a certain stress range. This estimated value is one important property that determines the maximum bulk friction of a powder from a given pre-consolidation history. Here, unless specified, all angles of internal friction originate from linearized yield loci.

In Fig. 2.18, we plot the angle of internal friction against normal stress at three different pre-shear normal stress and particle size for the 7 powders studied (EskalK0.5-0.8 is also included here but with only one point). Within the stresses investigated, there is no apparent dependence of the angle of internal friction on the normal stress (Fig. 2.18(a)). However, if we focus on the dependence on the particle size as shown in Fig. 2.18(b), we observe that when d_{50} is lower than approximately 30 μm, ϕ decreases with increasing particle size. Then, for $30 < d_{50} < 150$ μm, we observe that the ϕ is almost constant with changing particle size for the three pre-shear normal stresses chosen. Interestingly, if the particle size keeps rising to $d_{50} > 150$ μm, ϕ follows a parallel rise and achieves similar values to the ones obtained for samples smaller than 30 μm. For EskalK0.1-0.5 ($d_{50} = 223$ μm), the angle of internal friction increases back to around 38°.

We have run several tests/checks with the goal of elucidating the non-monotonic behavior that observed in Fig. 2.18(b). First, we further test another sample in the range of $d_{50} > 150$ μm, namely EskalK0.5-0.8 ($d_{50} = 938$ μm), at 20 kPa pre-shear stress. The ϕ value of EskalK0.5-0.8 increases even further to around 42°. This confirms that the increasing trend is not limited only to a specific sample. As second step, we have measured the angle of internal friction for the two sieved samples obtained after sieving EskalK0.1-0.5 (223 μm) via vibration and air methods that are already introduced in Sec. 2.6.2. While the bulk density strongly reduces after sieving, the angle of internal friction remains unaffected as shown in the dashed area of Fig. 2.18(b), which indicates that the span of particle size distribution is not the primary factor influencing the bulk friction. Finally, in order to check the influence of the devices, we have further tested EskalK0.1-0.5 (223 μm) and K0.5-0.8 (938 μm) in the direct shear tester (DST), and the results are reported in Fig. 2.14. The flow behaviour of both powders are very similar using RST-01

Figure 2.18: Angle of internal friction, ϕ, plotted against (a) pre-shear normal stress, σ_n, (b) median particle size, d_{50}. Symbols in the dashed area are sieved EskalK0.1-0.5 (223μm) sample sheared at σ_n = 20 kPa. Lines are guides to the eye.

and DST. This agreement clarifies that the behaviour originates from material properties rather than from a specific shear device.

One possible explanation of this interesting behaviour on bulk friction would be that the different size particles have a similar shape (this is visible by comparing the roundness between EskalK0.1-0.5 and K0.5-0.8 in Table 2.1) but different surface roughness/asperity, but this has to be further investigated and it is far beyond the scope of this study. Another possibility is the competition between the inter-particle cohesion and inter-particle friction (caused by shape). When the particles are small, the inter-particle cohesion dominates the flow behaviour and enhances the shear resistance. Also when a sample is confined under a given confining stress, if the inter-particle cohesion is high, the sample bulk density will be low, which gives more free spaces for particles to move around. Therefore, the geometrical interlocking does not play an important role here. When the particle size is large, we have almost no influence from inter-particle cohesion and the whole powder is more densely packed, so that the inter-particle friction/interlocking (shape/geometry) is the ruling mechanism of the bulk friction behaviour. For an intermediate particle size, these two effects are both reducing but still competing with each other, and they cannot be distinguished.

Cohesive Strength from Incipient Flow

As a complement to the angle of internal friction, one has to also look at the cohesive strength, which is the extrapolated intercept from the linearized yield locus, and gives an indication of the strength of the powder under zero confining stress (σ_n). In Fig. 2.19(a), we plot the cohesive strength against the pre-shear normal stress. As expected, the values of cohesive strength at given stress levels are higher for powders with finer particle size. The cohesive strength of all powders increases with increasing normal stress, but with different slopes. The cohesive strength of the two finest powders, Eskal300 (2.22 μm) and Eskal500 (4.42 μm), increase conspicuously with normal stress.
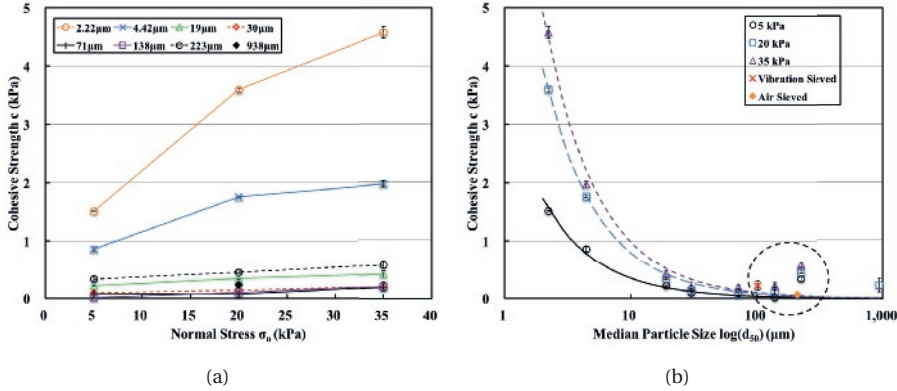
Figure 2.19: Cohesive strength, c, plotted against (a) pre-shear normal stress, σ_n, (b) median particle size, d_{50}. Symbols in the dashed area are sieved EskalK0.1-0.5 (223 μm) sample sheared at $\sigma_n = 20$ kPa. Lines are from the fitted function: $c(d_{50}) = \sigma_{pre} * d_c / d_{50}$ with $d_c = 0.6919, 0.3953$ and 0.2809 μm for $\sigma_{pre} = 5, 20$ and 35 kPa, respectively.

As we focus on the particle size dependence in Fig. 2.19(b), we see a monotonically decreasing bulk cohesion with increasing particle size for all the normal stress levels investigated. However, the cohesive strength for raw EskalK0.1-0.5 (223 μm) increases above this trend (as shown in the dashed area in the figure). This apparent discrepancy was also observed in the bulk density and the angle of internal friction, as explained earlier. We further investigated this behaviour by sieving the sample using different techniques. It seems that our air sieving procedures are effective and reduce the cohesive strength of the powder by separating the fines from the coarse fractions. the fine and coarse fractions. The theory that smaller particles have the strongest cohesive forces, acting most effectively on each other, is consistent with the strongest decrease in cohesion for the air-sieved samples in which the fines are most effectively removed. The observation of removing fines reduces bulk cohesion but does not affect bulk friction supports the hypothesis that frictional flow behaviour of powders in the range of $d_{50} > 150$ μm is governed by particle interlocking.

In Fig. 2.19(b), we have also given fitted lines based on the equation as shown in the caption. All our data fitted well with a power law dependence and this power has its origin from the adhesive forces between two particles, as introduced by Rumpf in 1990 [63, 64], where the adhesion force between two particles is linearly proportional to particle diameter: $F_{ad} \propto d$. While for the cohesive strength, it is a bulk property with an unit of stress. Therefore, cohesive strength is proportional to the adhesion force divided by effective contact area: $c \propto F_{ad}/d^2$, and finally we get $c \propto d^{-1}$, which is the relation used for our fitting.

Bulk Friction from Steady State Flow

Along with the bulk density (volume fraction), angle of internal friction and cohesive strength, the steady state angle of internal friction, ϕ_{ss}, also plays a major role in de-
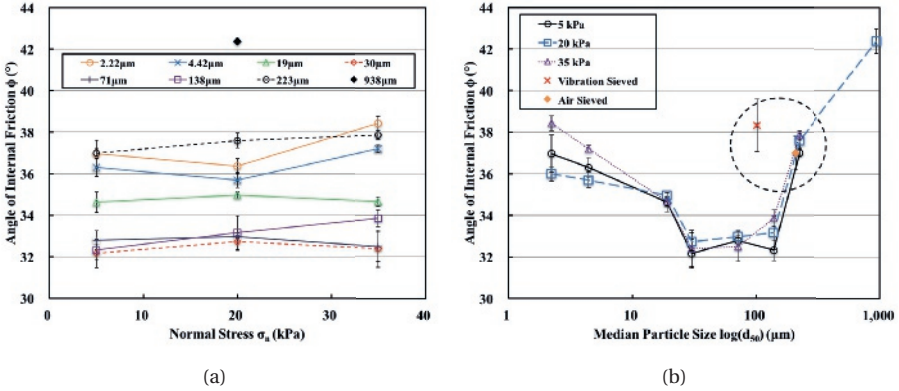
2
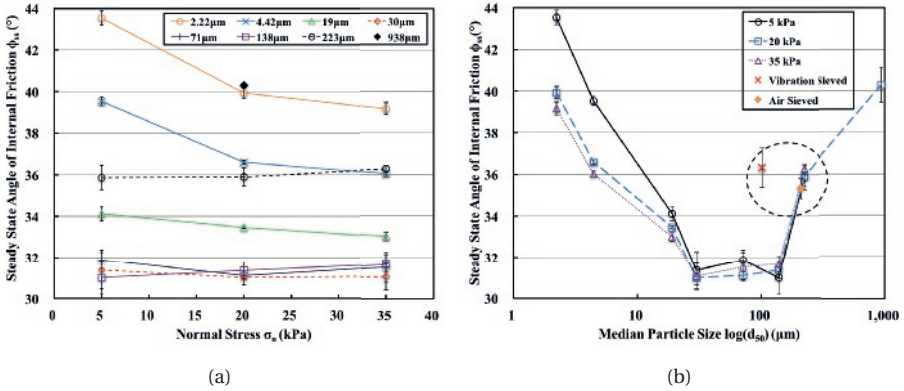
Figure 2.20: Steady state angle of internal friction, ϕ_{ss}, plotted against (a) pre-shear normal stress, σ_n, (b) median particle size, d_{50}. Symbols in the dashed area are sieved EskalK0.1-0.5 (223μm) sample sheared at σ_n = 20 kPa. Lines are guides to the eye.

termining the powder flow behaviour. The steady state flow does not depend on time change or sample history and one could get a unique bulk friction response to shearing for each normal stress level for a given sample. We first look at the ϕ_{ss} with respect to the applied normal stress in Fig. 2.20(a). For samples with median particle size higher than 20 μm (Eskal30, 80, 150 and K0.1-0.5), the ϕ_{ss} behaves similarly as ϕ, no clear dependence on normal stress is observed. However, for samples smaller than 20 μm (Eskal300, 500 and 15), ϕ_{ss} decreases with increasing normal stress.

When we look at the size influence on ϕ_{ss} in Fig. 2.20(b), we observe a very similar trend to the angle of internal friction in Fig. 2.18(b). However, the value of ϕ_{ss} for largest size powder is lower than the value of the finest powder, where ϕ of the coarsest powder exceeds the finest. This indicates that the inter-particle cohesion contributes more to the shear resistance at steady state flow than at incipient flow. When looking at the behaviour of the two sieved samples, ϕ_{ss} stay almost unchanged after sieving, which is consistent with Fig. 2.18(b).

2.6.3. QUANTITIES RELEVANT FOR SILO DESIGN

The parameters mentioned in the sections above are determined directly from the physical response of powders in the shear tester, e.g. bulk friction values can be directly calculated from the measured normal and shear stresses, and are very useful for understanding the powder's physical behaviour. However, for designing a silo, some additional parameters play an important role [41, 65, 66]. These will be discussed in the following sections.

EFFECTIVE ANGLE OF INTERNAL FRICTION

The effective angle of internal friction is defined as the angle of the effective yield locus, which is the line starting at the origin of the $\sigma_n - \tau$ plane and tangent to the Mohr circle
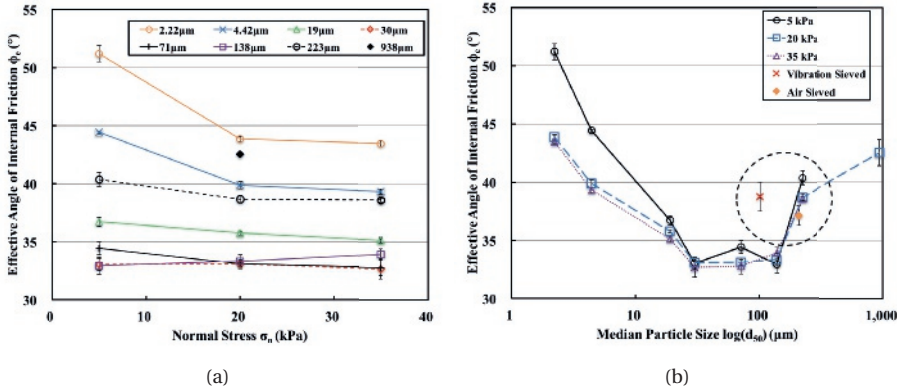
Figure 2.21: Effective angle of internal friction, ϕ_e, plotted against (a) pre-shear normal stress, σ_n, (b) median particle size, d_{50}. Symbols in the dashed area are sieved EskalK0.1-0.5 (223μm) sample sheared at σ_n = 20 kPa. Lines are guides to the eye.

(see Fig. 2.8). And this property is crucial for designing the hopper angle in order to achieve mass flow in a silo.

In Fig. 2.21, the effective angle of internal friction is plotted against the normal stress and median particle size. Within the stress levels investigated, ϕ_e decreases with increasing normal stress, except for two intermediate size powders - Eskal30 (30 μm) and 150 (138 μm), which shows a consistent behaviour with ϕ_{ss} independent of the normal stress. Interestingly, for even higher particle size, EskalK0.1-0.5 (223 μm), ϕ_e again decreases with applied normal stress.

When we focus on the dependence of the effective angle of internal friction on the particle size as shown in Fig. 2.21(b), we observe a very similar trend as ϕ and ϕ_{ss}, especially with values of ϕ_e consistently higher than ϕ_{ss} for both very fine and very coarse powders. Also in this case, sieving barely affects the behaviour of the powders, see dashed area in Fig. 2.21(b).

FLOW FUNCTION AND POWDER FLOWABILITY

Finally, we process the results to look at the powder flowability in the form of the flow function to evaluate how a given powder would fail/flow under a given major consolidation stress (see Fig. 2.8). This is also of great significance for designing the outlet diameter of a silo [67]. When a powder sample is compressed in a confined geometry, e.g. a cylinder in a uni-axial tester, the major consolidation stress is named as σ_1, which indicates the maximum compressive stress achieved in the sample. If the powder is sufficiently cohesive, it will form an intact bulk/block after the confinement is removed. If the block is compressed again, the minimum stress needed to achieve sample failure/breakage is called the unconfined yield strength, σ_c. Note that the sample stress paths in uni-axial testers and shear testers are different, but the stress states could be linked using Mohr's Circle. The curve $\sigma_c = f(\sigma_1)$ is called flow function in powder engineering, which can be

used to characterize material flowability, $ff_c = \sigma_1/\sigma_c$ [41]. The flowability is defined as follows:

- $ff_c < 1$ not flowing

- $1 < ff_c < 2$ very cohesive

- $2 < ff_c < 4$ cohesive

- $4 < ff_c < 10$ easy flowing

- $ff_c > 10$ free flowing
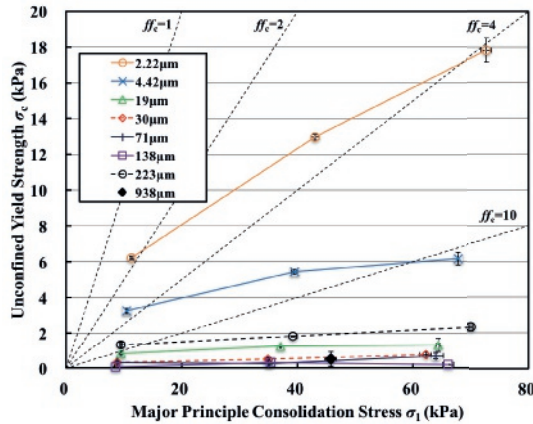
Figure 2.22: Flow function: unconfined yield strength, σ_c, plotted against major consolidation stress, σ_1 under 3 different pre-shear stresses using RST-01. Different symbols/colours represent different materials. Note that for EskalK0.5-0.8, there is only one point, and we have error bars with both σ_c and σ_1. Lines are guides to the eye.

In Fig. 2.22, we plot the flow functions for 7 limestone powders. As we can see, our powders cover almost the whole range of flowability, from cohesive to free flowing. In the stress range we investigated, σ_c increases for all the samples with increasing σ_1. As expected, the slope of the increase trend becomes higher with decreasing particle size, with the maximum slope of Eskal300 (minimum particle size). The flowability of a certain powder depends not only on the major consolidation stress σ_1, , but also on particle size.

2.7. Conclusion and Outlook

In this study, we have systematically examined the powder flow behaviour of limestone powder samples with varying median particle sizes in different shear testers at different confining stress levels. The major goal is to understand the relation between microscopic properties such as particle size and contact cohesion and macroscopic, bulk properties such as bulk density, cohesive strength and shear resistance (characterized by

the effective angle of internal friction, the internal friction at steady state flow, and the internal friction).

All shear testers investigated show highly repeatable/reproducible results and good overall, consistent agreement among each other. Direct shear devices (Jenike and ELE direct shear tester) give the highest standard deviations. The yield loci obtained by the Schulze ring shear tester (RST-01) are consistently slightly higher than the results from other testers, which, on the practical side, results in a more conservative but safer silo design. The shear protocol evidently influences the measurements as shown by comparing the RST-01 and the FT4, where the latter gives a significantly lower yield locus, which we attribute to a different pre-shear protocol. As a conclusion, while the automated devices minimize the operator influence, the output should be carefully interpreted, as differences in the protocol can result in considerable deviations in the measured material response even if the qualitative trends are found to be consistent among different testers.

In order to study the material behaviour, eight limestone powders with identical chemical composition and median particle size ranging from 2.2 μm to 938 μm have been tested in a wide range of normal stresses (5, 20 and 35 kPa). Both factors, size and stress, are found to influence the bulk flow significantly. As expected, the bulk density and cohesive strength increase with increasing normal stress, the effect being stronger for finer particles. On the other hand, the angle of internal friction seems to be unaffected by the normal stress (at least in the range investigated here), while the effective angle of internal friction and the steady state angle of internal friction show a decreasing trend with normal stress.

When we look at the dependence of the macroscopic flow on particle size, two regimes can be distinguished, above and below the median particle size of about 150 μm. For the fine particle regime, contact cohesion dominates the bulk behaviour, the effect getting smaller with increasing particle size. The bulk density increases monotonically with particle size, and the bulk cohesion (cohesive strength) decreases to nearly zero. The friction angles (effective angle of internal friction, angle of internal friction and steady state angle of internal friction), follow a similar decreasing trend as bulk cohesion.

In the coarse particle regime (150 to 938 μm), the bulk behaviour is less obvious. The bulk cohesion slightly increases while bulk density increases then decreases. The bulk friction angles increase with increasing particle size up to values comparable to those of the finest powders. In order to check the effect of small particles in this regime, fines are removed from the coarse samples via air sieving. This results in a significant reduction in bulk density and bulk cohesion, while the bulk friction angles are barely affected. This proves that the fine particles being the main source of cohesion. The competition between contact cohesion and geometrical effects can explain the transition between the two regimes. For dry powders consisting of large particles, the inter-particle cohesive forces, especially the van der Waals forces, become negligible. The interlocking between particles due to the surface roughness and shape dominates the bulk behaviour of coarse samples, while cohesion is the key contribution that governs the shear strength of fine powders. The geometrical interlocking effect is further enhanced by the increase of the bulk density for coarse samples. On the other hand, low density is associated with small median particle size, due to the presence of clusters and large pores.

For the sake of completeness, we also look at the flow behaviour of our powders, as relevant for the silo-design procedure. Overall, the flowability increases when increasing normal stress (powders become more free flowing) for finer samples, with the effect becoming weaker for coarse samples that are more free flowing anyway. The present paper is the beginning of a collection of experimental data that, in the future, can be enriched with more data from many more materials of both industrial and academic interest. Our speculations on the interesting bulk cohesion and friction behaviour with increasing particle size have to be further investigated. Furthermore, this experimental database can be used as a source for design (e.g. silo) procedures and as a benchmark for further experimental studies. Last but not least, the development, calibration and validation of particle models and simulations, especially the DEM contact models, and simulations of element tests (shear tests), require experimental data as presented here.

NOMENCLATURE

ρ_p Particle density (kg/m^3)

ρ_0 Initial bulk density (kg/m^3)

ρ_b Bulk density (kg/m^3)

w Moisture content (%)

d_{10} Particle diameter where 10% of
       distribution is below this value (μm)

d_{50} Particle median size where 50% of
       distribution is below this value (μm)

d_{90} Particle diameter where 90% of
       distribution is below this value (μm)

Ψ Roundness ([-])

τ Shear stress (kPa)

τ_{ss} Steady state shear stress (kPa)

τ_p Peak failure shear stress (kPa)

σ_n Normal stress (kPa)

σ_{pre} Pre-shear normal stress (kPa)

c Cohesive strength of yield locus
       or bulk cohesion (kPa)

c_{ss} Cohesive strength of steady state
       locus (kPa)

σ_c Unconfined yield strength (kPa)

σ_1 Major consolidation stress (kPa)

σ_2 Minor consolidation stress (kPa)

ϕ Angle of internal friction (°)

ϕ_e Effective angle of internal friction (°)

ϕ_{ss} Steady state angle of internal friction (°)

ff_c Flowability ([-])

APPENDIX A. TEST DETAILS ON YIELD LOCUS AND STEADY STATE LOCUS

Table 2.4: Summary of normal stress values applied using direct shear tester (DST) to measure steady state locus.

Samples	Normal Stress Applied (kPa)
Eskal 300, 500, 15, 150	1.4, 2.8, 4.2, 5.5, 6.9, 8.2, 9.6, 11, 12.3, 13.9, 19.4, 25, 30.5, 36.1
EskalK0.1-0.5	13.9, 36.1
EskalK0.5-0.8	13.9, 19.4, 25, 30.5, 36.1

Table 2.5: Summary of pre-shear/shear normal stress values used in each shear device to measure yield locus.

Device	Samples	Normal Stress Applied (kPa)
RST-01	Eskal 300, 500, 15, 30, 80, 150, K0.1-0.5	Pre-Shear at 5 Shear at 0.5, 1, 1.5, 2, 3
RST-01	Eskal 300, 500, 15, 30, 80, 150, K0.1-0.5, K0.5-0.8	Pre-Shear at 20 Shear at 2, 5, 8, 12, 16
RST-01	Eskal 300, 500, 15, 30, 80, 150, K0.1-0.5	Pre-Shear at 35 Shear at 2, 5, 10, 15, 20
RST-XS	Eskal 300, 500, 15, 150	Pre-Shear at 4.3 Shear at 0.35, 0,85, 1.4, 2.1, 3.6
DST	Eskal 300, 500, 15, 150	Pre-Shear at 36.1 Shear at 1.4, 13.9, 19.4, 25, 30.5
FT4	Eskal 300, 500, 15, 150	Pre-Shear at 20 Shear at 0.1, 0.5, 1, 2, 5, 8, 16
Jenike	Eskal 300, 150	Pre-Shear at 5 Shear at 0.5, 1.5, 3

APPENDIX B. TEST RESULTS OF ALL THE POWDERS AND DEVICES

2

Table 2.6: Data measured from RST-01 for several Eskal powders and different pre-shear stresses.

Device	Sample	d_{50} (µm)	σ_{pre} (kPa)	c (kPa)	σ_1 (kPa)	σ_c (kPa)	ρ_b (kg/m³)	ϕ_e (°)	ϕ (°)	ϕ_{ss} (°)
RST-01	K0.5-0.8	938	5	0.08	11.49	0.33	1288.00	41.37	40.57	38.97
			20	0.23	45.77	0.51	1275.67	42.53	42.37	40.30
			35	0.06	88.49	0.27	1299.67	42.30	42.23	41.20
	K0.1-0.5	223	5	0.33	9.47	1.33	1463.33	40.37	37.00	35.87
			20	0.45	39.23	1.82	1506.00	38.67	37.60	35.90
			35	0.58	70.17	2.33	1531.67	38.60	37.87	36.27
	Eskal150	138	5	0.01	8.53	0.06	1386.00	32.93	32.22	31.00
			20	0.10	35.34	0.31	1392.33	33.33	33.17	31.37
			35	0.21	66.07	0.19	1400.33	33.93	33.87	31.67
	Eskal80	71	5	0.08	8.88	0.31	1319.33	34.43	32.80	31.87
			20	0.07	35.02	0.25	1341.67	33.10	32.97	31.10
			35	0.19	63.9	0.68	1356.33	32.77	32.50	31.53
	Eskal30	30	5	0.09	8.83	0.31	1309.67	33.03	32.17	31.37
			20	0.14	34.84	0.49	1331.00	33.07	32.73	31.00
			35	0.20	62.20	0.74	1342.00	32.67	32.40	31.07
	Eskal15	19	5	0.21	9.44	0.82	1247.00	36.73	34.63	34.13
			20	0.34	37.08	1.23	1257.67	35.77	34.97	33.77
			35	0.42	64.34	1.31	1262.00	35.13	34.67	33.00
	Eskal500	4.42	5	0.86	10.47	3.25	1011.33	44.43	36.30	39.53
			20	1.76	39.45	5.44	1157.67	39.87	35.70	36.60
			35	1.97	67.79	6.17	1190.00	39.33	37.20	36.03
	Eskal300	2.22	5	1.52	11.33	6.21	760.67	51.20	36.97	43.53
			20	3.59	43.06	12.97	861.00	43.87	36.37	39.93
			35	4.57	72.81	17.82	932.33	43.47	38.43	39.17

Table 2.7: Data measured from RST-XS, FT4 and DST for several Eskal powders and different pre-shear stresses.

Device	Sample	d_{50} (μm)	σ_{pre} (kPa)	c (kPa)	σ_1 (kPa)	σ_c (kPa)	ρ_b (kg/m³)	ϕ_e (°)	ϕ (°)	ϕ_{ss} (°)
RST-XS	Eskal150	138	4.3	0.01	7.67	0.13	1447.67	34.13	32.00	29.93
	Eskal15	19		0.07	7.91	0.26	1416.67	34.57	33.80	32.53
	Eskal500	4.42		0.41	8.70	0.93	1015.00	40.83	38.33	37.50
	Eskal300	2.22		1.09	9.39	4.16	767.67	50.90	39.03	42.97
FT4	Eskal150	138	20	0.12	30.88	0.43	1441.45	33.75	33.41	24.91
	Eskal15	19		0.20	32.57	0.75	1297.10	33.51	32.95	29.82
	Eskal500	4.42		0.75	36.68	2.94	1081.57	37.59	35.68	34.16
	Eskal300	2.22		1.92	41.06	7.75	782.16	41.82	37.20	38.21
DST	Eskal150	138	36.08	0.86	59.83	1.95	1429.09	32.61	31.00	31.22
	Eskal15	19		1.30	60.83	3.10	1281.59	35.83	34.08	34.91
	Eskal500	4.42		2.13	61.33	7.40	1204.08	37.60	34.61	35.24
	Eskal300	2.22		3.67	64.47	10.07	952.30	42.01	37.21	38.27
Jenike	Eskal150	138	5	0.22	18.17	0.35	1445.63	35.31	34.13	32.09
	Eskal300	2.22		1.71	11.30	7.17	788.91	47.95	33.83	37.95

2

APPENDIX C. THE EXPLANATION ON THE GRAPHICAL ABSTRACT.
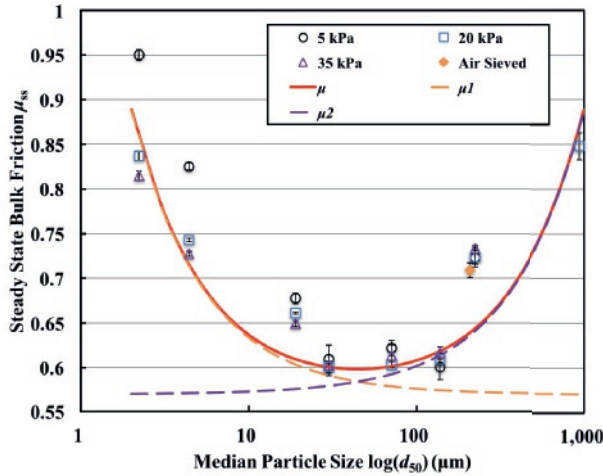
Figure 2.23: Steady state bulk friction, $\mu_{ss} = \tan(\phi_{ss})$, plotted against median particle size, d_{50}. Solid line is the fitted function, μ, in Eq. (2.1). Orange and purple dashed lines represent contributions from inter-particle cohesion and geometrical/inter-locking, respectively.

In Fig. 2.23, we have plotted the same data as shown in Fig. 2.20(b), but with a proposed theory which fits the data with $\sigma_{pre} = 20$ kPa:

$$\mu = \mu_0(1 + \frac{d_{c\mu}}{d_{50}} + \frac{d_{50}}{d_{g\mu}}) \tag{2.1}$$

where, the fitted values are $\mu_0 = 0.57$, $d_{c\mu} = 1.12$ µm and $d_{g\mu} = 1790$ µm with "c" denoting cohesion and "g" geometry. In Fig. 2.23, the curve $\mu1$ represents the first contribution inversely proportional to d_{50} due to inter-particle cohesion, which decays to zero with increasing particle size and it has the same power law as the cohesive strength, see Fig. 2.19(b). In contrast, the second term $\mu2$ is an empirical relation due to contributions from particle geometrical/inter-locking, which increases with particle size. The combination of these two contributions gives the total steady state bulk friction of the limestone powders in Eq. (2.1).

REFERENCES

[1] H. Shi, R. Mohanty, S. Chakravarty, R. Cabiscol, M. Morgeneyer, H. Zetzener, J. Y. Ooi, A. Kwade, S. Luding, and V. Magnanimo, *Effect of particle size and cohesion on powder yielding and flow,* KONA Powder and Particle Journal **35**, 226 (2018).

[2] A. J. Liu and S. R. Nagel, *Nonlinear dynamics: Jamming is not just cool any more,* Nature **396**, 21 (1998).

[3] D. Bi, J. Zhang, B. Chakraborty, and R. P. Behringer, *Jamming by shear,* Nature **480**, 355 (2011).

[4] S. Luding, *Granular matter: So much for the jamming point,* Nature **12**, 531 (2016).

[5] N. Kumar and S. Luding, *Memory of jamming–multiscale models for soft and granular matter,* Granular matter **18**, 1 (2016).

[6] M. E. Cates, M. D. Haw, and C. B. Holmes, *Dilatancy, jamming, and the physics of granulation,* Journal of Physics: Condensed Matter **17** (2005).

[7] M. Van Hecke, *Jamming of soft particles: geometry, mechanics, scaling and isostaticity,* Journal of Physics: Condensed Matter **22**, 033101 (2009).

[8] Y. Yang, W. Fei, H.-S. Yu, J. Ooi, and M. Rotter, *Experimental study of anisotropy and non-coaxiality of granular solids,* Granular Matter **17**, 189 (2015).

[9] K. A. Alshibli and S. Sture, *Shear band formation in plane strain experiments of sand,* Journal of Geotechnical and Geoenvironmental Engineering **126**, 495 (2000).

[10] A. Singh, V. Magnanimo, K. Saitoh, and S. Luding, *Effect of cohesion on shear banding in quasistatic granular materials,* Phys. Rev. E **90**, 022202+ (2014).

[11] S. C. Thakur, H. Ahmadian, J. Sun, and J. Y. Ooi, *An experimental and numerical study of packing, compression, and caking behaviour of detergent powders,* Particuology **12**, 2 (2014).

[12] F. Radjai, M. Jean, J. J. Moreau, and S. Roux, *Force Distribution in Dense Two-Dimensional Granular Systems,* Phys. Rev. Lett. **77**, 274 (1996).

[13] T. S. Majmudar and R. P. Behringer, *Contact force measurements and stress-induced anisotropy in granular materials,* Nature **435**, 1079 (2005).

[14] S. B. Savage and K. Hutter, *The motion of a finite mass of granular material down a rough incline,* J. Fluid Mech. **199**, 177 (1989).

[15] P. A. Cundall, *Numerical experiments on localization in frictional materials,* Ingenieur-Archiv **59**, 148 (1989).

[16] F. Radjai, S. Roux, and J. J. Moreau, *Contact forces in a granular packing.* Chaos **9**, 544 (1999).

[17] B. Wolf, R. Scirocco, W. J. Frith, and I. T. Norton, *Shear-induced anisotropic microstructure in phase-separated biopolymer mixtures,* Food Hydrocolloids **14**, 217 (2000).

[18] G. D. R. MiDi, *On dense granular flows,* Eur. Phys. J. E **14**, 341 (2004).

[19] J. Tomas, *Product Design of Cohesive Powders – Mechanical Properties, Compression and Flow Behavior,* Chem. Eng. Technol. **27** (2004).

[20] F. Alonso-Marroquin and H. J. Herrmann, *Ratcheting of granular materials,* Phys. Rev. Lett. **92**, 54301 (2004).

2

[21] S. Luding, *Anisotropy in cohesive, frictional granular media,* J. Phys. Condens. Matter **17** (2005).

[22] S. Luding, *Shear flow modeling of cohesive and frictional fine powder,* Powder Technol. **158**, 45 (2005).

[23] S. Luding, *Cohesive, frictional powders: contact models for tension,* Granul. Matter **10**, 235 (2008).

[24] J. Schwedes, *Review on testers for measuring flow properties of bulk solids,* Granul. Matter **5**, 1 (2003).

[25] A. W. Jenike, *Quantitative design of mass-flow bins,* Powder Technology **1**, 237 (1967).

[26] J. Schwedes and D. Schulze, *Measurement of flow properties of bulk solids,* Powder Technol. **61**, 59+ (1990).

[27] D. Schulze, *Time- and Velocity-Dependent Properties of Powders Effecting Slip-Stick Oscillations,* Chem. Eng. Technol. **26**, 1047 (2003).

[28] A. Russell, P. Müller, H. Shi, and J. Tomas, *Influences of loading rate and preloading on the mechanical properties of dry elasto-plastic granules under compression,* AIChE Journal **60**, 4037 (2014).

[29] O. I. Imole, M. Paulick, V. Magnanimo, M. Morgeneyer, B. E. Montes, M. Ramaioli, A. Kwade, and S. Luding, *Slow stress relaxation behavior of cohesive powders,* Powder technology **293**, 82 (2016).

[30] M. Morgeneyer, L. Brendel, Z. Farkas, D. Kadau, D. E. Wolf, and J. Schwedes, *Can one make a powder forget its history?* Proceedings of the 4th international conference for conveying and handling of particulate solids, Budapest , 12 (2003).

[31] M. Morgeneyer and J. Schwedes, *Investigation of powder properties using alternating strain paths,* Task Quarterly **7**, 571 (2003).

[32] H. Feise and J. Schwedes, *Investigation of the Behaviour of Cohesive Powder in the Biaxial Tester,* Kona Powder Part. J. **13**, 99 (1995).

[33] A. Casagrande, *The determination of the pre-consolidation load and its practical significance,* in *Proceedings of the international conference on soil mechanics and foundation engineering,* Vol. 3 (Harvard University Cambridge, 1936) pp. 60–64.

[34] J. Schwedes, *Vergleichende betrachtungen zum einsatz von schergeräten zur messung von schüttguteigenschaften,* Proc. PARTEC, Nürnberg , 278 (1979).

[35] S. Shibuya, T. Mitachi, and S. Tamate, *Interpretation of direct shear box testing of sands as quasi-simple shear,* Geotechnique **47**, 769 (1997).

[36] A. W. Jenike, *Storage and Flow of Solids, Bulletin No. 123,* Bulletin of the University of Utah **53**, 198 (1964).

[37] R. Freeman, *Measuring the flow properties of consolidated, conditioned and aerated powders — A comparative study using a powder rheometer and a rotational shear cell,* Powder Technol. **174**, 25 (2007).

[38] D. Schulze, *Entwicklung und Anwendung eines neuartigen Ringschergerätes,* Aufbereitungs-Technik **35**, 524 (1994).

[39] R. J. Berry, M. S. A. Bradley, and R. G. McGregor, *Brookfield powder flow tester-Results of round robin tests with CRM-116 limestone powder,* Proceedings of the Institution of Mechanical Engineers, Part E: Journal of Process Mechanical Engineering **229**, 215 (2015).

[40] H. Tsunakawa and R. Aoki, *Measurements of the failure properties of granular materials and cohesive powders,* Powder Technol. **33**, 249 (1982).

[41] D. Schulze, *Powders and bulk solids: behavior, characterization, storage and flow* (Springer, 2008).

[42] J. Harder and J. Schwedes, *The Development of a True Biaxial Shear Tester,* Part. Part. Syst. Char. **2**, 149 (1985).

[43] R. J. M. Janssen and H. Zetzener, *Measurements on cohesive powder with two biaxial shear testers,* Chem. Eng. Technol. **26**, 147 (2003).

[44] J. P. Bardet, *Experimental Soil Mechanics* (Prentice-Hall, Upper Saddle River, New Jersey, 1997).

[45] D. Schulze, *Round robin test on ring shear testers,* Adv. Powder Technol. **22**, 197 (2011).

[46] S. Kamath, V. M. Puri, H. B. Manbeck, and R. Hogg, *Flow properties of powders using four testers-measurement, comparison and assessment,* Powder Technol. **76**, 277 (1993).

[47] S. Kamath, V. M. Puri, and H. B. Manbeck, *Flow property measurement using the Jenike cell for wheat flour at various moisture contents and consolidation times,* Powder Technol. **81**, 293 (1994).

[48] R. J. Akers, *The certification of a limestone powder for jenike shear testing(crm 116),* EUR(Luxembourg) (1992).

[49] S. Koynov, B. Glasser, and F. Muzzio, *Comparison of three rotational shear cell testers: Powder flowability and bulk density,* Powder Technology **283**, 103 (2015).

[50] H. Salehi, D. Barletta, and M. Poletto, *A comparison between powder flow property testers,* Particuology **32**, 10 (2017).

[51] E. Teunou, J. J. Fitzpatrick, and E. C. Synnott, *Characterisation of food powder flowability,* Journal of Food Engineering **39**, 31 (1999).

[52] J. J. Fitzpatrick, S. A. Barringer, and T. Iqbal, *Flow property measurement of food powders and sensitivity of Jenike's hopper design methodology to the measured values,* Journal of Food Engineering **61**, 399 (2004).

[53] H. J. Feise, *A review of induced anisotropy and steady-state flow in powders,* Powder Technol. **98**, 191 (1998).

[54] H. Zetzener and J. Schwedes, *Relaxation and Creep of Dry Bulk Solids,* Part. Part. Syst. Charact. **19**, 144 (2002).

[55] W. Witt, D. Altrogge, and O. Rutsch, *High speed image analysis and dispersion for size and shape characterisation on fibres,* in *5th World Congress of Particle Technology* (2006).

[56] J. F. Carr and D. M. Walker, *An annular shear cell for granular materials,* Powder Technol. **1**, 369 (1967).

[57] D. Schulze, *Flow properties of bulk solids (v),* Deutsche Keramische Gesellschaft und Nederlandse Keramische Vereniging, Annual Meeting 2002, Eindhoven. (2002).

[58] A. D6128-16, *Standard test method for shear testing of bulk solids using the jenike shear cell,* West Conshohocken, PA: ASTM International (2006).

[59] D. Schulze, *Towards more reliability in powder testing (v),* Proceedings of the 4th international conference for conveying and handling of particulate solids (CHoPS), Budapest , 5 (2003).

[60] A. D6773-16, *Standard shear test method for bulk solids using the schulze ring shear tester,* West Conshohocken, PA: ASTM International (2008).

[61] A. D7891-15, *Standard test method for shear testing of powders using the freeman technology FT4 powder rheometer shear cell,* West Conshohocken, PA: ASTM International (2015).

[62] R. E. Freeman, J. R. Cooke, and L. C. R. Schneider, *Measuring shear properties and normal stresses generated within a rotational shear cell for consolidated and non-consolidated powders,* Powder Technol. **190**, 65 (2009).

[63] H. Rumpf, *Particle technology* (Chapman & Hall, London/New York, 1990).

[64] Y. I. Rabinovich, J. J. Adler, A. Ata, R. K. Singh, and B. M. Moudgil, *Adhesion between Nanoscale Rough Surfaces,* Journal of Colloid and Interface Science **232**, 10 (2000).

[65] A. W. Jenike, *Storage and flow of solids. Bulletin No. 123; Vol. 53, No. 26, November 1964,* Tech. Rep. (Utah Univ., Salt Lake City (USA), 1976).

[66] D. Schulze, *Verfahrenstechnische Siloauslegung,* in *Pulver und Schüttgüter* (Springer, 2014) pp. 335–360.

[67] D. Schulze, *Beispiele gemessener Fließeigenschaften,* in *Pulver und Schüttgüter* (Springer, 2014) pp. 249–268.

3

EFFECT OF PARTICLE SIZE ON POWDER COMPACTION AND TABLET STRENGTH USING LIMESTONE

*Process-ability of powders in high load compaction constitutes a challenge due to the crossed phenomena (particle rearrangement and breakage) occurring simultaneously. Previously Shi, et al. [KONA Powder and Particle Journal, **35**, 226-250 (2018)] studied the effect of particle size on the powder flow behavior during shear under low confinement pressure (5-40 kPa), as relevant for the powder processing industry. Here, compaction to 1000 times higher stress levels (10-400 MPa) is addressed in the same spirit using a compaction simulator. A set of tabletting experiments is carried out on eight Eskal limestone grades of varying particle size, over 3 orders of magnitude, maintaining the chemical composition, morphology as well as crystallinity. One goal of extending the pressure range is to compare the powder behaviours at low and high confining stresses. Second goal is relating the powder bulk properties as well as the quality properties of final tablets to the microscopic particle properties, such as median particle size and thus cohesion. As a major finding, the tablet tensile strength does not follow a monotonic trend with median particle size. For fine grade Eskal powders, the tensile strength is not sensitive to the size variation. However, for the coarse grade Eskal powders, the tensile strength decreases with median particle size at all compaction pressures. The earlier addressed geometrical effects on bulk flow, relevant for coarse grades, become irrelevant at such high pressures due to the enormous compaction, so that inter-particle cohesion seems not to be the dominating factor. The qualitative effects of both compaction pressure and particle size on the bulk density at high pressure compaction are found to be very similar compare to low pressure results.*

3.1. Introduction

Granular media are envisaged as a collection of microscopic particles which interact
through dissipative contact forces; their natural discontinuity poses many challenges
for both academia and industry in understanding their bulk behavior [1]. A continuum
description of the flow behavior of granular media is highly desirable, for application in
both natural phenomena studies and industrial applications [2].

Powders are a special class of granular material that contains fines. They may flow when
shaken or tilted, but stick when left at rest or being compressed. It is widely used in
construction, food or pharmaceutical industries. An understanding of the material me-
chanical properties is crucial in order to predict the performance of a new formulation
or to avoid segregation and poor powder flow [3]. A series of characterization techniques
with empirical indices, such as the Hausner ratio [4], the Carr's index [5] or different vari-
ants of the angle of repose [6] are used to quantify and generalize the performance of a
material. Element tests are also commonly applied to get a deeper understanding of the
influence of particle properties such as friction, cohesion, size (distributions) and shape
on the bulk mechanical responses [7–10].

During the process of high load compaction or tabletting, a bulk solid is conveyed to
a new structure with physical properties different from the original ones. Many efforts
have been made to correlate the powder flow-ability with classical instrumentation to
the performance of tabletting processes [11–14]. Experimentally, due to limited material
availability, there is still little focus on systematically studying a single micro-mechanical
parameter's influence while isolate other influences as much as possible [15, 16]. Thus, a
precise understanding of the tabletting process from a micro-mechanical point of view
is still pending. A wide range of physical phenomena occur simultaneously in very short
time and it is difficult to track the mechanics of compaction on the particle scale. Den-
sification of powders through (uni-axial) compaction takes place by four main mecha-
nisms: rearrangement, elastic deformation, plastic deformation and fragmentation. Re-
arrangement of particles is a phenomenon normally restricted to relatively low stress, as
a series of non-deformation related mechanisms such as rotation, translation and perco-
lation of fines produce an initial reallocation of particles within the bulk [17]. Elastic de-
formation can be defined as a reversible deformation of particles that after removing the
load, return to their original form [18]. Plastic deformation is an irreversible deforma-
tion mechanism occurring after reaching the yielding point, where particles start flowing
elasto-visco-plastically and remain deformed after withdrawing the load. Former phe-
nomenon are the principal densification paths for ductile powders (the paradigmatic ex-
ample is micro-crystalline cellulose), whereas for brittle specimens or agglomerates, the
elasto-plastic deformation is restricted to very low compaction forces. In this case, the
main mechanism for the densification of a bulk is particle fragmentation, an irreversible
process of diametrical and edge fragmentation [19, 20].

The goal of this study is to analyze the effect of the median particle size on the tablet-
ting performance of a series of limestone powders. Prior to the compaction, a charac-
terization of raw powders (density, size distribution, crystallographic structure, specific
surface area and flow properties) is performed in order to elucidate the interplay of mor-

phology and shape on the final tablet strength. The latter results are from a previous report on the same limestone powder specimens [16] that demonstrated a successful characterization of the flow-ability at low confining stress in correlation with their particle size. The most relevant parameters to interpret the densification paths up to very large stress and overall the quality of the final tablets are computed from acquired in-die and out-of-die data: yield pressure, in-die elastic recovery, bulk density and tensile strength.

This study is structured as follows: in section 3.2, we provide information on the limestone samples/materials, in section 3.3 the description of the experimental devices and in section 3.4 the test procedures as well as the method used for analysis. Section 3.5 is devoted to the discussion of experimental results for different compaction pressures and, particle sizes, while conclusions and outlook are presented in section 3.6.

3.2. MATERIAL DESCRIPTION AND CHARACTERIZATION

In this work, eight grades of pre-sieved limestone powders under the commercial name Eskal (KSL Staubtechnik GmbH, Germany) are used. Limestone has been used as a reference powder for standard testing [16] and calibration of equipment in powder technology, for instance, shear testers [21, 22] and optical sizing systems due to the favorable physical properties: high roundness, low porosity and an almost negligible sensitivity towards humidity and temperature changes, which allows to avoid sample pretreatment.

Each grade of the Eskal series is milled and then sieved to ensure a certain range of its particle size distribution. In the current study, the median particle size almost spans three orders of magnitude, from μm to mm. This permits to analyze the crossed-effects of cohesion, mechanical interlocking, blockiness and electrostatic forces, some of them predominant only on a reduced particle size range.

Apart from the original eight commercial grades, the air sieved fraction between 200 and 400 μm of Eskal Körnung 0.1-0.5 is also analyzed. After sieving, the very fine and coarse particles are removed which narrows down the span of the particle size distribution. The air jet sieve process is conducted using the Alpine Labortyp 200 system, which is an early model of the Hosokawa Alpine Air jet sieve e200 LS. The underpressure in Labortyp 200 system provides a continuous air flow through the sieve meshes and lifts all the small size particles and therefore separates them from large size fraction. Additional details about the test setup are provided in [16]. Note that all powders here presented are identified in most of the cases with their median particle size d_{50} in the following sections.

Table 3.1 summarizes the physical properties of the calcium carbonate samples used in the current study. The skeletal particle density ρ_p has been measured with helium pycnometry (ULTRAPYC 1200e, Quantachrome GmbH, Germany) at 0.9% moisture content. Results showed that true particle density remains in the same range (from 2748 to 2868 kg/m^3) for all the samples.

The surface structure and shape of Eskal150 and Eskal300 are analyzed by means of Scanning Electron Microscope (SEM) imaging. Materials were sputtered with silver and investigated with a field emission instrument (Helios G4 CX, FEI Deutschland GmbH,

Table 3.1: Material parameters of the experimental samples. The initial bulk density represents bulk density from raw materials. Here, K0.1-0.5 means Körnung 0.1-0.5, which follows the commercial product naming. While in the text of the paper, powders are referred to by their median particle size, d_{50}. The initial bulk density values are provided by the manufacturer.

Property (Eskal)		Unit	300	500	15	30	80	150	K0.1-0.5	Air-sieved	K0.5-0.8
Particle Size	d_{10}	μm	0.78	1.64	12	21	39	97	4.5	164	738
(Dynamic image analysis)	d_{50}	μm	**2.22**	**4.42**	**19**	**30**	**71**	**138**	**223**	**223**	**938**
	d_{90}	μm	4.15	8.25	28	43	106	194	292	292	1148
Span	$(d_{90}-d_{10})/d_{50}$	[-]	1.52	1.50	0.84	0.73	0.94	0.70	1.29	0.57	0.44
Particle density	ρ_{p}	kg/m^3	2853	2868	2799	2758	2753	2761	2775	2775	2748
Moisture content	w	%	0.9	0.9	0.9	0.9	0.9	0.9	0.9	0.9	0.9
Roundness	Ψ	[–]	0.75	0.55	0.48	0.66	0.84	0.88	0.74	0.74	0.85
Initial bulk density	ρ_0	kg/m^3	540	730	1110	1230	1330	1370	1400	1269	1276
Specific surface area	SSA	m^2/g	2.11	1.13	0.48	0.36	0.30	0.24	-	-	-
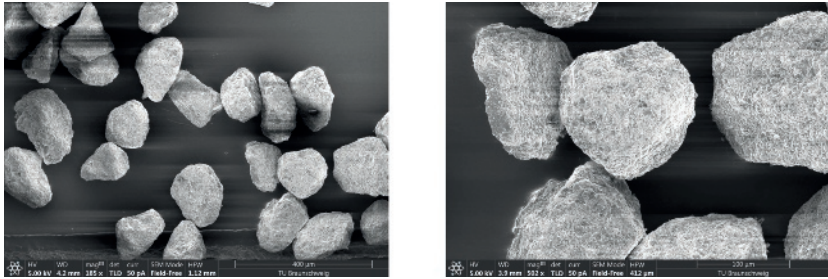
Figure 3.1: SEM images of Eskal150 (d_{50} = 138 μm) in two different magnifications: 185x (left) and 502x (right).
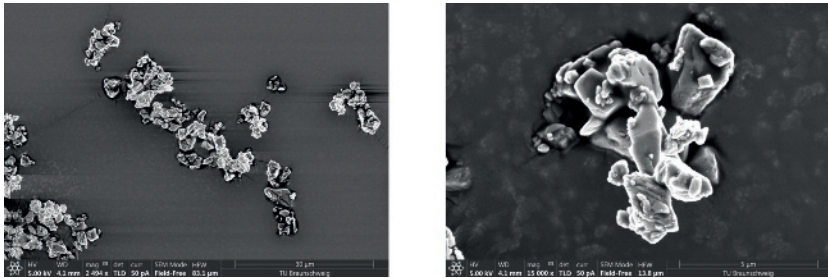
Figure 3.2: SEM images of Eskal300 (d_{50} = 2.2 μm). Magnifications: 2500x (left) and 15000x (right).

Germany) with an EDX detector, applying an acceleration voltage of 5 kV and a working distance of 4 mm. Different magnifications between 185x and 15000x were applied. Figures 3.1 and 3.2 show the SEM images of Eskal150 and Eskal300, respectively. In Fig. 3.1, it can be seen that all Eskal150 primary particles have similar shapes (left) and rough surfaces (right), and do not agglomerate. But for Eskal300 in Fig. 3.2 (left), we observe some clusters of primary particles, with an approximate size between 10 and 20 μm, which is about 5 to 10 times median particle size of Eskal300. Zooming into a single cluster as shown in the Fig. 3.2 (right), smaller fines (< 1 μm) sticking on the surface of primary particles can be clearly seen, and also that the shape of Eskal300 particles is more irregular than that of Eskal150. The other Eskal samples have mostly similar shapes, irrespective

of median particle size of the samples.

The morphology and internal structure of Eskal agglomerates is studied by powder X-ray diffraction (PXRD) and nitrogen adsorption. PXRD was carried out on vacuum-dried Eskal150, 300 and 500 samples to determine the crystal structural variations using Cu K radiation (Empyrean Cu LEF HR goniometer, Almelo, The Netherlands) on a Si sample holder in a range between 20 and 90° (2θ) with a step size of 0.05° (Empyrean series 2, PANalytical PIXcel-3D detector, Almelo, The Netherlands). Fig. 3.3 summarizes the diffraction patterns of three representative grades of Eskal. Due to the absence of a reference pattern, it is not possible to estimate neither the proportion of the crystalline and amorphous phases nor the crystallization system of the samples. However, characteristic peaks of all three samples are placed at the same diffraction angles, highlighting no significant changes on the crystallography.
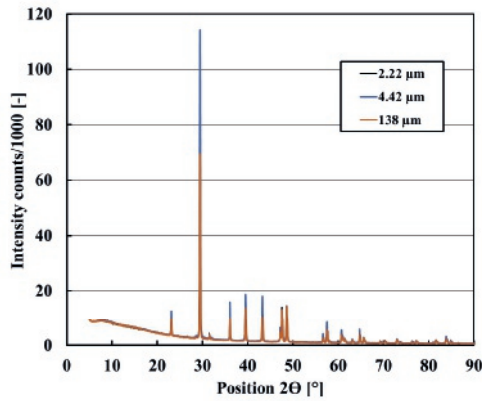
Figure 3.3: Diffraction patterns of Eskal300 (2.22 μm), Eskal500 (4.42 μm) and Eskal150 (138 μm).

The specific surface area (SSA) of Eskal is determined by nitrogen sorption using the NOVA 2000e Surface Area and Pore Size Analyzer (Quantachrome GmbH, Germany). Each limestone grade is inserted into the degassing chambers, where they are treated for 24 h at 55 °C at vacuum conditions in order to remove physisorbed compounds. Then, a conditioning interval of 500 s precedes the sorption of nitrogen at a pressure ratio with increasing relative pressure levels of 0.06, 0.12, 0.18, 0.24, and 0.30, and an absolute temperature of −196 °C. The specific surface area is calculated with the best linear fit for the BET model. As reported in Table 3.1, the specific surface area follows an inverse dependency with median particle size: the finest grades present the highest surface per unit of mass and therefore, the largest specific surface area. Thus, grades with a larger SSA exhibit a better bond-ability and thus, a higher tensile strength, as the possibility to establish an effective interaction between granules is maximized. Complementing the crystallographic patterns described in Fig. 3.3, it can be stated that all Eskal grades hereby analyzed present almost identical internal composition, morphology and shapes, which narrows down the differences in process-ability to the median particle size.

3.3. COMPACTION SIMULATOR STYL'ONE

The compaction simulator STYL'One Evolution is the machinery used for the high load compaction of limestone (Medel Pharm S.A.S, France). Standard EURO B die and punches (punch diameter d=11.38 mm) were set up in order to produce cylindrical tablets (Fig. 3.4). The compaction sequence comprises the filling of the die up to a height of 10 mm with the powder of interest (conditioned for all cases at 20°C and 45% RH for 24 h) and the symmetrical movement of the punches at a constant speed of 0.27 mm/s until the target pressure is achieved. In the current study, compaction pressures running from 10 MPa up to 400 MPa are investigated. Two distinct strategies have been followed for powder dosing. Due to the extremely high cohesivity of Eskal300 and Eskal500, a target mass of 520 mg is weighted externally and inserted manually into the die with the help of a spatula. The other grades are automatically dosed with a rotary, gravitory filling shoe, in order to speed up the compaction sequence. The poor process-ability of fine limestone powders and the extraordinarily high ejection forces exerting on the tablet press (up to 4 kN) might cause damage to the whole system and make the direct processing unfeasible. Therefore, an external lubrication with magnesium stearate (MGST) (Magnesia 4264; Magnesia GmbH, Germany) is carried out to reduce the friction with the instrumentation. Prior to a compaction sequence of 3 tablets, some MGST is gently spread on the die lateral walls, upper and lower punches and adjacent surfaces by a cotton swab.
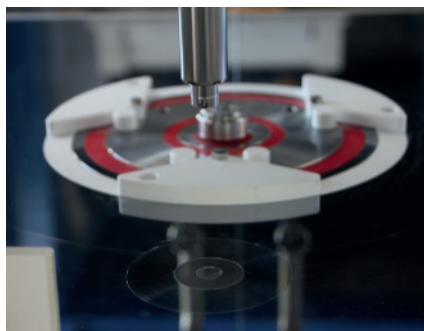
Figure 3.4: Close view of the Styl'One Compaction Simulator assembled with Kilian EURO B 11.35 mm flat punches

3.4. TEST PROCEDURES AND ANALYSIS METHOD

In this section, we present an overview of the procedures as well as all the details of the tests performed using the Compaction Simulator and tablet quality control tester for different limestone specimens.

In order to investigate the tablet-ability of the limestone grades, the maximum compression force is systematically varied from 1 to 40 kN (10 to 400 MPa). Typical tabletting pressures are commonly set above 100 MPa and the current analysis is extended to two smaller pressures (10 and 50 MPa), in order to quantify also the mechanical stability threshold at low compaction pressure.

Repeatability for a selected maximum compressive pressure is investigated by tabletting 5 different specimens. If the compressed formulation offers a stable tablet after ejection from the die, it is stored for 24 h at 20 °C and 45% RH. Then, the weight, dimensions and maximum tensile strength are extracted by means of the MultiTest 50 Manual Tablet Hardness Tester (Sotax AG, Switzerland).

Compressibility of limestone can also be analyzed with the widely reported model of Heckel [23]. This approach assimilates the process of compression with a first-order chemical reaction. On one hand, there are the pores of the tablet (the reactant) and, on the other hand, the densification of the bulk (the advance of the reaction). It is formulated as:

$$\ln\left(\frac{1}{\varepsilon}\right) = kP + A \tag{3.1}$$

where ε is the porosity of the bulk and P the applied compaction pressure. The parameter A is a constant that accounts for the particle rearrangement and $1/k$ is used to calculate apparent mean yield pressure P_y. The latter is a relevant magnitude in assessing the plasticity of the material, as a lower P_y value represents more plastically deforming material, whereas higher P_y values suggest more brittle behavior [24]. An analysis of the Heckel plots extracted with the in-die porosity and compaction pressure at the loading part of the compaction cycle is presented in Sec. 3.5.1.

3.5. RESULTS AND DISCUSSIONS

3.5.1. HECKEL ANALYSIS

(a)   (b)
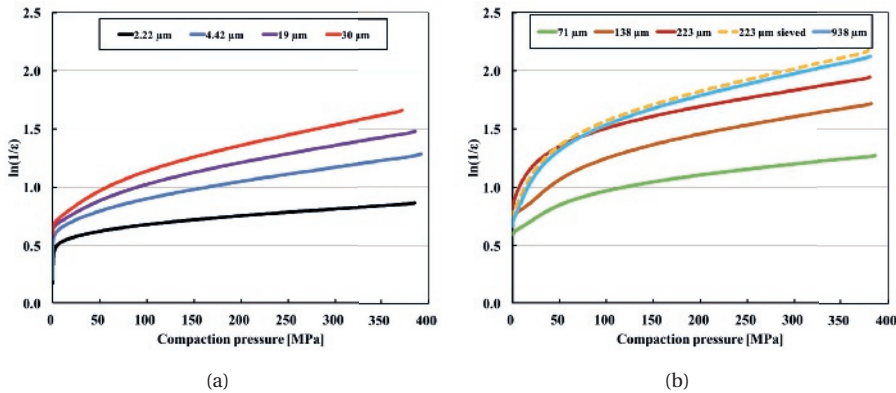
Figure 3.5: The Heckel plots for (a) fine grade Eskal powders ($d_{50} < 50\mu$m), (b) coarse grade Eskal powders ($d_{50} > 50\mu$m). Note that slopes of the curve are evaluated of compaction pressure between 100 and 300 MPa, which is not too far from linear for all the samples presented here.

In-die compaction data of the selected powders are first analyzed with the Heckel plots (Fig. 3.5). In order to enhance the readability, data is split into two groups: i) fine grades

($d_{50} < 50\mu$m); ii) coarse grades ($d_{50} > 50\mu$m). As it can be seen, all materials exhibit approximate linearity above 100 MPa, suggesting applicability of this empirical equation (3.1). A direct proportionality between bulk porosity and median particle size can then be extracted for the analyzed process conditions.

The evolution of the inverse of porosity is represented in (Fig. 3.5). P_y is fitted for the loading compaction cycles in the range 100-300 MPa. According to the classification introduced by Führer et al. [19], materials with a $P_y > 80$ MPa can be classified as hard or brittle. Regardless of the particle size, empirical observations are aligned with the results reported in Fig. 3.5 and all materials are placed above this threshold. Fine grades exhibit a more pronounced brittle behavior and a poorer process-ability.

3.5.2. EFFECT OF COMPACTION PRESSURE

In this section, the effect of compaction pressure on powder bulk properties during compaction and the final properties of the tablet are studied.

ELASTIC RECOVERY RATIO: IN-DIE AND 24 HOURS OUT-OF-DIE

The in-die axial elastic recovery (ER_{die-ax}) is defined as

$$ER_{die-ax} = \frac{\delta_{F=0} - \delta_{F=max}}{\delta_{F=max}} \tag{3.2}$$

where $\delta_{F=0}$ is the distance between the upper and the lower punch at the point of detachment during the withdrawal of the upper punch and $\delta_{F=max}$ is the distance at the target compaction pressure. ER_{die-ax} has been extracted for all calcium carbonate grades from in-die data as shown in Fig. 3.6.

Figure 3.6: In-die elastic recovery ratio plotted against compaction pressure for (a) fine grade Eskal powders ($d_{50} < 50\mu$m), (b) coarse grade Eskal powders ($d_{50} > 50\mu$m). Lines are guides to the eye.

Fine grades present larger values of in-die elastic recovery, which can be attributed to the larger strain at F_{max} (lower distance between punches) as the packing permits higher

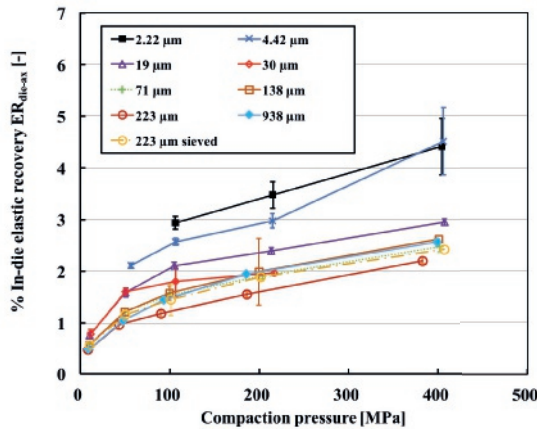particle rearrangement prior to fragmentation. For the coarse series that has median particle size larger than 30 μm, the effects of particle size are not remarkable as they all have very similar values of in-die elastic recovery except for the 223 μm grade, which is special. At the same time, for a given grade/size, by increasing the compaction pressure, ER_{die-ax} increases with a high slope when the compaction pressure is below 50 MPa but with a lower slope for the compaction pressure above 50 MPa. This is an indication of the change of the dominating mechanism from rearrangement and elasto-plastic deformation to fragmentation.

BULK DENSITY
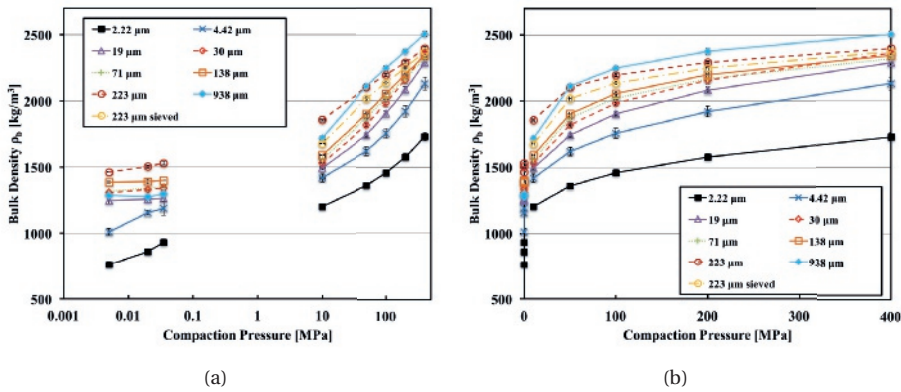
Figure 3.7: Bulk density, ρ_b, plotted against the compression pressure (a) logarithmic scale, (b) linear scale for all the powder samples with different median particle sizes. The lines are guides to the eye.

The bulk density (solid fraction) is the reciprocal of the porosity term presented in the Heckel equation and it is used hereby for better comparability with previous results [16]. Bulk density evolution with normal consolidation stress is plotted in Fig. 3.7 jointly with the data reported in [16]. Normal stress at low compaction pressure range (0.005 to 0.035 MPa) accounts for the steady state bulk density under shear of RST, while 10-400 MPa data originate from uni-axial compaction in the tablet press. Nevertheless, for all Eskal grades, the bulk density increases with the compaction pressure for both stress ranges and the qualitative increasing trend is similar and consistent. A peculiar effect is to be seen on the bulk density of the coarsest fraction: EskalK0.5-0.8 (d_{50} = 938 μm). The ρ_b series of EskalK0.5-0.8 is the largest at the highest compression, whereas for the lower normal stress, ρ_b drops significantly below the corresponding values of 138, 223 μm and 223 μm sieved fractions. This phenomenon has its origin in a dual effect. On one hand, at high load compaction, the large particles tend to fragment into smaller fractions and the geometrical effect from the confinement is fully removed. On the other hand, in the low pressure shear process, inter-particle movement is mainly taking place by sliding or rolling, which constitute low energy interactions producing tangential wear driven damage that do not affect drastically the overall bulk density. In contrast with that, the geometrical effect enhances the shear dilation pushing the shear lid upwards and thus

reduces the bulk density at the steady state.

Tensile strength

The dependence of tensile strength on the compaction pressure is shown in Fig. 3.8(a) and Fig. 3.8(b). The presentation order in the legends also corresponds to d_{50} size order, ranging from the finest grade (2.22 μm) to the coarsest (938 μm).
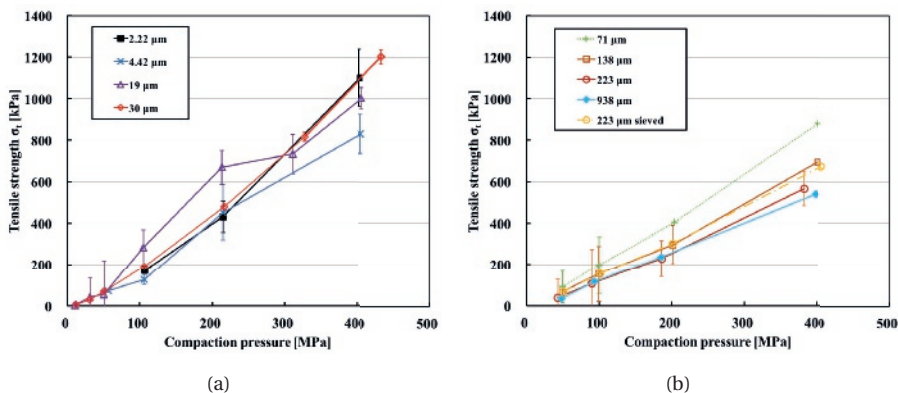
Figure 3.8: Tensile strength of tablet, σ_t, plotted against compaction pressure for (a) fine grade Eskal powders ($d_{50} < 50\mu$m), (b) coarse grade Eskal powders ($d_{50} > 50\mu$m). All the tablets here are compressed with loading rate 0.27 mm/s and punch size 11.35 mm. Lines are guides to the eye. Note that for coarse Eskal grades, the stable tablet is only formed when compaction pressure is above 50 MPa.

As expected beforehand, the tensile strength increases with compaction pressure for all samples with similar slopes for all grades by comparing fine (a) vs. coarse grades (b). As a general trend, the tensile strength at the same compaction pressure is weakly decreasing with d_{50}. This is caused by the higher bond-ability of finer particles, resulting in higher contact areas and therefore extended possibilities to from a coherent structures. This fact occurs irrespectively of the crystallographic structure and the degree of amorphicity as Subhatu et al. reported in [25]. Leaving aside the effects of crystallinity, the only morphological parameter that might alter this general tendency is particle roundness. Less rounded particles, have higher surface area and therefore, are prone to form stronger compacts. The tensile strength of 223 μm and 938 μm collapse on each other, while after removing the fines from the coarse part of 223 μm, tablets become slightly stronger. This is compatible with the principle of flow aids like aerosol: adding cohesive fines (< 30 μm) to a non-cohesive coarse powder has a negative effect on its cohesion and thus on the tablet tensile strength. The cohesive fines might not be acting as a binder between coarse particles but rather as a lubricant, making the connection between the coarse particles weaker (lower tensile strength).

3.5.3. EFFECT OF MEDIAN PARTICLE SIZE

YIELD PRESSURE

The yield pressure has been regarded as a constant describing the tendency of compacted material to undergo deformation in general. Powder deformation behavior or compressibility is assessed with the "in-die" yield pressure that derived from the linear part (100 to 300 MPa) of the Heckel curves (Fig. 3.5). Deformation described by P_y may include elastic deformation, plastic flow or fragmentation of particles. In Fig. 3.9, the yield pressure is plotted as a function of median particle size d_{50} for all our Eskal grades at highest compaction pressure 400 MPa. Here we chose only the highest compaction pressure to obtain the yield pressure because this pressure level gives a larger pressure range for the linear estimation. A poorer plasticity has been determined for the finest grades, as d_{50} goes from 2.2 μm to 938 μm and P_y changes from around 1500 MPa to about 500 MPa, with the exception of the 71 μm grade, which presents a higher P_y. By reducing primary particle size, fracturing becomes more difficult as the initiation of cracking requires more energy, and therefore, these grades exhibit higher yield pressure. If the primary particle is sufficiently small, the inter-particle cohesion force starts dominating over the external forces, which allows stable structures at low bulk density. In the same plot, we also add the yield pressure of sieved powder with d_{50} = 223 μm and the value gets lower after sieving. In other words, adding fines into a coarse grade powder has a direct effect on the increase of the yield pressure. This further confirms that enough fine particles within the bulk carry some of the stresses, leading to a larger contribution to the powder deformation tendency and result in an increased yield pressure.
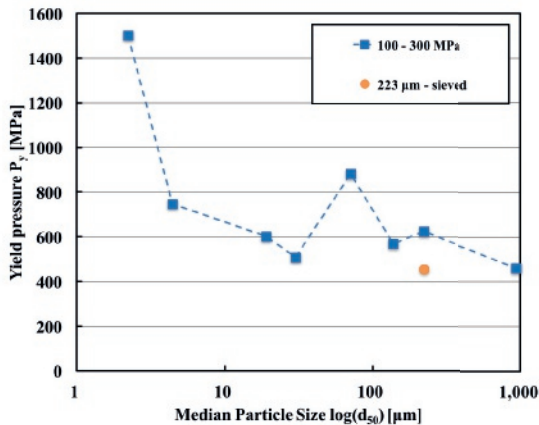
Figure 3.9: Yield pressure (P_y) plotted against median particle size (d_{50}). P_y is fitted by Eq. (3.1) to the compaction loading curves between 100 and 300 MPa.

BULK DENSITY

Sequel to the influence of compaction pressure on bulk density in Sec. 3.5.2, the influence of the median particle size in different grades of limestone powder is hereby presented. In Fig. 3.10(a), the bulk density is plotted against median particle size for dif-

ferent compaction pressures. At given compaction pressure, the bulk density increases
with the median particle size, with a similar trend for different compaction pressures.
This fact is consistent with what it was found for steady state shear conditions as shown
in Fig. 3.10(b), which is taken from [16].

(a)   (b)
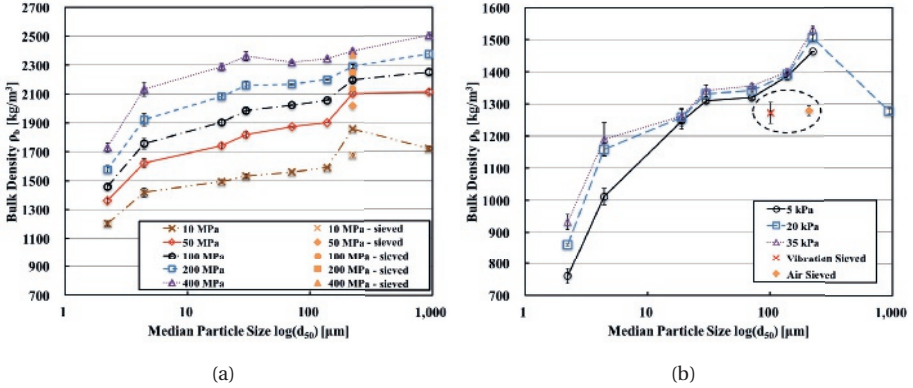
Figure 3.10: The influence of median particle size, d_{50}, on bulk density, ρ_b for different compression pressures.
(a) tabletting at pressure larger than 10 MPa, (b) steady state shear as in [16].

At the low compaction pressure/confining stress regime, however, no strong effects on
the bulk density can be seen for median particle size larger than 30 μm. At the high
pressure range, bulk density differences between two different pressure levels are larger.
This fact is attributed to different deformation mechanisms at different pressure levels.
At low pressure levels, the particles are only slightly (not yet plastically) deformed so that
the bulk density changes mainly occur due to the rearrangements accompanied by the
reduction of the free spaces between particles/clusters. At high pressures, most parti-
cles deform plastically or even fracture and thus, the bulk density changes take place in
combination with the reduction of the free space between particles and also the volume
decrease of particles themselves.

Tensile strength

Following the pressure influence on tensile strength in Sec. 3.5.2, the effect of the median
particle size is analyzed in Fig. 3.11. The compaction pressures 10 and 50 MPa are inten-
tionally neglected, because these two low pressures in most cases offer very unstable
tablets after ejection.

Unlike the previous categorization, the data here are split into two regimes: $d_{50} < 10$
μm and $d_{50} > 10$ μm and named as "very fine grades" and "normal grades", respectively.
For very fine grades, the tensile strength does fluctuate significantly with median parti-
cle size. For normal grades, a clear decreasing trend with median particle size is seen at
all compaction pressures, consistent between different grades. This effect is very simi-
lar to what was observed for the cohesive strength as introduced in [16]. Therefore, in
analogy to the cohesive strength, we introduce also here empirical fittings based on the
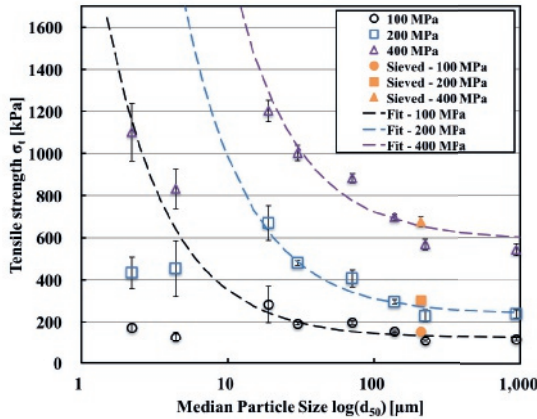
Figure 3.11: The tensile strength, σ_t, plotted against median particle size, d_{50}, for compaction pressures that can form stable tablets (σ_{max} = 100, 200 and 400 MPa). Lines are fittings using Eq. (3.3) with $d_{50} > 10$ μm at different compaction pressures with $\sigma_t = 114 * (1 + 35/d_{50})$ for 100 MPa, $\sigma_t = 227 * (1 + 35/d_{50})$ for 200 MPa and $\sigma_t = 520 * (1 + 35/d_{50})$ for 400 MPa.

particle adhesion theory proposed by Rumpf [26]: if the adhesion force $f_t \propto d$ increases linearly with the primary particle size, the tensile strength $\sigma_t \propto f_t/d^2$ is proportional to the inverse of particle size:

$$\sigma_t = \sigma_t^0(1 + d_c/d_{50}) \tag{3.3}$$

Thus, we propose an empirical function as in Eq. (3.3) and fit all the three compaction pressures separately for $d_{50} > 10$ μm. $\sigma_t^0 d_c$ represents the stiffness scale of the tablets, with σ_t^0 the tensile strength at zero cohesion and d_c the characteristic particle size where the cohesion loses its dominance. All the fitting lines agree well with each dataset and the values of σ_t^0 follow a logic increase trend with compaction pressure (slightly larger than the compaction pressure values). The characteristic particle size d_c is found to be around 35 μm for all the data presented here. The tensile strength of the 223 μm sieved grade is also reported in Sec. 3.5.2. Interestingly, the tensile strength of the latest increases after sieving, strictly the opposite evolution of yield pressure reported in Fig. 3.9. The yield strength seems not to be the main influencing factor to the strength of the final tablet, but the span of particle size distribution. To further confirm this point it is required a detailed study only focusing on the effect of the span of particle size distribution, which might constitute a key point for future work.

3.6. CONCLUSION AND OUTLOOK

In this study, we have systematically examined the powder compaction behaviour of limestone powders with varying median particle sizes at different high compaction levels in the same spirit of [16]. The major goal is to understand the relation between microscopic properties such as particle size (cohesion) and macroscopic, bulk properties such

as yield pressure, bulk density as well as tensile strength of final tablets.

The selection of limestone as a reference material has permitted to isolate and analyze the effects of the median particle size on the tabletting performance of a material. The material morphology and consistency of raw powders are examined by various characterization techniques, confirming that their properties, e.g. true particle density, particle size distribution, crystallographic structure and specific surface area are very similar among the sizes.

Measurements of the in-die stress-strain data are used to extract the yield pressure by means of the classical Heckel analysis, which is more to the practical relevance. As expected, both compaction pressure and particle size, are found to influence the compaction behaviour significantly. The yield pressure increases with the compaction pressure but decreases with the median particle size. Higher yield pressure of finest Eskal grades suggests a poorer process-ability (for both flow and compaction) and a more brittle behavior.

Following by the classical Heckel analysis, we also investigated the influences of both compaction pressure and size dependencies on the quantities that are more relevant to the compaction process or the quality of final tablets, e.g. in-die axial elastic recover, bulk density and tensile strength. When we increase the compaction pressure, the in-die axial elastic recover, bulk density (solid fraction) and tensile strength all increase. The increasing trends of bulk density found are consistent with the trends found in [16] indicating the possibility of bridging over a large range of pressures. Interestingly, if the pressure is high enough in the MPa regime, the geometrical influence of coarse particle fractions which dominates at low stress regime (kPa regime) becomes irrelevant.

When looking at the size dependence, the bulk density (solid fraction) increases with the median particle size, which qualitatively also agrees well with the bulk density at low stress shear flows. For tensile strength of final tablets, the global trend is decreasing with the increase of median particle size. We correlate this trend to the decrease of inter-particle cohesive force and proposed an empirical prediction based on the Rumpf's adhesion theory [26] that describe well this decreasing trend. However, the two fine Eskal grades (two highest yield pressure) show a more brittle behaviour and thus have lower strengths that do not follow the empirical predictions.

For future work, a detailed investigation on the mechanism that influences the quality of tablets formed only by very fine Eskal powders should be performed. Moreover, the effect of the span of the particle size distribution can be introduced by mixing/sieving of the raw commercial materials. At the same time, the interplay of process parameters such as the loading rate and the tooling size also has to be elucidated. Furthermore, the comparison of our experimental data can be used to calibration or validate simulation models of tabletting, with both DEM or continuum methods.

REFERENCES

[1] H. M. Jaeger, S. R. Nagel, and R. P. Behringer, *Granular solids, liquids, and gases,* Rev. Mod. Phys. **68**, 1259 (1996).

[2] D. B. Van de Waal, J. M. H. Verspagen, J. F. Finke, V. Vournazou, A. K. Immers, Kardinaal, L. Tonk, S. Becker, E. Van Donk, P. M. Visser, and Others, *Reversal in competitive dominance of a toxic versus non-toxic cyanobacterium in response to rising co 2,* The ISME journal **5**, 1438 (2011).

[3] M. Jivraj, L. G. Martini, and C. M. Thomson, *An overview of the different excipients useful for the direct compression of tablets,* Pharmaceutical science & technology today **3**, 58 (2000).

[4] R. Grey and J. Beddow, *On the hausner ratio and its relationship to some properties of metal powders,* Powder Technology **2**, 323 (1969).

[5] R. B. Shah, M. A. Tawakkul, and M. A. Khan, *Comparative evaluation of flow for pharmaceutical powders and granules,* Aaps Pharmscitech **9**, 250 (2008).

[6] H. M. B. Al-Hashemi and O. S. B. Al-Amoudi, *A review on the angle of repose of granular materials,* Powder Technology (2018).

[7] A. W. Jenike, *Storage and Flow of Solids, Bulletin No. 123,* Bulletin of the University of Utah **53**, 198 (1964).

[8] D. Schulze, *Entwicklung und Anwendung eines neuartigen Ringschergerätes,* Aufbereitungs-Technik **35**, 524 (1994).

[9] J. Schwedes, *Review on testers for measuring flow properties of bulk solids,* Granul. Matter **5**, 1 (2003).

[10] R. Freeman, *Measuring the flow properties of consolidated, conditioned and aerated powders - A comparative study using a powder rheometer and a rotational shear cell,* Powder Technol. **174**, 25 (2007).

[11] J. Ilkka and P. Paronen, *Prediction of the compression behaviour of powder mixtures by the heckel equation,* International journal of pharmaceutics **94**, 181 (1993).

[12] J. K. Prescott and R. A. Barnum, *On powder flowability,* Pharmaceutical technology **24**, 60 (2000).

[13] Q. Li, V. Rudolph, B. Weigl, and A. Earl, *Interparticle van der Waals force in powder flowability and compactibility,* Int. J. Pharm. **280**, 77 (2004).

[14] G. Morin and L. Briens, *The effect of lubricants on powder flowability for pharmaceutical application,* Aaps Pharmscitech **14**, 1158 (2013).

[15] M. G. Herting and P. Kleinebudde, *Roll compaction/dry granulation: Effect of raw material particle size on granule and tablet properties,* International Journal of Pharmaceutics **338**, 110 (2007).

[16] H. Shi, R. Mohanty, S. Chakravarty, R. Cabiscol, M. Morgeneyer, H. Zetzener, J. Y. Ooi, A. Kwade, S. Luding, and V. Magnanimo, *Effect of particle size and cohesion on powder yielding and flow,* KONA Powder and Particle Journal **35**, 226 (2018).

3

[17] J. Liu and P. David, *Particle rearrangement during powder compaction,* Metallurgical and Materials Transactions A **32**, 3117 (2001).

[18] I. Ilić, B. Govedarica, S. Srčič, *et al.*, *Deformation properties of pharmaceutical excipients determined using an in-die and out-die method,* International journal of pharmaceutics **446**, 6 (2013).

[19] G. Alderborn and C. Nystrom, *Pharmaceutical Powder ComPattion Technology* (CRC Press, 1995).

[20] R. Cabiscol, J. Finke, H. Zetzener, and A. Kwade, *Characterization of mechanical property distributions on tablet surfaces,* Pharmaceutics **10**, 184 (2018).

[21] H. J. Feise, *A review of induced anisotropy and steady-state flow in powders,* Powder Technol. **98**, 191 (1998).

[22] H. Zetzener and J. Schwedes, *Relaxation and Creep of Dry Bulk Solids,* Part. Part. Syst. Charact. **19**, 144 (2002).

[23] R. Heckel, *Density-pressure relationships in powder compaction,* Trans Metall Soc AIME **221**, 671 (1961).

[24] J. Nordström, K. Welch, G. Frenning, and G. Alderborn, *On the role of granule yield strength for the compactibility of granular solids,* Journal of pharmaceutical sciences **97**, 4807 (2008).

[25] T. Sebhatu and G. Alderborn, *Relationships between the effective interparticulate contact area and the tensile strength of tablets of amorphous and crystalline lactose of varying particle size,* European journal of pharmaceutical sciences **8**, 235 (1999).

[26] H. Rumpf, *Particle technology* (Chapman & Hall, London/New York, 1990).

4

STRETCHING THE LIMIT OF DYNAMIC AND QUASI-STATIC FLOW TESTING ON LIMESTONE POWDERS

Granular materials are ubiquitous in our daily life. A special class of them is powders consisting of fine particles that may flow when shaken or tilted, but stick when left at rest or being compressed, during storage and transport in powder processing industry. In order to measure the complex flow properties of powders, a variety of characterization techniques have been proposed: the (static) angle of repose measurement, the quasi-static tapped density measurement, the dynamic rotating drum or rotating blade systems inspired by liquid rheometer or standard shear testing procedure. These techniques are based on different geometries with very different flow fields under different confining stresses, and make the cross link between different techniques non-trivial. As a consequence, results are traditionally considered dependent on specific technique and only valid for that geometry/pressure/flow profile. In this study, we attempt to bridge the gap between the static angle of repose test, the dynamic rotating drum measurement and the quasi-static ring shear test using free flowing and cohesive limestone powders, differing only in median particle size. This connection between different tests opens new perspectives in the field of powder flow characterization for measurement interpretation and also for a better link with powder behavior in industrial process lines. Choosing the low speed limit of a dynamic drum test and the low stress limit for quasi-static shear test, the drum flowing angle and the shear cell friction angle are converging for both free flowing and cohesive limestone powders. Moreover, the repose angle is linked to the flowing angle in the rotating drum extrapolated to zero speed with a small deviation for cohesive powder that is sensible to its pre-stress history.

4.1. INTRODUCTION

Granular media are envisaged as a collection of microscopic particles which interact through dissipative contact forces; their natural discontinuity poses many challenges for both academia and industry in understanding their bulk behavior [1].

Since decades, granular media have been subjects of many studies, ranging from static conditions to flowing, from hard to soft-particles. Micro-mechanical studies of granular materials gives an essential understanding of their macro-scale behavior. For example, at micro or meso scale, the study by Radjai et al. [2] classifies the contacts into subnetworks of strong and weak contacts, and show that the anisotropic shear stress of granular materials is primarily carried by the strong contacts. This method offers insight into the micro structure change from the contact origin but has its limitation on studying the real life materials, e.g. limestone powders, etc.

At macroscopic scale, from the perspective of granular flow, researchers have investigated different dynamic flow configurations like plane shear, Couette cell, silos, flows down an inclined plane, or avalanches on piles and in rotating drums [3–11], where the granular materials are usually under very low or even free surface conditions. From the perspective of material characterization, researchers have developed various element tests in the lab to quantify the bulk responses of granular materials under specific stress/strain conditions. Element tests are (ideally homogeneous) macroscopic laboratory tests in which the force (stress) and/or displacement (strain) path are controlled. One of the most widely performed element test in both industry and academia is the shear test [12–20], where a granular sample is sheared until failure is reached and the material starts to flow. Here, the shear zone is pre-defined by the device design, and the shear failure is forced in a specific physical location. Other common element tests are the uni-axial compression tester [21–23] and bi-axial shear box [24–26], where the shear zone develops according to the applied state of stress.

Almost all the element tests shown in literature are done in static to quasi-static regimes, with the stress applied usually above a few hundred pascals, while the granular flow tests mentioned above are normally under dynamic, low stress conditions. The link between the dynamic and quasi-static to even static tests is still missing and represents a great challenge. Therefore, in this study, we try to explore the connection between the two types of test by stretching their limits: explore the dynamic rotating drum towards very low rotation rate, hence going to quasi-static regime; and bring the quasi-static ring shear tests towards very low confining stress condition, thus matching the stress conditions in the dynamic drum test.

This study is structured as follows. Section 4.2 introduces the limestone materials, in section 4.3 the description of the experimental devices and the test procedures. Section 4.4 is devoted to the discussion of experimental results and finding the link between dynamic and quasi-static tests, while conclusions and outlook are presented in section 4.5.

4.2. MATERIAL DESCRIPTION AND CHARACTERIZATION

Limestone powder is a widely used powder in fields ranging from construction to automotive industries. In this work, eight grades of pre-sieved limestone powder under the commercial name Eskal (KSL Staubtechnik GmbH, Germany) are used. Eskal has been used as a reference powder for standard testing [20] and calibration of equipment in powder technology, for instance, shear testers [27, 28] and optical sizing systems due to the favourable physical properties: high roundness, low porosity and an almost negligible sensitivity towards humidity and temperature changes, which allows to avoid sample pretreatment.

Each grade of the Eskal series is milled and then sieved to ensure a certain particle size distribution. Two grades of Eskal are chosen specifically from the experience in previous study [20]: fine/cohesive Eskal300 (d_{50} = 2.22 μm) and coarse/free-flowing Eskal150 (d_{50} = 138 μm). The details of their physical properties are summarized in Table 4.1.

Table 4.1: Material parameters of the experimental samples. The initial bulk density represents bulk density from raw materials. The initial bulk density values are provided by the manufacturer.

Property		Unit	Eskal 300	Eskal150
	d_{10}	μm	0.78	97
Particle Size	d_{50}	μm	**2.22**	**138**
	d_{90}	μm	4.15	194
Span	$(d_{90}-d_{10})/d_{50}$	[-]	1.52	0.70
Particle density	ρ_{p}	kg/m^3	2853	2761
Moisture content	w	%	0.9	0.9
Roundness	Ψ	[–]	0.75	0.88
Initial bulk density	ρ_0	kg/m^3	540	1370
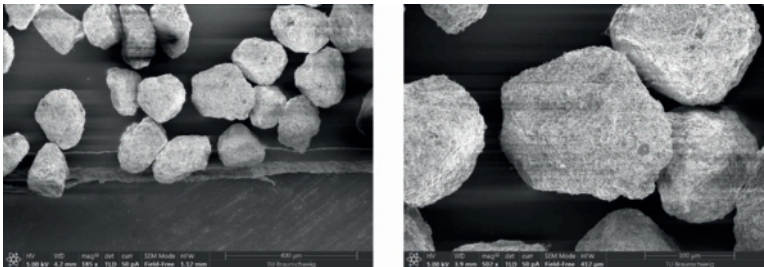
Figure 4.1: SEM images of Eskal150 (d_{50} = 138 μm) in two different magnifications: 185x (left) and 502x (right).

The aspect, shape and morphology of Eskal150 and Eskal300 are analyzed by means of Scanning Electron Microscope (SEM) imaging. Materials were sputtered with silver and investigated with a field emission instrument (Helios G4 CX, FEI Deutschland GmbH, Germany) with an EDX detector, applying an acceleration voltage of 5 kV and a working distance of 4 or 6 mm. Different magnifications between 185x and 15000x were applied.
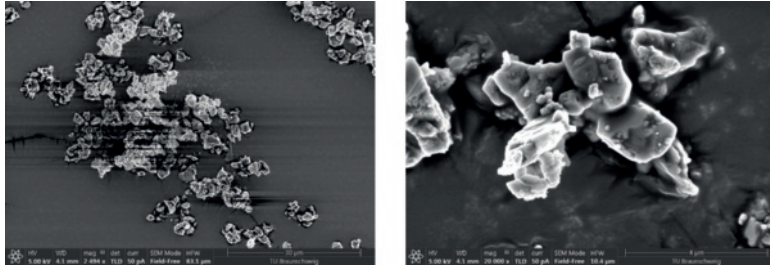
Figure 4.2: SEM images of Eskal300 (d_{50} = 2.2 μm). Magnifications: 2500x (left) and 15000x (right).

Figures 4.1 and 4.2 show the SEM images of Eskal150 and Eskal300, respectively. In Fig. 4.1, we see that all the Eskal150 primary particles have similar shapes (left) and rough surfaces (right), and every particle is clearly distinguished/separated from the others. But for Eskal300 in Fig. 4.2 (left), we observe some clusters of primary particles, and the size of clusters are typically around 10 to 20 μm, which is about 5 to 10 times median particle size of Eskal300. When we zoom into a smaller scale, focusing on one single cluster as shown in the Fig. 4.2 (right), we see even smaller fines (< 1 μm) sticking on the surface of primary particles. Moreover, the shape of Eskal300 particles are more irregular than Eskal150 particles.

4.3. Experimental Setup

In this study, we combine three experimental devices: GranuHeap (Angle of Repose), Schulze ring shear tester (Steady state friction angle), and GranuDrum (Dynamic flowing angle), to perform measurements in both static and dynamic regimes. The details of each setup are shown in Fig. 4.3 and will be explained in the following.
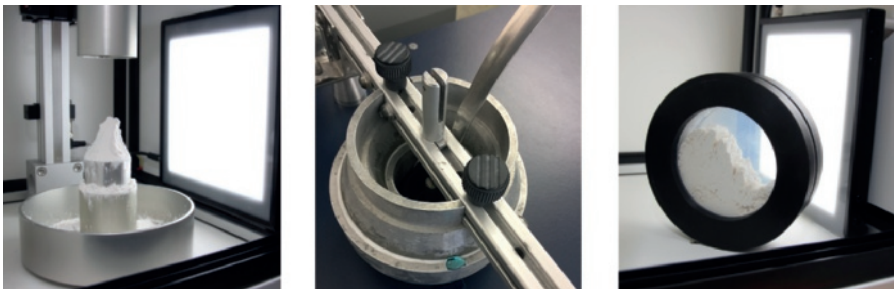
Figure 4.3: Left: GranuHeap for measuring angle of repose; middle: the Schulze ring shear tester RST-01.pc; right: GranuDrum for measuring the dynamic flowing angle.

4.3.1. GranuHeap - Static Free Surface

GranuHeap instrument [10] is an automated repose angle measurement device based on image processing. A powder heap is created on a cylindrical support to be analyzed

by image processing. The geometry of the measurement and a typical heap cell are presented in Fig. 4.3 (left). In order to obtain reproducible results, an initialization tube with an internal diameter equal to the circular support is installed on the support. After filling the initialization tube by hand with a fixed volume of powder (100 ml in the case of the present study), the tube moves up at a constant speed of 5 mm/s. Thereby, the powder is flowing from the tube to form a heap on the cylindrical support, which is then evaluated by image analysis. A controlled rotation of the support allows obtaining different heap projections. In the present study, 16 images separated by a rotation of 11.25° were recorded. A custom image recognition algorithm determines the position of the powder/air interface. The repose angle α_r refers to the angle of the isosceles triangle with the same projected surface as the powder heap. The isosceles triangle corresponds to the ideal heap shape. The lower the repose angle is, the better the powder flowability is [10].

4

4.3.2. SCHULZE RING SHEAR TESTER - RST-01 - QUASI-STATIC CONFINED SURFACE

Shear tester is used for powder characterization since decades, the Schulze rotational ring shear tester (1994) is one of the most widely used testers and it is semi-automated. The Schulze ring shear tester (RST-01) operates connected to a personal computer running a control software that allows the user to obtain, among other things, yield loci and wall yield loci. The ring-shaped (annular) bottom ring of the shear cell contains the bulk solid specimen. An annular-shaped lid is placed on top of the bulk solid specimen and it is fixed at a cross-beam (Fig. 4.3 middle). A normal force, F_N, is exerted on the cross-beam in the rotational axis of the shear cell and transmitted through the lid onto the specimen. Thus a normal stress is applied to the bulk solid. In order to allow small confining stress, the counterbalance force, F_A, acts in the centre of the cross-beam, created by counterweights and directed upwards, counteracting the gravity forces of the lid, the hanger and the cross-beam. Shearing of the sample is achieved by rotating the bottom ring with an angular velocity ω, whereas the lid and the cross-beam are prevented from rotation by two tie-rods connected to the cross-beam. Each of the tie-rods is fixed at a load beam, so that the forces, F_1 and F_2, acting on the tie-rods can be measured. The bottom of the shear cell and the lower side of the lid are rough in order to prevent sliding of the bulk solid on these two surfaces. Therefore, rotation of the bottom ring relative to the lid creates a shear deformation within the bulk solid. Through this shearing the bulk solid is deformed, and thus a shear stress τ develops, proportional to the forces on the tie-rods ($F_1 + F_2$). All the tests performed here follow the procedure as in ASTM standard [29].

The typical confining pressure used in the shear cell tests are between 1 and 10 kPa. However, this is too high compared to the pressure range of free or nearly free surface. Thus, in order to explore the low confining pressure regime, we employ the pre-shear normal stresses down to the device's lowest limit: 2, 1.5, 1.0, 0.8, 0.6, 0.4, 0.2 and 0.1 kPa. For cohesive Eskal300, we could apply the pre-shear normal stresses down to 0.1 kPa, while for free-flowing Eskal150, this minimum limit stays at 0.2 kPa. And in order to achieve very low pre-shear normal stress in RST-01, we use a special shear cell made of

PVC instead of aluminium, which has a lower self weight of the lid and allows to apply very low stress. However, the pre-consolidation becomes questionable and the output are not representative. For each sample on each pre-shear normal stress, we performed the test for three runs with 3 fresh samples in order to investigate repeatability. In all tests here, the shear velocity is kept constant as default to ensure the shearing is within the quasi-static regime.

4.3.3. GRANUDRUM - DYNAMIC FREE SURFACE

The GranuDrum instrument [10] is an automated powder flowability measurement technique based on the rotating drum geometry, which characterizes materials at dynamic flowing regime. A horizontal cylinder with vertical glass side walls called drum is half filled with the sample of powder. For the present study, the drum rotates around its axis at rotating speeds from 2 RPM to 10 RPM and we do not analyze the flow during the rotating speed decrease sequence. A CCD camera takes snapshots (50 images separated by 0.5s) at each angular velocity (see Fig. 4.3 right). The air/powder interface is detected on each snapshot with an edge detection algorithm. Afterward, the average interface position and the fluctuations around this average position are computed. Then, for each rotating speed, the flow angle α_f is measured at the center of the average interface position. A dynamic cohesive index σ_f can be also measured from the interface fluctuations.

4.4. RESULTS AND DISCUSSION

4.4.1. STATIC GRANULAR HEAP

Fig. 4.4 shows two typical heaps obtained with Eskal150 (left) and Eskal300 (right). The cohesive Eskal300 powder makes strongly irregular heap with a high repose angle ($\alpha_r = 69.1 \pm 1.9°$) due to the influence of cohesion between particles. As the opposite, the heap obtained with Eskal150 has almost conic shape with a low repose angle ($\alpha_r = 33.0 \pm 0.1°$). The repose angle measurement of each Eskal powder has been repeated four times with fresh samples to obtain a representative value with standard deviations. Moreover, in each single measurement, the stably formed heap were rotated slowly to take 16 pictures at different viewing angles from the side of the heap.
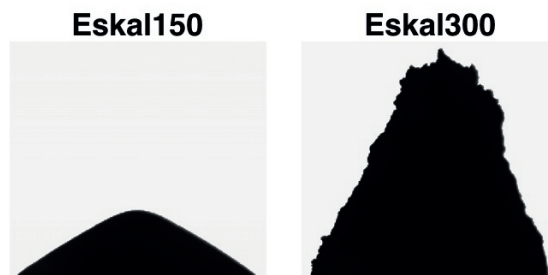
Figure 4.4: Typical heaps obtained with Eskal150 and Eskal300.

4.4.2. Quasi-Static Ring Shear Tester
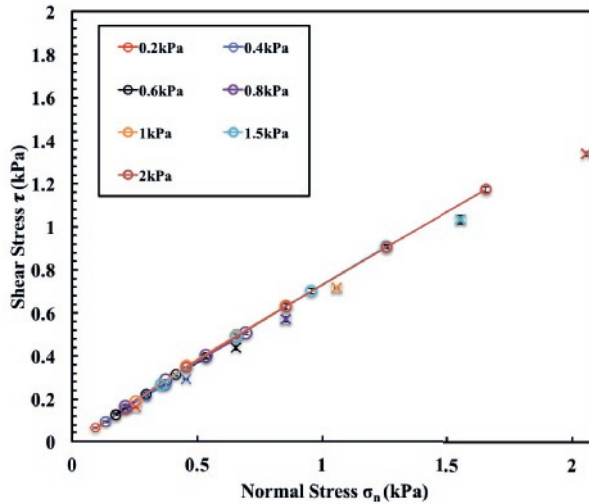
Figure 4.5: Yield locus (shear stress versus normal stress) of Eskal150 (138 μm) using RST-01.pc. The pre-shear normal stress is kept between 0.2 and 2 kPa. Points with and without lines are shear and pre-shear points, respectively. Lines are only guides to the eye.

In the low normal stress regime, we first look at the yield loci at different pre-shear stresses (0.2 to 2 kPa). Each yield locus is measured with 3 fresh samples to acquire the standard deviations. The yield loci for Eskal150 (138 μm) are shown in Fig. 4.5. With increase in pre-shear normal stress, all the yield loci collapse on a single curve. This is expected behaviour for free flowing powder, where the flow behaviour is not sensitive to the pre-shear confining stress. The pre-shear points stay consistently lower than the corresponding yield loci. However, the difference between the pre-shear points and yield loci increases with the pre-shear normal stress. Both pre-shear and shear points show very good repeatability with maximum standard deviations around symbol size. We only manage to measure representative yield locus of Eskal150 down to 0.2 kPa pre-shear normal stress, while the data measured at lower stress levels are not reliable. Note that we have also measured the yield loci at 3, 4 and 5 kPa, but for the sake of brevity, the data are not shown here. They all follow the trend of low stress levels data.

For the cohesive Eskal300 (2.2 μm), we measured the yield loci in the normal stress range between 0.1 and 2 kPa, and the data are shown in Fig. 4.6. Unlike the free flowing Eskal150, the yield loci of Eskal300 move upwards with the increase of the pre-shear normal stress, which indicates the cohesive Eskal300 is sensitive to the pre-shear normal stress. The yield loci of Eskal300 show a concave curvature and clearly visible from the guide lines. Similar to the case of Eskal150, the yield loci of Eskal300 show very good repeatability with maximum standard deviations around symbol size.

4
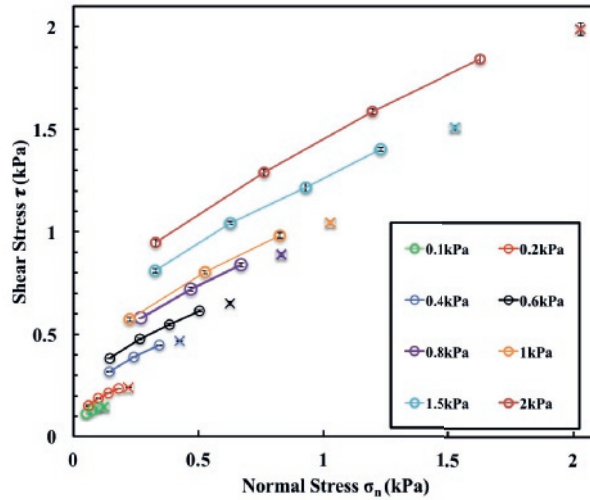
Figure 4.6: Yield locus (shear stress versus normal stress) of Eskal300 (2.2 μm) using RST-01.pc. The pre-shear normal stress is kept between 0.1 and 2 kPa. Points with and without lines are shear and pre-shear points, respectively. Lines are only guides to the eye.

4.4.3. DYNAMIC GRANUDRUM

Similar to Fig. 4.4, Fig. 4.7 shows two typical flowing patterns obtained in the rotating drum with Eskal150 (left) and Eskal300 (right). The free flowing Eskal150 shows a very smooth free surface with a slightly concave shape, while the cohesive Eskal300 gives a much rougher free surface with some clumps due to cohesion.
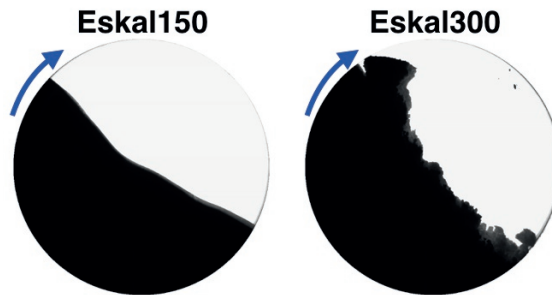
Figure 4.7: Snapshots of typical flow inside the rotating drum with Eskal150 and Eskal300.

The flowing angles of our two limestone powders at different rotating speeds are measured with the GranuDrum and plotted in Fig. 4.8. As a function of the rotating speed, the flowing angle increases for the free flowing Eskal150 and decreases for the cohesive Eskal300. This behavior is also commonly seen for other powders [10].

The increase for non-cohesive granular material is due to the inertial effect, while the
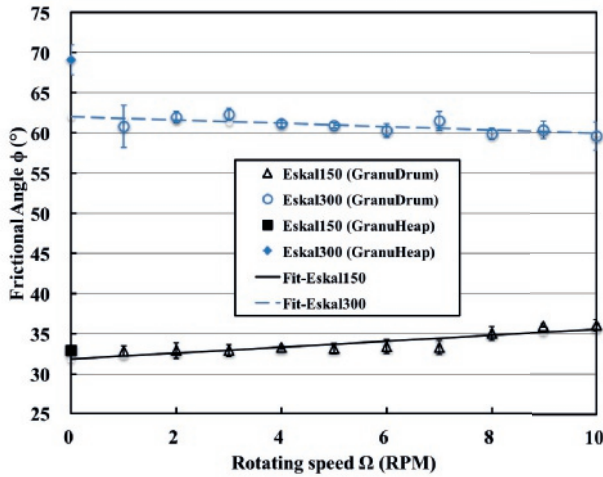
Figure 4.8: Repose angle measured with the GranuHeap (plain symbols) and the flowing angles for different rotating speeds measured with the GranuDrum (open symbols). A linear regression allows to extrapolate the angle at 0 rpm from GranuDrum data with $\phi = 0.37\Omega + 32$ for Eskal150; and $\phi = 0.2\Omega + 62$ for Eskal300.

decrease for cohesive powder is due to strong aeration at high rotating speeds. A linear regression allows us to extrapolate the angle at 0 rpm. We obtain 32° for Eskal150 and 62° for Eskal300. In addition, we also added here the two angle of reposes measured with the GranuHeap on the same figure. For the cohesive Eskal300, the repose angle measured from the heap is higher than the angle extrapolated with the drum. The difference here can be explained by the angles that measured before or after the slope instability (avalanche), which are named as upper and lower angle [30]. The static angle of repose we measured represents here are the highest stable angle Eskal300 could ever reach (upper angle) while the dynamic flowing angle stays between the upper and lower angles. This is not the case for the free flowing Eskal150, where the two measurement techniques give comparable results.

4.4.4. UNIFYING STATIC AND DYNAMIC

After confirming the repeatability of each test, we come back to the main focus of this study: linking different flow regimes. Our first step is to explore the lowest confining stress limit of the quasi-static Schulze ring shear tester at quasi-static flow regime and extrapolate the frictional angles. The second step is to evaluate the values of effective confining stress for both static GranuHeap and dynamic GranuDrum. Results can then be presented in a unique comprehensive plot showing the dependence of frictional angle ϕ on the confining stress σ for the three tests. Note that the confining stress (angle of repose test and rotating drum test) can be confused with the pre-shear normal stress (Schulze ring shear test).

In Fig. 4.9, the frictional angle measured by the Schulze ring shear tester is plotted against the confining stress (normal stress applied to the lid at the pre-shear stage) for two Eskal

powders. The confining stress axis is shown in logarithmic scale in order to represent better the range below 0.1 kPa. We have fitted data for both Eskal150 and 300 with specific functions and those have been extended towards the very low stress regime. For free flowing Eskal150, we fit our data with a linear regression towards the large confining stress. On one hand, in the low confining stress regime ($\sigma < 10$ kPa), the fitted line stays almost constant. On the other hand, if the confining stress becomes larger ($\sigma > 10$ kPa), the fitted line decreases with the confining pressure. At low confining stress, the flow behaviour of Eskal150 is dominated by the surface properties of primary particles, e.g. shape, roughness, and thus almost not influenced by the confining stress. For cohesive Eskal300, the best fit is obtained by a reducing power law, where higher frictional angle corresponds to lower confining stress. This decreasing trend with confining stress is expected as powders normally flow better at larger confining stress regime. The reason is that large confining stress leads to large plastic deformation and possible contact flattening, which reduces the influences from surface roughness and geometrical interlocking, and thus a reduction of flow resistance.
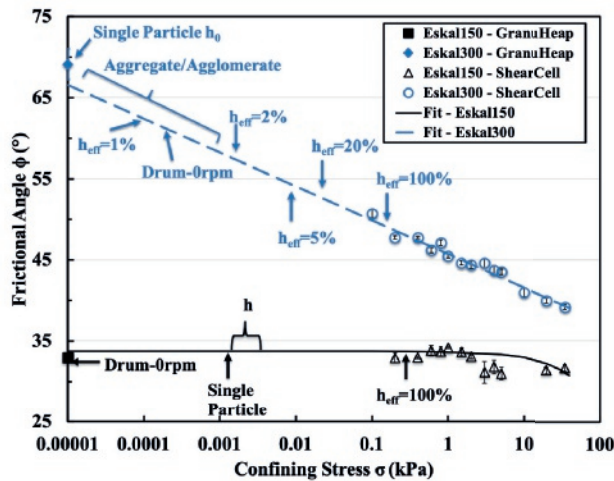
Figure 4.9: Frictional angles, ϕ, from different types of test as a function of confining stress, σ for Eskal150 (138 μm) and Eskal300 (2.2 μm) in semi-log scale. For the confining stress refers to normal stress at preshear stage in ring shear test, and estimated from weight of single particle layer and effective flowing depth of powder in GranuHeap and GranuDrum, respectively. Lines are the fitting to the shear tests data: black linear regression line with $\phi = -0.08\sigma + 33.73$ for Eskal150; blue line with $\phi = 45.72 - 4.18\log(\sigma)$ for Eskal300. Arrows with 0 rpm indicate the frictional angles extrapolated from rotating drum tests, while the other arrows indicate the estimated effective confining stresses assuming single particle layer or effective flowing depth $h_{eff} = h/r$ in the rotating drum.

In the same figure, we have also indicated the angle of repose values and the extrapolation of the flowing angle from rotating drum at 0 rpm for both Eskal150 and Eskal300. Moreover, in order to estimate the (effective) confining stress on flowing powders in both GranuHeap and GranuDrum tests, we have used two principles: single particle layer h_0 and effective flowing depth of the rotating drum h. The first one represents the effective pressure induced by a single layer of primary particles, which can be correlated to

the static angle of repose test. In the static situation, one expects the flow depth close to the free surface to be the same order of magnitude of single particle diameter. The effective flowing depth is valid only for the case of the rotating drum and given by the ratio between the actual flowing depth h and the radius r of the drum $h_{eff} = h/r$. The flow depth of non-cohesive granular materials in a rotating drum depends on the rotating speed and on the ratio between the drum diameter and the grain diameter [31]. For cohesive powders, the flowing depth increases with the cohesiveness [32]. It is almost impossible to get accurate measure of depth of the flowing layer for our cohesive Eskal300. Therefore, instead of giving an accurate estimation of the flowing depth of our cohesive Eskal300, we use a depth range: 1% to 20% of the drum radius, which covers almost all the possible depths of cohesive powder flows in a rotating drum [32]. Then, the effective confining stresses are evaluated at different depths h inside the powder considering the hydrostatic pressure $\sigma = \rho_{bulk} g h$, where ρ_{bulk} is the powder bulk density and g is gravitational acceleration. The points given by the estimated confining stress and the extrapolated frictional angles in the drum (0 rpm) are shown with arrows in Fig. 4.9.

For free flowing Eskal150, both angle of repose (black square) and flowing angle at 0 rpm (black Drum-0 rpm) match well with the prediction (black fitting line) from the Schulze ring shear tester data. This material is free flowing and insensitive to the confining stress change in the whole pressure range of our interest. The angle of repose of Eskal300 (blue diamond) is very close to the prediction of the confining stress from single particle layer and also agrees well with the frictional angle of Eskal300 as extrapolated by the fitting of shear test data. The frictional angle of GranuDrum at 0 rpm (blue Drum-0rpm) is also plausible and sit well on the dotted line. Finally, the confining stresses estimation at the bottom of the drum ($h_{eff} = 100\%$) for both Eskal150 and 300 are also given on the same figure. They both collapse with the data points obtained by shear cell measurements at low confining stress levels. The good agreement of the three types of test shows the possibility of extending the instrumental measuring limits by means of an accurate comparison of different types of test.

4.5. CONCLUSION AND OUTLOOK

In this study, we have examined the flow behaviour of both non-cohesive and cohesive limestone powders in three types of characterization tests: GranuHeap (static angle of repose), Schulze ring shear test (quasi-static frictional angle) and GranuDrum (dynamic flowing angle). Various confining stresses at low levels are performed in the Schulze ring shear tester and the results are extrapolated towards almost zero confining stress with empirical laws. This offers the possibility to extend the low limit of the confining stress and thus link to the other types of tests, specifically dynamic tests.

The static angle of free flowing Eskal150 measured with GranuHeap is much lower than the value of Eskal300, which indicates that higher cohesion leads to a higher angle of repose for the same type of material.

The dynamic flowing angle of Eskal150 measured with GranuDrum increases with the rotating speed, while decreases for the case of Eskal300. This is expected as common flow behaviour of free flowing and cohesive powders are dominated by inertial effect and

aeration, respectively. The estimation of the flowing angle of Eskal150 at 0 rpm agrees well with the measured static angle of repose. But the estimation of Eskal300 at 0 rpm is significantly larger than the static angle of repose. We attribute this to the angle variance between the static angle of repose before the slope instability and the dynamic flowing angle that comes after the avalanches.

Finally, the frictional angle obtained by quasi-static ring shear test is found to be a function of confining stress. The data of free flowing Eskal150 is fitted well with linear regression and the cohesive Eskal300 is well described by a power law. These two empirical laws allows us to gain insight at very low confining stresses that are comparable with the other two types of test. For free flowing Eskal150, all 3 tests agree well with each other. For the cohesive Eskal300, the estimations of the effective confining stresses become very difficult. An extrapolation approach is needed in order to calculate the effective confining stress in the rotating drum. Nevertheless, the results of Eskal300 from three different tests agree well with the range of confining stress estimated, confirming the validity of the approach. Our method opens new perspectives in the field of powder flow characterization for measurement interpretation and also allows to find a better link with powder behaviour in industrial process lines.

In future, a more detailed study of the effective flowing layer depth in a rotating drum for cohesive powders is needed. The strength of proposed empirical laws could be further checked by including either new materials or new testing techniques.

REFERENCES

[1] H. M. Jaeger, S. R. Nagel, and R. P. Behringer, *Granular solids, liquids, and gases,* Rev. Mod. Phys. **68**, 1259 (1996).

[2] F. Radjai, D. E. Wolf, M. Jean, and J. Moreau, *Bimodal Character of Stress Transmission in Granular Packings,* Phys. Rev. Lett. **80**, 61+ (1998).

[3] G. D. R. MiDi, *On dense granular flows,* Eur. Phys. J. E **14**, 341 (2004).

[4] P. Jop, Y. Forterre, and O. Pouliquen, *A constitutive law for dense granular flows,* Nature **441**, 727 (2006).

[5] O. Pouliquen, C. Cassar, P. Jop, Y. Forterre, and M. Nicolas, *Flow of dense granular material: towards simple constitutive laws,* J. of Stat. Mech.: Theory and Experiment **2006**, P07020 (2006).

[6] G. Lumay, N. Vandewalle, C. Bodson, L. Delattre, and O. Gerasimov, *Linking compaction dynamics to the flow properties of powders,* Appl. Phys. Lett. **89**, 093505 (2006).

[7] Y. Forterre and O. Pouliquen, *Flows of Dense Granular Media,* Annu. Rev. Fluid Mech. **40**, 1 (2008).

[8] P. Schall and M. van Hecke, *Shear bands in matter with granularity,* Annu. Rev. Fluid Mech. **42** (2010).

[9] G. Lumay and N. Vandewalle, *Flow of magnetized grains in a rotating drum,* Phys. Rev. E **82**, 040301 (2010).

[10] G. Lumay, F. Boschini, K. Traina, S. Bontempi, J. C. Remy, R. Cloots, and N. Vandewalle, *Measuring the flowing properties of powders and grains,* Powder Technol. **224**, 19 (2012).

[11] A. Jarray, V. Magnanimo, and S. Luding, *Wet granular flow control through liquid induced cohesion,* Powder Technol. (2018).

[12] A. Casagrande, *The determination of the pre-consolidation load and its practical significance,* in *Proceedings of the international conference on soil mechanics and foundation engineering,* Vol. 3 (Harvard University Cambridge, 1936) pp. 60–64.

[13] A. W. Jenike, *Storage and Flow of Solids, Bulletin No. 123,* Bulletin of the University of Utah **53**, 198 (1964).

[14] J. Schwedes, *Vergleichende betrachtungen zum einsatz von schergeräten zur messung von schüttguteigenschaften,* Proc. PARTEC, Nürnberg , 278 (1979).

[15] D. Schulze, *Entwicklung und Anwendung eines neuartigen Ringschergerätes,* Aufbereitungs-Technik **35**, 524 (1994).

[16] S. Shibuya, T. Mitachi, and S. Tamate, *Interpretation of direct shear box testing of sands as quasi-simple shear,* Geotechnique **47**, 769 (1997).

[17] J. Schwedes, *Review on testers for measuring flow properties of bulk solids,* Granul. Matter **5**, 1 (2003).

[18] D. Schulze, *Powders and bulk solids: behavior, characterization, storage and flow* (Springer, 2008).

[19] U. Zafar, C. Hare, G. Calvert, M. Ghadiri, R. Girimonte, B. Formisani, M. A. S. Quintanilla, and J. M. Valverde, *Comparison of cohesive powder flowability measured by schulze shear cell, raining bed method, sevilla powder tester and new ball indentation method,* Powder Technol. **286**, 807 (2015).

[20] H. Shi, R. Mohanty, S. Chakravarty, R. Cabiscol, M. Morgeneyer, H. Zetzener, J. Y. Ooi, A. Kwade, S. Luding, and V. Magnanimo, *Effect of particle size and cohesion on powder yielding and flow,* KONA Powder and Par. J. **35**, 226 (2018).

[21] A. Russell, P. Müller, H. Shi, and J. Tomas, *Influences of loading rate and preloading on the mechanical properties of dry elasto-plastic granules under compression,* AIChE J. **60**, 4037 (2014).

[22] S. C. Thakur, H. Ahmadian, J. Sun, and J. Y. Ooi, *An experimental and numerical study of packing, compression, and caking behaviour of detergent powders,* Particuology **12**, 2 (2014).

[23] O. I. Imole, M. Paulick, V. Magnanimo, M. Morgeneyer, B. E. Montes, M. Ramaioli, A. Kwade, and S. Luding, *Slow stress relaxation behavior of cohesive powders,* Powder technol. **293**, 82 (2016).

[24] M. Morgeneyer, L. Brendel, Z. Farkas, D. Kadau, D. E. Wolf, and J. Schwedes, *Can one make a powder forget its history?* Proc. of the 4th international conference for conveying and handling of particulate solids, Budapest , 12 (2003).

[25] M. Morgeneyer and J. Schwedes, *Investigation of powder properties using alternating strain paths,* Task Quarterly **7**, 571 (2003).

[26] H. Feise and J. Schwedes, *Investigation of the Behaviour of Cohesive Powder in the Biaxial Tester,* Kona Powder Part. J. **13**, 99 (1995).

[27] H. J. Feise, *A review of induced anisotropy and steady-state flow in powders,* Powder Technol. **98**, 191 (1998).

[28] H. Zetzener and J. Schwedes, *Relaxation and Creep of Dry Bulk Solids,* Part. Part. Syst. Charact. **19**, 144 (2002).

[29] A. D6773-16, *Standard shear test method for bulk solids using the schulze ring shear tester,* West Conshohocken, PA: ASTM International (2008).

[30] N.-S. Cheng and K. Zhao, *Difference between static and dynamic angle of repose of uniform sediment grains,* Int. J. Sediment Res. **32**, 149 (2017).

[31] G. Félix, V. Falk, and U. D'Ortona, *Granular flows in a rotating drum: the scaling law between velocity and thickness of the flow,* The Eur. Phys. J. E **22**, 25 (2007).

[32] R. Brewster, G. S. Grest, and A. J. Levine, *Effects of cohesion on the surface angle and velocity profiles of granular material in a rotating drum,* Phys. Rev. E **79, 011305** (2009), 10.1103/physreve.79.011305.

4

5

GRANULAR FLOW: FROM DILUTE TO JAMMED STATES

Particulate systems and granular matter display dynamic or static, fluid- or solid-like states, respectively – or both at the same time. The mystery of bridging the gap between the particulate, microscopic state and the macroscopic, continuum description is one of the challenges of modern research. This book chapter gives an overview of recent progress and some new insights about the collective mechanical behavior of granular, deformable particles.

5.1. INTRODUCTION

Dune migration, landslides, avalanches and silo instability are a few examples of systems where granular materials play an important role. Furthermore, handling and transport of these materials are central to many industries such as pharmaceutical, agricultural, mining and construction and pose many open questions to the researchers. In spite of their ubiquity, understanding and predicting the flow behavior of granular materials is still a major challenge for science and industry. Even in a seemingly simple system such as dry sand, the presence of large numbers of internal degrees of freedom leads to highly nonlinear effects making it difficult to relate the microscopic grain-level properties to the macroscopic bulk behavior.

Granular systems can show properties commonly associated with either solid, or liquid. They can behave like a fluid, i.e., yielding under an applied shear stress. On the other hand, they can also behave like solids, being able to resist applied stresses without deforming, showing also interesting anisotropic structure (contact-and force-networks) [2, 3]. Lucretius (ca. 98 – 55 B.C.) was among the first ones to recognize this interesting behavior of soil-like materials, when he wrote "One can scoop up poppy seeds with a

ladle as easily as if they were water and, when dipping the ladle, the seeds flow in a continuous stream" (quotation taken from Jacques [4]). Granular materials exhibit solid-like behavior if the particles are packed densely enough and a network of persistent contacts develops within the medium, resulting in a mechanically stable jammed structure of the particles. On the other hand, when the grains are widely spaced and free to move in any direction, interacting only through collisions, the medium is unjammed and behaves like a fluid [5].

Due to their microscopic, discrete nature and their interesting macroscopic, bulk behavior response, granular materials are studied using both discrete and continuum mechanics frameworks. In the realm of the discrete approach, several numerical techniques that are able to reproduce the single particle motions with the given micro-mechanical properties of the grains have been developed. In such an approach the dynamic behavior is studied by integrating the Newton's equations of motion for each grain using micro-mechanical properties and specific interaction law. Following the pioneer work by Goldhirsch [6, 7] several numerical techniques have been developed to obtain continuum fields from discrete particle data.

Using these numerical methods, one can study the flow behavior of the idealized grains, characterized by some specific micro-mechanical properties, which might not exist in the nature, but is helpful in understanding the underlying global physical behavior. In spite of their versatile applicability and benefits, these numerical methods have limitations such as excessive computational requirements, round off or truncation errors, and an intrinsic dynamic that is sometimes not reflecting the experimental reality. On the other hand, continuum models give a macroscopic view to investigate granular material behaviors. Continuum mechanics theories solve the conservation equations for the whole medium i.e., the balance of mass, momentum and when necessary, energy. Although the balance laws are easily deducible, defining the constitutive relations poses the bigger challenge. The latter relate stresses and strains taking into account the physics of the grain-grain interaction.

The goal of the present book chapter is to study the constitutive behavior of granular systems using particle, numerical simulations and micro-macro transition. In particular, we focus on the different mechanical responses of a granular material in dense and dilute conditions, corresponding to the solid and fluid behaviors, respectively. In order to systematically analyze the influence of some crucial material parameters, which affect the flow behavior, we focus on an idealized material composed of frictionless, spherical particles, in the absence of any interstitial fluids. Moreover, in order to concentrate on the rheology of particulate systems, disregarding boundary effects, we have considered two system setups which allow to simulate steady and homogeneous flows.

This chapter is organized as follows. Section 5.2 introduces the general rheological framework to describe the flow behavior of granular materials. In the same section, we also briefly review some existing granular rheological models. The particle simulations along with micro-macro transition are introduced in Section 5.3, where different system setups that are used to study the steady and homogeneous granular flows are shown. Finally, in Section 5.4, we present a comprehensive comparison of the existing simulation data with frictionless particles in dilute and dense regimes. In the same section, we highlight

the effect of various micro-mechanical properties (coefficient of restitution, polydispersity and particle stiffness) on the macroscopic fields (stresses and volume fraction). We present a comparison of these results with the theoretical models in two regimes: The kinetic theory in the dilute regime, and a recently proposed generalized rheological model in the dense regime.

5.2. GRANULAR RHEOLOGY

5.2.1. A MICRO-MECHANICAL BASED CONTINUUM APPROACH

Despite the fact that granular materials are discontinuous media, their behavior is commonly described by a continuum approach. Continuum mechanics theories solve the conservation equations of the whole medium, i.e., the balance of mass, momentum and, when necessary, energy. Although the balance laws are easily deducible, the big challenge is the definition of the constitutive relations, i.e., the rheology. The latter captures the macroscopic behavior of the system, incorporating the micro-scale grain-grain interaction dynamics.

A granular flow can undergo different behaviors depending on both properties at the particle level and the macroscopic characteristic of the flow (i.e., velocity and concentration). At the microscopic level, each particle is characterized by its shape, dimension, material and contact properties. For the sake of simplicity, in this chapter an assembly of identical spheres, of diameter d, density ρ_p and equivalent linear contact stiffness k_n is considered. The density of the continuum medium can be computed as the product of the particle density and the volume fraction, ν, defined as the fractional, local volume occupied by the spheres: $\rho = \rho_p \nu$. Given that each grain i moves with velocity $\boldsymbol{v}_i$, the macroscopic velocity of N-particles flow in a volume V can be defined as the average $\boldsymbol{u} = \frac{1}{N}\sum_{i=1}^{N} \boldsymbol{v}_i$. Similarly, we can introduce the strain rate tensor, calculated as the symmetric part of the velocity gradient. Its off-diagonal components describe the shear rate between two Cartesian directions and are often used as control parameters to describe flow problems. In particular, considering a granular system with mean flow in the x direction only and sheared along the y direction, we introduce the shear rate as $\dot{\gamma} = 2\dot{\epsilon}_{xy} = \frac{\partial u_x}{\partial y}$. Finally, in continuum mechanics, the stress tensor, σ, represents the manner in which force is internally transmitted. Each component of the stress tensor, σ_{ij}, represents the force in the i-direction on a surface with inward pointing normal unit vector in the j direction. The isotropic part of the stress tensor is the hydrostatic stress or pressure p, while the shear stress τ is proportional to the second invariant of the stress tensor. A detailed description of how to calculate strain rate and stress tensors in the case of granular assemblies will be provided in Section 5.2.2.

In the framework of continuum mechanics, dimensionless numbers are often introduced in order to describe the material behavior. These dimensionless numbers are defined as the ratio of different time scales or forces, thus signifying the relative dominance of one phenomenon over another. In the case of granular flows, the macroscopic time scale associated with the shear rate plays an important role. Then, it is convenient to scale all the quantities using the particle diameter, particle density and shear rate $\dot{\gamma}$, so that the dimensionless pressure and stiffness are given as $p/(\rho_p d^2 \dot{\gamma}^2)$ and $k_n/(\rho_p d^3 \dot{\gamma}^2)$,

respectively. On the other hand, when particle deformability becomes relevant, quantities are usually made dimensionless using the particle stiffness; pressure and shear rate are then expressed as pd/k_n and $\dot{\gamma}\sqrt{(\rho_p d^3/k_n)}$. In the following, we will see how these dimensionless numbers are used to characterize granular flows in their different regimes, namely fluid-like and solid-like.

5.2.2. Continuum models

In the early modeling attempts, granular flow is envisaged as existing in either dense solid-like, or loose gas-like regimes. Early works using shear cell experiments observed these regimes by varying the shear rate and allowing the bed to dilate or compact. Granular materials exhibit solid-like behavior if the particles are packed densely enough and a network of persistent contacts develops within the medium, resulting in a jammed mechanically stable structure of the particles. On the other hand, when the grains are widely spaced and free to move in any direction, interacting only through collisions, the medium is unjammed and behaves like a fluid [8].

In the fluid-like limit, the system is very dilute and the grains interact mainly through binary, instantaneous, uncorrelated collisions. One of the first rheological models for granular flows in this regime was proposed in 1954 by Bagnold [9]. This empirical model, derived from experiments in two-dimensional plane shear flows, basically states that the stresses are proportional to the square of the strain rate. This simple law, now known as "Bagnold scaling", has been the first to understand the physics of granular dynamics at large deformations and has been verified for dry grains in a number of experimental and numerical studies [10–13]. In the fluid-like regime, the generalization of kinetic theory of granular gases provides a meaningful hydrodynamic description.

On the other hand, when the system is very dense, its response is governed by the enduring contacts among grains, which are involved in force chains; the deformations are extremely slow because the entire network of contacts has to be continuously rearranged (jammed structure). In these conditions, the granular material behaves like a solid, showing an elastic response in which stresses are rate independent. The corresponding flow regime is usually referred to as quasi-static. Slowly deforming quasi-static dense granular materials has been mainly investigated in the framework of geomechanics. There, the majority of the constitutive models are based on the theories of elasto-plasticity and visco-plasticity [14–17], and many of them have been conceived by starting from the well-known critical state theory [18, 19].

In the transition phase, the grains interact via both force chains and collisions. None of the models cited above is able to deal with this phase-transition of granular materials – from a solid-like to a fluid-like state, and vice-versa. Intensive studies of the granular rheology at the phase transition have been conducted in the last decades, e.g. by Campbell [20], Ji and Shen [21, 22] and Chialvo et al. [23] using 3D simulations of soft frictional spheres at imposed volume fractions. In these works, the authors derived a flow-map of the various flow regimes and analyzed the transition areas. In particular, they found that, for a collection of particles, the solid-fluid transition occurs in the limit of zero confining pressure at the critical volume fraction v_c. Then the solid-like regime, in which

stresses are independent of shear rate, occurs for volume fractions $v > v_c$, whereas, at volume fractions $v < v_c$ the system shows a fluid-like behavior with stresses scaling with the square of the shear rate. In the proximity of the critical volume fraction, a continuous transition between the two extreme regimes takes place, for which the rheological behavior is still not fully understood.

More recently, new theories have been developed to model the phase transition. The French research group GDR-MiDi [24] has suggested that dense granular materials obey a local, phenomenological rheology, known as $\mu(I)$-rheology, that can be expressed in terms of relations between three non-dimensional quantities: volume fraction, shear to normal stress ratio, usually called μ, and inertial parameter I. The latter is defined as the ratio of the time scales associated with the motion perpendicular and parallel to the flow: $I = \dot{\gamma}d\sqrt{\rho_p/p}$ [25, 26]. The inertial number provides an estimate of the local rapidity of the flow, with respect to pressure, and is of significance in dynamic/inertial flows, as shown in [27]. In dense, quasi-static flows, particles interact by enduring contacts and inertial effects are negligible, that is I goes to zero. Two main assumptions on the basis of the $\mu(I)$-rheology are: (i) perfectly rigid (i.e. non-deformable) particles and (ii) homogeneous flow. Various constitutive relations, based on the GDR-MiDi rheology, have been developed [10, 28–30] in order to extend the validity of the model. In particular, the influence of particle deformability has been accounted for in the soft $\mu(I)$-rheology proposed in [31–33].

Below we present a summary of the two continuum theories that well describe the flow behavior in the limits and their extension to the intermediate regime. Kinetic theory in its standard form (SKT) provides a meaningful hydrodynamic description for frictionless particles in the very dilute regime, while $\mu(I)$ rheology holds for both frictionless and frictional particles for dense flows. It is important to mention that both theories work only for ideal systems, made of rigid, perfectly elastic, monodisperse particles. Finally, the extension of $\mu(I)$-rheology to deal with soft, deformable particles, is also introduced.

STANDARD KINETIC THEORY (SKT)

This section is largely based on the notable works of: Brilliantov et al. [34], Garzo et al. [35, 36], Goldhirsch [6, 37], Pöschel et al. [38].

The term "granular gas" is used in analogy with a (classical) molecular gas, where the molecules are widely separated and are free to move in all directions, interacting only through instantaneous, uncorrelated collisions. The main differences between molecular and granular gases are that in the latter case part of the energy is irreversibly lost whenever particles interact and the absence of strong scale separation. These facts have numerous consequences on the rheology of granular gases, one of which being the sizable normal stress differences [39].

Analogous to the molecular gases (or liquids), the macroscopic fields velocity and mass density are defined for granular systems [6]. An additional variable of the system, the granular temperature, T, is introduced as the mean square of the velocity fluctuations of the grains, in analogy with molecular gases, quantitatively describing the degree of agitation of the system. Following the statistical mechanics approach, the kinetic theory of granular gases rigorously derives the set of partial differential equations given by the

conservation laws of mass, momentum and energy (the latter describing the time development of the granular temperature) for the dilute gas of inelastically colliding particles.

In this section, we summarize the standard kinetic theory (SKT) for the case of steady and homogeneous flows for a collection of ideal particles, i.e., they are rigid, monodisperse, frictionless with diameter, d, and density, ρ_p. In this case, the mass balance is automatically satisfied, the momentum balance trivially asserts that the pressure, p, and the shear stress, τ, are homogeneous and the flow is totally governed by the balance of energy, which reduces to

$$\Gamma = \tau \dot{\gamma} \tag{5.1}$$

where Γ is the rate of energy dissipation due to collisions and $\dot{\gamma}$ is the shear rate. The constitutive relations for p, τ and Γ are given as [40]:

$$
\begin{aligned}
p &= \rho_p f_1 T \\
\tau &= \rho_p d f_2 T^{\frac{1}{2}} \dot{\gamma} \\
\Gamma &= \frac{\rho_p}{d} f_3 T^{\frac{3}{2}}
\end{aligned}
\tag{5.2}
$$

where, f_1, f_2, and, f_3, are explicit functions of the volume fraction ν and the coefficient of restitution, e_n, (ratio of pre-collisional to post-collisional relative velocity between colliding particles in the normal impact direction), and are listed in Table 5.1.

Table 5.1: List of coefficients as introduced in the constitutive relations of SKT (standard kinetic theory).

$$
\begin{aligned}
f_1 &= 4\nu G F \\
f_2 &= \frac{8J}{5\pi^{1/2}} \nu G \\
f_3 &= \frac{12}{\pi^{1/2}} (1 - e_n^2) \nu G \\
G &= \nu \frac{(2 - \nu)}{2(1 - \nu)^3} \\
F &= \frac{(1 + e_n)}{2} + \frac{1}{4G} \\
J &= \frac{(1 + e_n)}{2} + \frac{\pi}{32} \frac{[5 + 2(1 + e_n)(3e_n - 1)G][5 + 4(1 + e_n)G]}{[24 - 6(1 + e_n)^2 - 5(1 - e_n^2)]G^2}
\end{aligned}
$$

Further, by substituting the constitutive relations for τ and Γ into the energy balance, the granular temperature drops out, so that the pressure becomes proportional to the square of the strain rate (Bagnold scaling [9]):

$$p = \rho_p d^2 f_1 \dot{\gamma}^2 \tag{5.3}$$

SKT was rigorously derived under very restrictive assumptions. In particular, the granular system is assumed to be mono-disperse and composed of spherical, frictionless and rigid particles, interacting only through binary and uncorrelated collisions [8, 41, 42]. Several modifications to the SKT have been introduced in the literature accounting for different effects: inter-particle friction [5, 8, 43–45], non-sphericity [46], or polydispersity [47]. As one example, Jenkins [48, 49] extended the kinetic theory to account for the existence of correlated motion among particles at high concentration.

TRADITIONAL $\mu(I)$-RHEOLOGY

A convincing, yet simple phenomenological model that predicts the flow behavior in moderate-to-dense regime is the $\mu(I)$-rheology. Once again, this rheological law is based on the assumption of homogeneous flow of idealized rigid, mono-disperse particles, though the extra constraint of frictionless particles can be dropped. According to this empirical model, only three dimensionless variables are relevant for steady shear flows of granular materials: the volume fraction , the shear stress to normal stress ratio $\mu = \tau / p$ and the inertial number I [10, 24, 29]. The collaborative study GDR-Midi showed the data collapse for various shear geometries such as inclined plane, rotating drum and annular shear when analyzed in terms of the inertial number. $\mu(I)$-rheology in the standard form is given by

$$\mu = \mu_0 + \frac{(\mu_\infty - \mu_0)}{1 + I_0 / I} \tag{5.4}$$

with μ_0, μ, and I_0 being dimensionless, material parameters which are affected by the micro-mechanical properties of the grains [50].

To account for the polydispersity of particles, the generalized inertial number taking into account the average diameters of the particles was introduced by [51]. Traditional $\mu(I)$-rheology had been successful in describing the flow behavior of homogeneous flows (both dense and fast). But it has failed to capture the slow, inhomogeneous flow, where a shear rate gradient is present. Researchers have made significant efforts into developing non-local models for granular flows [52].

SOFT $\mu(I)$-RHEOLOGY

When particles are not perfectly rigid, instead they have a finite stiffness (or softness), the binary collision time is nonzero and hence presents an additional timescale, which is ignored in the standard inertial number phenomenology. A dimensionless number signifying the finite softness of the particles is the dimensionless pressure $p^* = pd/k_n$, which is needed to describe the flow behavior, as proposed recently in [31–33]:

$$\mu(I, p^*) = \mu(I) \left(1 - (\frac{p^*}{p_0^*})^{1/2}\right) \tag{5.5}$$

with the dimensionless pressure p^* being the characteristic pressure at which this correction becomes considerable.

The other dimensionless number needed for the full flow characterization is the volume fraction ν. In case of rigid particles under shear, the packing will dilate and hence ν

depends only on the inertial number I. On the other hand, a packing made up of soft particles will dilate due to shear, at the same time pressure will lead the compression of the particles. Hence v depends on both I and p^* as:

$$v(I, p^*) = v_c \left(1 - (\frac{I}{I_c})\right) \left(1 + (\frac{p^*}{p_c^*})\right) \tag{5.6}$$

where I_c, and p_c^* are material dependent dimensionless quantities [50, 53] and v_c is the critical volume fraction, governing the fluid-solid transitions introduced in the previous section. Its dependence on the polydispersity of the system will be discussed in Section 5.4.

5.3. NUMERICAL SIMULATIONS

Since a few decades, dynamic particle simulations have been a strong tool to tackle many challenging issues related to understanding the flow behavior of particulate systems. The Molecular Dynamics or Discrete Element Methods (DEM) is the term given to the numerical procedure, which is used to simulate assemblies of discrete particles. Molecular Dynamics (MD) was originally introduced to simulate the motion of molecules [54–56]. It is essentially the simultaneous numerical solution of Newton's equation for the motion of individual particles, for which the position, velocity and acceleration are computed at each time step. Through averaging of positions, velocities and forces of the particles, the macroscopic fields of the whole system, such as the density, mean velocity and stresses can be obtained in terms of the micro-mechanical properties. This helps in revealing insights of the behavior of granular materials, which cannot be captured by experiments. In particular, with MD methods, the role of micro-mechanical properties of the grains on the macroscopic collective behavior of the system can be analyzed. Particle simulation methods include three different techniques: The Discrete Element Method (DEM), the Event-Driven (ED), and the Contact Dynamics method (CD). All these methods simulate the inelastic and frictional nature of the contacts among grains through microscopic coefficients (i.e., the coefficients of restitution and the inter-particle friction coefficient). In DEM, deformations of particles during contacts are modeled allowing a finite overlap between grains, whereas in the other two methods, the particles are assumed to be infinitely rigid. Since the results presented in this chapter are obtained by using DEM simulations, below we briefly present an overview of DEM. Readers interested in the latter two methods are referred to [57–59].

5.3.1. DISCRETE ELEMENT METHOD (DEM)

The Discrete Element Method (DEM) is a family of numerical methods for simulating the motion of large numbers of particles. In DEM, the material is modeled as consisting of finite number of discrete particles, with given micro-mechanical properties. The interactions between particles are treated as dynamic processes with states of equilibrium developing when the internal forces balance. As previously stated, the granular material is considered as a collection of discrete particles interacting through contact forces. Since the realistic modeling of the deformations of the particles is extremely complicated, the grains are assumed to be non-deformable spheres which are allowed to over-

lap [59]. The general DEM approach involves three stages: (i) detecting the contacts between elements; (ii) calculating the interaction forces among grains; (iii) computing the acceleration of each particle by numerically integrating the Newton's equations of motion while combining all interaction forces. This three-stage process is repeated until the entire simulation is complete. Based on the fundamental simulation flow, a large variety of modified codes exist and often differ only in terms of the contact model and some techniques used in the interaction force calculations or the contact detection.

In this Subsection, we focus on the standard linear spring-dashpot (LSD) model. Considering two particles, i and j, of diameter d and density ρ_p (i.e. mass $m = \rho_p \pi d^3/6$), their contact leads to the normal (in the direction connecting the centers of the two particles in contact) and tangential components of forces as

$$
\begin{aligned}
F_{ij}^n &= -k_n \delta_{ij}^n - \eta_n \dot{\delta}_{ij}^n \\
F_{ij}^t &= -k_t \delta_{ij}^t - \eta_t \dot{\delta}_{ij}^t
\end{aligned}
\tag{5.7}
$$

where δ_{ij}^n and δ_{ij}^t are the normal and tangential component of the overlap at the contact among particle i and particle j, k_n and k_t the spring stiffness constants, and η_n and η_t the viscous damping coefficients, representing the energy dissipation at the contact, and dots stand for the time derivative. Tangential force is bounded by the Coulomb criterion $|F_{ij}^t| < \mu_p F_{ij}^n$ with particle friction coefficient μ_p. The resulting contact force vector is then $\boldsymbol{F}_{ij} = F_{ij}^n \boldsymbol{n} + F_{ij}^t \boldsymbol{t}$, being $\boldsymbol{n}$ and $\boldsymbol{t}$ the normal and tangential unit vectors at the contact.

Collisions may be described using the coefficients of normal and tangential restitution, e_n and e_t, respectively, relating the pre-collisional and post-collisional relative velocities. For the spring-dashpot model, the following relations between the coefficients of restitution, the spring constants and the damping coefficients hold [60]:

$$
\begin{aligned}
\gamma_n &= \sqrt{\frac{4 m k_n (\log e_n)^2}{\pi^2 + (\log e_n)^2}} \\
\gamma_t &= \sqrt{\frac{8 m k_t (\log e_t)^2}{7[\pi^2 + (\log e_t)^2]}} \\
k_t &= \frac{2 k_n [\pi^2 + (\log e_t)^2]}{7[\pi^2 + (\log e_n)^2]}
\end{aligned}
\tag{5.8}
$$

5.3.2. MICRO-MACRO TRANSITION

A research goal in the granular community is to derive macroscopic continuum models based on relevant micro-mechanical properties. This means to bridge the gap between the microscopic properties and the macroscopic mechanical behavior. The methods and tools for this so called micro-macro transition are often applied to small so-called representative volume elements (RVEs), where all particles can be assumed to behave

similarly. Note that both time- and space- averaging are required to obtain reasonable statistics, the latter being appropriate in the case of steady states.

As previously introduced in Section 5.2.1, the average velocity of the N particles in the RVE V gives the macroscopic velocity $\boldsymbol{u}$, while the strain rate tensor involves the velocity gradient of the particles:

$$\dot{\varepsilon} = \frac{1}{2} \sum_{i=1}^{N} \left(\nabla \boldsymbol{v}_i + \nabla^T \boldsymbol{v}_i \right) \tag{5.9}$$

being $\boldsymbol{v}_i$ the velocity of particle i. For the particular case of granular systems with mean flow in the x direction only and subjected to shear in the y direction, the shear rate is introduced as $\dot{\gamma} = 2\dot{\varepsilon}_{xy}$.

The stress tensor is of particular interest for the description of any continuum medium. In the case of granular assemblies, previous studies have proposed stress-force relationships for idealized granular systems that relate average stress in the assembly to fundamental parameters that are explicitly related to statistical averages of inter-particle load transmission and geometrical arrangement. When referring to a homogeneous volume element V, the macroscopic stress tensor $\boldsymbol{\sigma}$ can be calculated as

$$\boldsymbol{\sigma} = \frac{1}{V} \left(\sum_{i=1}^{N} m_i \boldsymbol{V}_i \otimes \boldsymbol{V}_i + \sum_{i=1}^{N} \sum_{i \neq j} \boldsymbol{F}_{ij} \otimes \boldsymbol{l}_{ij} \right) \tag{5.10}$$

where $\boldsymbol{F}_{ij}$ is the contact force and $\boldsymbol{l}_{ij}$ the branch vector in between connecting the centers of particles i and j, and $\boldsymbol{V}_i = \boldsymbol{v}_i - \boldsymbol{u}$ is the velocity fluctuation of particle i. The first and second terms in the previous equation represent the dynamic and static contributions respectively [7, 61]. The pressure and shear stress are finally defined as

$$p = \frac{\sigma_1 + \sigma_2 + \sigma_3}{3}$$
$$\tau = \sqrt{\frac{(\sigma_1 - \sigma_2)^2 + (\sigma_1 - \sigma_3)^2 + (\sigma_2 - \sigma_3)^2}{2}} \tag{5.11}$$

where $\sigma_1, \sigma_2, \sigma_3$ are the eigenvalues of the stress tensor in Eq. (5.10). With the development of computational power, nowadays one can simulate reasonable number of particles in a granular system and retrieve good statistical information by micro-macro procedure. The simulations and coarse-graining presented in this section were undertaken using the open-source code Mercury-DPM (www.mercurydpm.org).

5.3.3. SIMULATION SETUPS

There are two popular ways to extract continuum quantities relevant for flow description such as stress, density, shear rate from the discrete particle data. The traditional one is ensemble averaging of "microscopic" simulations of homogeneous small samples, a set of independent RVEs. A recently developed alternative is to simulate a non-homogeneous geometry where dynamic, flowing zones and static, high-density zones

coexist. By using adequate local averaging over equivalent volume (inside which all particles can be assumed to behave similarly), continuum descriptions in a certain parameter range can be obtained from a single simulation.
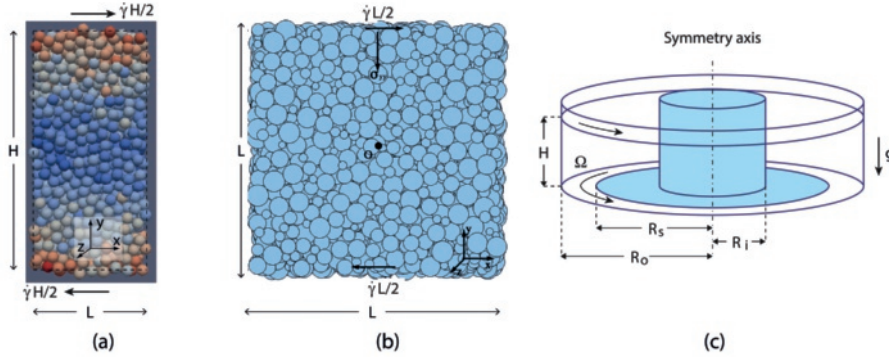
Figure 5.1: Simulation setups: (a) RVE of mono-disperse spheres subjected to constant volume simple shear. Different colors represent different kinetic energies of each particle with low in blue and high in red; (b) RVE of poly-dispersed particles subjected to constant normal stress simple shear; (c) split-bottom shear cell consisting of a fixed inner part (light blue shade) and a rotating outer part (white).

In Section 5.4, we will combine results from, (a) simple shear RVE and (b) split bottom shear cell. The setups are briefly introduced below and shown in Figure 5.1 (see Ref. [31, 50] for more details) and relevant numerical parameters are reported in Table 5.2. When dimensionless quantities (see Section 5.2.1) are matched and averaging zones are properly selected, the behaviors from different setups are comparable and a wide flow range can be explored.

Table 5.2: Numerical parameters for the three simulation setups.

Parameter Setup	Symbol	Constant Volume Simple Shear	Constant Pressure Simple Shear	Split Bottom Shear Cell
Geometry		$LxHxL$, $LxHxL$, $H = 20d$, $L = vary$,	$LxLxL$, $L = var$,	$R_s = 40d$, $R_i = 0.2R_s$, $R_o = 1.3R_s$, $H = 0.4R_s$,
Boundary Conditions		periodic	periodic	azimuthal periodic
Particle Number	N	2000	4096	37000
Polydispersity	w	1	2 and 3	2
Restitution Coeff.	e_n	0.7	0.8	0.8
Volume Fraction	ν	0.2-0.68	[-]	[-]
Dimensionless Stress	$\sigma_{yy}d/k_n$	[-]	$10^{-3} - 10^{-1}$	$10^{-8} - 10^{-2}$
Dimensionless Shear Rate	$\dot{\gamma}(\rho_p d^3/k_n)^{0.5}$	$3x10^{-4} - 3x10^{-2}$	$10^{-5} - 1$	$10^{-5} - 10^{-2}$

SIMPLE SHEAR RVE

A collection of spheres of mean diameter d and density ρ_p, sheared under steady conditions, is considered. Here and in the following, x and y are taken to be the flow and the shearing directions, respectively, and variations along the transversal direction z are ignored. We also introduce the polydispersity w as the ratio between the maximum and the minimum particle diameter. In this simple configuration, the flow is assumed to be one-dimensional such that the horizontal velocity u_x is the only non-zero component, and the stress tensor reduces to two scalars; the pressure p and the shear stress τ. In the steady state, the mass balance equation is automatically satisfied and the divergence of the velocity is zero. The momentum balance equation, in absence of external forces, indicate that both pressure p and shear stress τ are constant. Simple shear flows are homogeneous if the horizontal velocity of the medium varies linearly along the gradient direction and the dominant kinematic variable is its first spatial derivative, the shear rate, $\dot{\gamma} = \partial u_x / \partial y$, which is kept constant along the flow depth. The shear is applied using Lees-Edwards periodic boundary conditions in the y direction and periodic boundary conditions are employed in the x and z directions.

Variables governing the problem are the volume fraction ν (also known as density concentration defined as the fraction of volume occupied by the spheres), the pressure p and the shear stress τ. Using DEM simulations, we have performed simulations by using two types of simple shear experiments, that is (i) constant pressure (here refers to normal stress) or, (ii) constant volume boundary conditions. In the former (Figure 5.1b), pressure and strain rate are held constant, hence density and shear stress are outputs and the system is free to dilate/compact based on the initial volume fraction of the packing. In case of constant volume (Figure 5.1a), volume fraction and shear strain rate are held constant, so that pressure and shear stress are the outputs. Constant pressure is one of the traditional methods used in the soil mechanics to estimate the shear strength of the material, while constant volume method is used often to understand the flow behavior close to the jamming transition. Shearing under constant-volume conditions is difficult to realize experimentally due to the fundamental characteristic of the behavior of granular materials, however, a pertinent experiment would be the undrained shear test on water-saturated sand where the volume of the whole specimen can be kept constant within the range of experimental error [19]. On the other hand, dense granular flows under constant stress are present under experimental or natural conditions, e.g., sand or/and powders sheared in different shear cells [62] or in an avalanche [63].

Constant-volume steady simple shear samples are placed in a cuboid box (Figure 5.1a). The height of the computational domain as $H = 20d$, with d particle diameter, is fixed before we compute the x- and z-size L according to the chosen, fixed, volume fraction. Simulations have been performed using a monodisperse system ($w = 1$) by systematically changing both the volume fraction ν, ranging from dilute-to-dense regime and the particle stiffness k_n such that the dimensionless shear rate $\dot{\gamma}(\rho_p d^3 / k_n)^{0.5}$ ranges from $3\text{x}10^{-4}$ to $3\text{x}10^{-2}$.

In the case of RVE under constant normal stress condition (Figure 5.1b), granular systems with polydispersity $w = 2$ and $w = 3$ are considered. The initial length of side is set to L, along with the center point in x-y-plane (marked as O), where one always

has zero mean field velocity in shear direction during the whole simulation. The normal stress σ_{yy} is kept constant along y direction. In this way, the sample is free to dilate/compact along y direction and smoothly reaches its steady state. In order to investigate the sheared granular flow behavior with different inertia and particle stiffness, we systematically vary the both the confined normal stress σ_{yy} and shear strain-rate $\dot{\gamma}$ such that the dimensionless stress/softness $\sigma_{yy}d/k_n$ ranges between 10^{-3} and 10^{-1} and the dimensionless shear strain-rate is between 10^{-5} and 1.

A common feature of natural slow granular flows is the localization of strain in shear bands, which are typically of few particle diameters width. A specialized geometry proposed recently which allows one to impose an external deformation at constant rate is the so-called split-bottom geometry (Figure 5.1c). In this geometry, stable shear bands of arbitrary width can be achieved allowing for a detailed study of microstructure associated with flow of granular materials in the steady state. Unlike the previous setups, in the split-bottom geometry, the granular material is not sheared directly from the walls, but from the bottom. The bottom of the setup that supports the weight of material above it is split in two parts, the two parts move relative to each other and creates a wide shear band away from sidewalls. The resulting shear band is robust, as its location exhibits simple, mostly grain independent properties.

In this geometry, due to inhomogeneous flow, granular packings with contrasting properties and behavior co-exist, i.e., high density static to quasi-static areas and dilated dynamic flowing zones are found in the same system. A superimposed grid meshes the granular bed and averaging is performed within each grid volume. Inside a grid volume all particles are assumed to behave similarly and information for a wide parameter range can be obtained using a single numerical experiment, for example at increasing pressure levels along the depth of the cell. In the following sections, when presenting data from split bottom cell simulations, only grid-points in the center of the shear band will be considered, where the shear rate $\dot{\gamma}$ is higher than a given threshold (see references [31–33, 64] for details on the data processing). Data in center of the shear band are not affected by boundary effects, so that flow gradients can be neglected and the system can be considered as locally homogeneous. In the split-bottom geometry, the shear rate is computed as function of the relative angular velocity Ω between inner and outer cylinders. Details on the geometry setup and numerical parameters adopted for the simulations described in the following section are reported in Table 5.2.

5.4. RHEOLOGICAL FLOW BEHAVIOR

In this section, we compare the results from various flow setups discussed above for low-to-high volume fractions. We vary various particle and contact properties to understand how the particle micro-mechanical properties influence the macroscopic flow behavior. We have compared different datasets from different setups and/or authors, and numbered as following: [A] Peyneau et al. (Ref. [65]); [B] Chialvo and Sundaresan (Ref. [66]); [C] Shi et al. (unpublished); [D] Singh et al. (Ref. [31, 64]) and [E] Vescovi and Luding (Ref. [50]).Unless specified, we will only use the data labels in the following discussion

for the sake of brevity.

5.4.1. INFLUENCE OF COEFFICIENT OF RESTITUTION

Figure 5.2 presents a data collection from two different setups and plots the dimensionless pressure against volume fraction. It shows data with constant pressure simulations from data [A] together with the constant volume simulation results of data [B], for frictionless monodisperse rigid particles. As expected, the data from the two setups are in good agreement. We observe that the restitution coefficient e_n affects the dimensionless pressure strongly for volume fractions $v < 0.6$, which increases with increase in e_n. However, in the high volume fraction limit, the data for different e_n collapse on the limit curve diverging at v_c, i.e., v ranging between 0.6 and the critical volume fraction v_c.

Figure 5.2: Steady state dimensionless pressure as a function of volume fraction for a simple shear flow of frictionless monodisperse rigid particles. Stars and circles represent simple shear simulations at constant pressure simulations for $e_n = 0$ from data [A] and constant volume fraction for different e_n from data [B], respectively. Different colors refer to different coefficient of restitution as shown in the legend. Different lines are prediction using standard kinetic theory (SKT) as in Eq. (5.1) - (5.3).

For the dilute case, a granular gas with high restitution coefficient, e.g. $e_n = 0.99$ will behave like a nearly like an ideal gas i.e., almost no energy loss during each particle-particle collision. Hence the system will reach an equilibrium with higher fluctuation velocity (proportional to the dimensionless pressure) for each particle. In the other extreme, for a restitution coefficient equal to 0, the particles loose all their energy at one collision. Such strong dissipation leads to a rather small pressure in the system. As v approaches the critical volume fraction, for rigid spheres, the mean free path available for particles decreases, making it more difficult to move the particles by imposing shear. The frequency of the collisions and thus the pressure both increase since the free path decreases, diverging in the limit case. Once one reaches the critical volume fraction limit, the system is jammed, hence shear movement of particles without further deformation is not possible. The increase of the pressure for decreasing volume fraction (below 0.1),

as the probability of collisions is reduced in the dilute case, is due to the collisional energy loss, with a higher steady state pressure. As for the standard kinetic theory prediction, it captures the behavior well below volume fractions 0.5, but fails for higher volume fractions. This is expected because the standard kinetic theory (SKT) does not take the critical volume fraction into account and thus leads to an underestimation of the pressure for high volume fractions.

5.4.2. INFLUENCE OF POLYDISPERSITY

Figure 5.3 shows the variation of the non-dimensional pressure with volume fraction for different polydispersity for constant pressure (data [A] and [C]), constant volume (data [B]) homogeneous shear flow simulations, together with the local shear band data from non-homogeneous shear flows (data [D]). We observe that for low-to-moderate volume fractions, pressure is weakly increasing with volume fraction. The data from different shear setups and different polydispersity collapse and agree with the predictions of SKT. However, for higher volume fractions ($v > 0.55$), pressure increases when approaching v_c. However, different polydispersity yields different v_c [67], so that the pressure decreases with increase in polydispersity, due to the increase in free space available for particle movement for higher polydispersity (in the cases studied here). In some cases, the small particles can move into the gaps between larger particles and form rattlers (rattlers do not contribute to the pressure as for mechanically stable contacts). Therefore, the critical volume fraction v_c increases with increase in polydispersity as shown by the vertical dashed lines, consistent with previous studies [67–69].
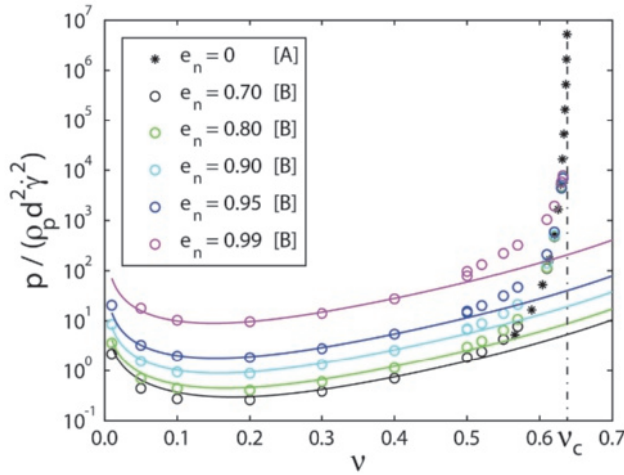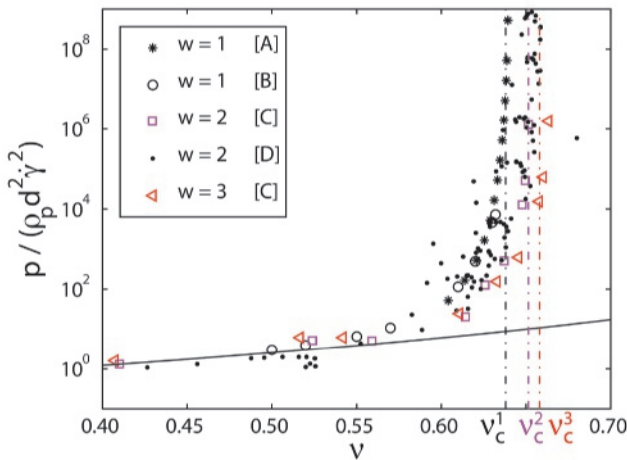

Figure 5.3: Steady state dimensionless pressure as a function of volume fraction for shear flow simulations of frictionless rigid particles with the same coefficient of restitution ($e_n = 0.8$) but different polydispersity and different setups (data [A-D]) as shown in the legend. The solid line is the prediction of standard kinetic theory and the vertical dashed lines are the predictions of the critical volume fraction with different polydispersity as proposed in Ref. [67–69].

Note that the shear band data from non-homogeneous split bottom setup (data [D]) has

more scatter than the others, due to the fluctuations of the local averaging over small volumes. But most of the data still follow exactly the same trend as the homogeneous shear data for same polydispersity. We also note that some data points, e.g., for polydispersity $w = 3$, go beyond the critical volume fraction due to the fact that DEM particles are not infinitely rigid (they have large but finite stiffness). This softness (and hence possibility of deformation) leads to flow above v_c and will be elaborated next.

5.4.3. EFFECT OF PARTICLE STIFFNESS

In Figure 5.4, we show the dimensionless pressure as a function of volume fraction for various values of dimensionless particle stiffness, ranging from 10^3 to 10^7. The vertical dashed line shows the monodispersed critical volume fraction as in Figure 5.3. For the sake of comparison, rigid cases (data [A] and [B]) are also plotted. As expected, for the rigid case, pressure diverges close to the critical volume fraction. For soft particles, the deviation from the rigid case is a function of particle stiffness and depending on the system volume fractions (even for the softest particles the deviation from the rigid limit is small for volume fractions smaller than 0.55). When decreasing the volume fraction below 0.5, all different stiffness data tend to collapse. The solid line is the same standard kinetic theory as in Figure 3 where the assumption of rigid particle breaks down for volume fractions $v > 0.5$. And the dashed line is the prediction from extended rheological model in Eq. (5.6) using the fitting parameters taken from [50] for the data with dimensionless particle stiffness 10^5. Our new extended dense rheological model smoothly captures the soft particles behavior even beyond the critical volume fraction and works perfectly between volume fraction 0.3 and 0.7.
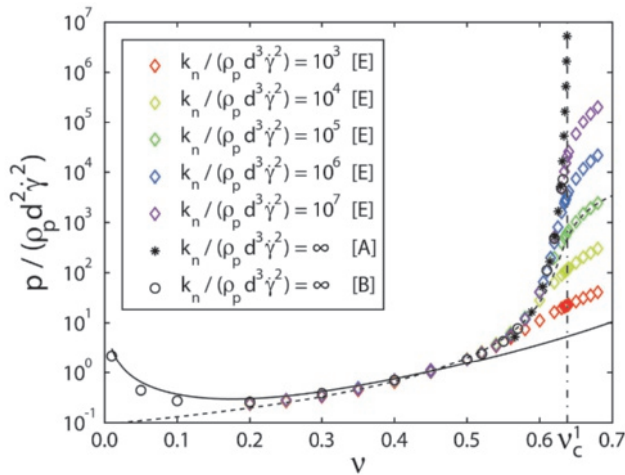
Figure 5.4: Steady state dimensionless pressure as a function of volume fraction for different values of dimensionless particle stiffness, using monodisperse particles, with restitution coefficient $e_n = 0.7$. Diamonds represent the data from constant volume simulations with data [A], [B] and [E] as suitable for monodisperse, frictionless spheres. The solid line is the prediction of standard kinetic theory and the dashed line is the critical volume fraction as also shown in Figure 5.3. The new dashed line is the prediction using Eq. (5.6) with $I_c = 3.28$, and $p_c^* = 0.33$ and $v_c = 0.636$.

5.4.4. COMBINING BOTH PARTICLE STIFFNESS AND POLYDISPERSITY IN THE DENSE REGIME

Figure 5.5 displays dimensionless pressure plotted against volume fraction for both constant volume (data [E]) and normal stress (data [C]) setups with three polydispersities and dimensionless contact stiffnesses, in the moderate to dense volume fraction regime. Diamonds represent constant volume simulation for monodisperse particles, while stars and triangles refer to the constant pressure simulation data for polydispersity 2 and 3 respectively and different color represent different particle stiffness. For $v < 0.55$, the data points from the two setups collapse and following the same trend as for the rigid case (Figure 5.3, data [A]). Interestingly, for the data above the critical volume fraction v_c, the pressure data for different polydispersity are found to collapse with a given dimensionless stiffness (both for 10^5 and 10^7). This indicates that once the system is jammed, the particle stiffness (deformation) determines the pressure without much effect of the polydispersity of particles. The solid and dashed lines are the same lines as in Figure 5.4, but is given there as a guidance to the eye representing a reference to the connections. We observe the SKT solid line is not predicting the behavior at all while the extended dense rheology dashed line is qualitatively capturing the behavior even for volume fractions $v > 0.7$, but with considerable deviations. Note that there are small differences between the data from two setups and it is due to the small differences in the particles stiffness, and this will be elaborated in the next.
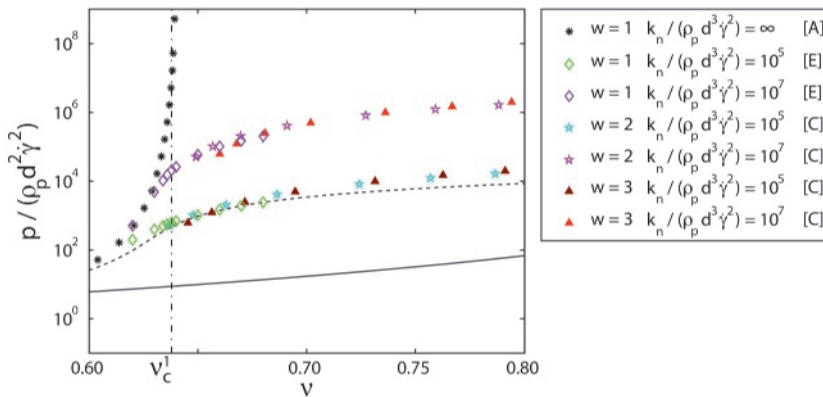
Figure 5.5: Steady state dimensionless pressure as a function of volume fraction in moderate to dense regime for simulations with different polydispersity and different particle stiffness as given in the legend. The lines are the same as in Figure 5.4.

5.4.5. FROM DILUTE TO DENSE, FROM "LIQUID" TO "SOLID", UNIVERSAL SCALING

Figure 5.6 shows the pressure non-dimensionalized in two possible ways (a) using shear rate and (b) using particle stiffness (as introduce in Section 5.2.1) plotted against the distance from the critical volume fraction for the data from different simulations using

(a)

(b)
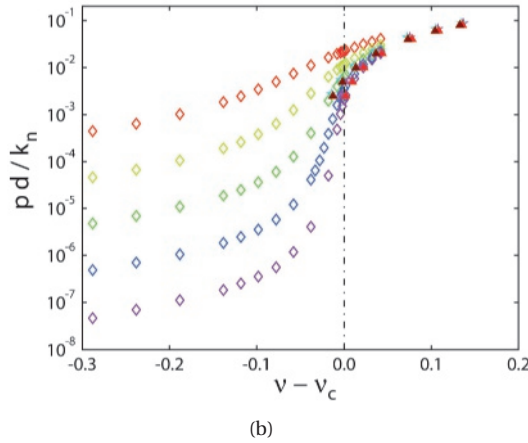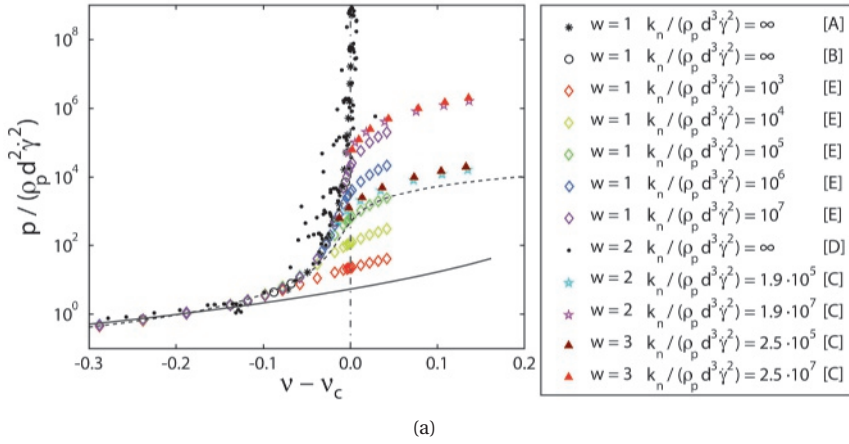
Figure 5.6: Steady state pressure, as non-dimensionalized by (a) shear rate, and (b) particle stiffness plotted as a function of distance from the critical volume fraction, $v - v_c$, for frictionless particles in different shear setups with different polydispersity and stiffness as shown in the legend. The lines are the same as in Figure 5.4.

frictionless particles. Figure. 5.6(a) shows a good data collapse for the volume fractions below the critical volume fraction (unjammed regime), or the so-called fluid regime. In the special case of nearly rigid particles or small confining stress, the scaled pressure diverges at the critical volume fraction, which indicates that the granular fluid composed of rigid particles under shear cannot reach a denser shear jammed state. For the data with softer particles, flow is possible even above the critical volume fraction. For low to moderate volume fractions, the agreement of our data with the rigid case is excellent, while for high volume fractions (especially close to the critical volume fraction) deviations are considerable. The data collapse in the low volume fraction regime shows that the Bagnold scaling relationship between pressure and volume fraction is not strongly

affected by particle stiffness, polydispersity and shear setups, but was influenced by the restitution coefficient (see Figure 5.2). The "fluid" experiences the energy loss more prominent due to collisions.

For larger volume fractions, the scaling does not collapse the data Note the deviation between constant volume (data [E]) and constant pressure (data [C]) due to the small difference in the dimensionless stiffness as shown in the legend.

Figure 5.6(b) shows the same data but only the soft particle simulations ([C] and [E]) with pressure non-dimensionalized by the particle stiffness. In this way, we observe a data collapse for high volume fractions, $v > v_c$, in agreement with the rate independent behavior as observed in other studies. This collapse of data for $v > v_c$ indicates that above the critical volume fraction the steady state rheological behavior of soft granular media under shear is dominated mostly by particle stiffness, while the influences of polydispersity and restitution coefficient ($e_n = 0.8$ in data [C] and $e_n = 0.7$ in data [E]) are of minor importance. In this regime, the higher the volume fraction, the more solid like the behavior, and hence the less influences come from other micro-parameters than stiffness. It is also important to mention that even though we presented the analysis for pressure only, the shear stress shows a similar quantitative behavior [50].

5.4.6. So much for the granular rheology

While up to now, the focus was on understanding the relation between pressure and volume fraction, a granular rheology also must consider the shear stress.
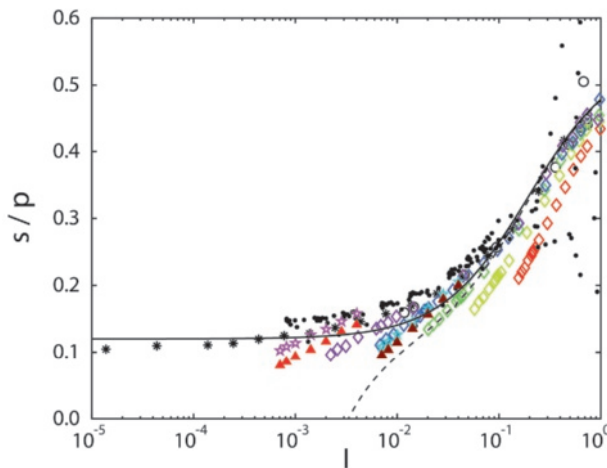
Figure 5.7: Steady state stress ratio (shear stress divided by pressure) versus inertial number, I, for data from different numerical setups as introduced in the legend of Figure 5.6, with different polydispersity, restitution coefficient, and particle stiffness. The black solid line shows the traditional $\mu(I)$-rheology from Eq. (5.4) with the fitting parameters $\mu_0 = 0.12$, $\mu = 0.55$ and $I_0 = 0.2$ for frictionless rigid particles (black symbols) [65]. The dashed line represents the prediction of the extended rheology from Eq. (5.5) using (data [E]) with $p_0^* = 0.9$ [50].

Figure 5.7 shows the steady state shear stress ratio, $\mu = \tau/p$ (scaled by pressure, mostly referred as macroscopic friction), against inertial number for all the data discussed from Figure 5.6(a) (with different polydispersity, restitution coefficient, particle stiffness, as simulated in diverse numerical setups). It is important to realize that though both shear stress and pressure diverge close to the critical volume fraction point, their ratio does not. We observe the traditional $\mu(I)$-rheology as a basic trend. For low inertial number, μ is almost independent of I, and increases with increasing I, for intermediate to large I. Interestingly, although the qualitative trend of all the data is predicted by the traditional rheology, we still observe the deviations from the prediction in Figure 5.7. There are still many unveiled folders in the granular rheology like non-local behaviors, small shear rates diffusion, particle softness influence, etc., not to mention the complexity of including the frictional and cohesive granular media or/and with liquid bridges and suspensions. And also, the missing link between the dilute and dense granular rheological models is still a great challenge in the future.

5.5. Conclusion

This chapter gives an overview of recent progress in understanding and theoretically describing the collective mechanical behavior of dissipative, deformable particles in different states, both fluid-like and solid-like. Particulate systems and granular matter display collisional, dilute and solid, mechanically stable states - either switching forth and back, or both at the same time. In which state the system resides depends on material properties like, e.g., their discrete nature (elastic stiffness), the dissipation (restitution coefficient) or the size distribution (polydispersity) of the particles. But also on the density of the system and balance between the energy input by (shear) stress or strain-rate and the energy dissipation by collisions or plastic deformations. Realistic material properties like friction and cohesion as well as non-spherical particles go beyond the scope of this chapter.

One extreme case of low and moderate density collisional flows (for weak to moderate dissipation & arbitrary polydispersity) is well described by standard kinetic theory (SKT) up to system volume fractions about 0.5, beyond which the elastic behavior of longer-lasting contacts becomes dominant. Open challenges involve very soft particles for which basic theoretical assumptions of kinetic theory fail, e.g., due to multiple contacting particles.

The other extreme case of quasi-static flow of elastic, mechanically stable solid-like structures are approximately described by the classical $\mu(I)$-rheology in the limit of rigid particles, but require a softness correction for comparatively large confining stresses. Remarkably, dissipation – as quantified by the coefficient of restitution – dominates the collisional flows in the dilute regime, while the particle stiffness, the polydispersity and the friction (data not shown here) are the controlling micro-parameters for denser quasi-static and jammed flows.

The mystery of bridging the gap between the collisional, dilute and the denser quasi-static, elastic solid-like regimes is not completely solved yet. The particulate, microscopic states are well understood by particle simulations that via a so-called micro-macro

transition can guide the development of macroscopic, continuum constitutive relations that allow to predict the state and characteristics where a granular system resides in. A unified description that ranges from dilute to dense, from rapid to slow, from soft to rigid, etc., is still one of the great challenges of today's research.

This chapter provided a few methods and some phenomenology, as well as an overview of recent literature in this field, with theories that can describe the extremes. Various recent works attempted to combine those limit-cases and provide first combined, generalized theories that go beyond the classical states. However, due to dissipation, friction, cohesion, non-sphericity of realistic materials, this poses still plenty of challenges for today's research. Our own ongoing research focuses on providing simple generalized theories, also for systems with attractive forces and with anisotropic microstructures, which were not addressed in this chapter.

REFERENCES

[1] H. Shi, D. Vescovi, A. Singh, S. Roy, V. Magnanimo, and S. Luding, *Granular flow: From dilute to jammed states,* in *Granular Materials,* edited by M. Sakellariou (In-Tech, 2017).

[2] F. Göncü and S. Luding, *Effect of particle friction and polydispersity on the macroscopic stress-strain relations of granular materials,* Acta Geotechnica (2013), 10.1007/s11440-013-0258-z.

[3] N. Kumar, S. Luding, and V. Magnanimo, *Macroscopic model with anisotropy based on micro–macro information,* Acta Mechanica **225**, 2319 (2014).

[4] J. Duran, *Sands, powders, and grains: an introduction to the physics of granular materials* (Springer Science & Business Media, 2012).

[5] J. T. Jenkins and R. W. Richman, *Grad's 13-moment system for a dense gas of inelastic spheres,* Arch. Rat. Mech. Anal. **87**, 355 (1985).

[6] I. Goldhirsch, *Rapid granular flows,* Annu. Rev. Fluid Mech. **35**, 267 (2003).

[7] I. Goldhirsch, *Stress, stress asymmetry and couple stress: from discrete particles to continuous fields,* Granul. Matter. **12**, 239 (2010).

[8] J. T. Jenkins and C. Zhang, *Kinetic Theory for Identical, Frictional, Nearly Elastic Spheres,* Physics of Fluids **14**, 1228 (2002).

[9] R. A. Bagnold, *Experiments on a gravity-free dispersion of large solid spheres in a Newtonian fluid under shear,* Proc. Royal Soc. London **225**, 49 (1954).

[10] F. Da Cruz, S. Emam, M. Prochnow, J.-N. Roux, and F. Chevoir, *Rheophysics of dense granular materials: Discrete simulation of plane shear flows,* Physical Review E **72**, 021309 (2005).

[11] G. Lois, A. Lemaître, and J. M. Carlson, *Numerical tests of constitutive laws for dense granular flows,* Physical Review E **72**, 051303 (2005).

5

[12] Pouliquen, *Scaling laws in granular flows down rough inclined planes,* Phys. Fluids **11**, 542 (1999).

[13] L. E. Silbert, G. S. Grest, T. C. Halsey, D. Levine, and S. J. Plimpton, *Granular flow down an inclined plane: Bagnold scaling and rheology,* Phys. Rev. E **64** (2001).

[14] C. di Prisco and S. Imposimato, *Experimental analysis and theoretical interpretation of triaxial load controlled loose sand specimen collapses,* Mechanics of Cohesive-frictional Materials: An International Journal on Experiments, Modelling and Computation of Materials and Structures **2**, 93 (1997).

[15] D. Kolymbas, *Constitutive modelling of granular materials* (Springer Science & Business Media, 2012).

[16] P. Perzyna, *Fundamental problems in viscoplasticity,* in *Advances in applied mechanics*, Vol. 9 (Elsevier, 1966) pp. 243–377.

[17] J.-N. Roux and G. Combe, *Quasistatic rheology and the origins of strain,* Comptes Rendus Physique **3**, 131 (2002).

[18] D. M. Wood, *Geotechnical modelling* (CRC Press, 2014).

[19] A. N. Schofield and C. P. Wroth, *Critical state soil mechanics* (McGraw-Hill, London, 1968).

[20] C. S. Campbell, *Granular shear flows at the elastic limit,* Journal of Fluid Mechanics **465**, 261 (2002).

[21] S. Ji and H. H. Shen, *Characteristics of temporalspatial parameters in quasisolid-fluid phase transition of granular materials,* Chinese Science Bulletin **51**, 646 (2006).

[22] S. Ji and H. H. Shen, *Internal parameters and regime map for soft polydispersed granular materials,* Journal of Rheology (1978-present) **52**, 87 (2008).

[23] S. Chialvo, J. Sun, and S. Sundaresan, *Bridging the rheology of granular flows in three regimes,* Phys. Rev. E **85**, 021305 (2012).

[24] G. D. R. MiDi, *On dense granular flows,* Eur. Phys. J. E **14**, 341 (2004).

[25] O. Pouliquen, C. Cassar, P. Jop, Y. Forterre, and M. Nicolas, *Flow of dense granular material: towards simple constitutive laws,* J. of Stat. Mech.: Theory and Experiment **2006** (2006).

[26] J. Gray and A. Edwards, *A depth-averaged [mu](i)-rheology for shallow granular free-surface flows,* Journal of Fluid Mechanics **755**, 503 (2014).

[27] N. Berger, E. Azéma, J. F. Douce, and F. Radjai, *Scaling behaviour of cohesive granular flows,* EPL (Europhysics Letters) **112**, 64004 (2016).

[28] R. C. Daniel, A. P. Poloski, and A. Eduardo Sáez, *A continuum constitutive model for cohesionless granular flows,* Chem. Eng. Sci. **62**, 1343 (2007).

[29] P. Jop, Y. Forterre, and O. Pouliquen, *A constitutive law for dense granular flows,* Nature **441**, 727 (2006).

[30] P. Jop, *Hydrodynamic modeling of granular flows in a modified Couette cell,* Phys. Rev. E **77**, 32301 (2008).

[31] A. Singh, V. Magnanimo, K. Saitoh, and S. Luding, *The role of gravity or pressure and contact stiffness in granular rheology,* New J. Phys. **17**, 043028 (2015).

[32] S. Roy, A. Singh, S. Luding, and T. Weinhart, *Micro-macro transition and simplified contact models for wet granular materials,* Computational particle mechanics **3**, 449 (2016).

[33] S. Roy, S. Luding, and T. Weinhart, *A general(ized) local rheology for wet granular materials,* New Journal of Physics **19**, 043014 (2017).

[34] N. V. Brilliantov and T. Pöschel, *Kinetic Theory of Granular Gases* (Oxford University Press, Oxford, UK, 2004).

[35] V. Garzó, J. W. Dufty, and C. M. Hrenya, *Enskog theory for polydisperse granular mixtures. i. navier-stokes order transport,* Physical Review E **76**, 031303 (2007).

[36] V. Garzo, C. M. Hrenya, and J. W. Dufty, *Enskog theory for polydisperse granular mixtures. II. Sonine polynomial approximation,* Phys. Rev. E **76**, 31304 (2007).

[37] I. Goldhirsch, *Introduction to granular temperature,* Powder Technol. **182**, 130 (2008).

[38] T. Pöschel and S. Luding, *Granular gases*, Vol. 564 (Springer Science & Business Media, 2001).

[39] I. Goldhirsch and N. Sela, *Origin of normal stress differences in rapid granular flows,* Phys. Rev. E **54**, 4458 (1996).

[40] V. Garzo, J. W. Dufty, V. Garzó, and J. W. Dufty, *Dense fluid transport for inelastic hard spheres,* Phys. Rev. E **59**, 5895 (1999).

[41] M. Alam, J. T. Willits, B. O. Arnarson, and S. Luding, *Kinetic theory of a binary mixture of nearly elastic disks with size and mass disparity,* Physics of Fluids **14**, 4087 (2002).

[42] D. Berzi and D. Vescovi, *Different singularities in the functions of extended kinetic theory at the origin of the yield stress in granular flows,* Physics of fluids **27**, 013302 (2015).

[43] A. Goldshtein, M. Shapiro, L. Moldavsky, and M. Fichman, *Mechanics of collisional motion of granular materials. Part 2. Wave propagation through vibrofluidized granular layers,* J. Fluid Mech. **287**, 349 (1995).

[44] C. K. K. Lun, *Kinetic theory for granular flow of dense, slightly inelastic, slightly rough spheres,* Journal of Fluid Mechanics **233**, 539 (1991).

5

[45] C. Lun and S. Savage, *A simple kinetic theory for granular flow of rough, inelastic, spherical particles,* Journal of applied mechanics **54**, 47 (1987).

[46] T. Pöschel and V. Buchholtz, *Molecular Dynamics of Arbitrarily Shaped Granular Particles,* J. Phys. I France **5**, 1431 (1995).

[47] V. Garzó and J. W. Dufty, *Hydrodynamics for a granular binary mixture at low density,* Physics of Fluids (1994-present) **14**, 1476 (2002).

[48] J. T. Jenkins, *Dense shearing flows of inelastic discs,* Physics of fluids **18**, 103307 (2006).

[49] J. Jenkins, *Dense inclined flows of inelastic spheres,* Granul. Matter. **10**, 47 (2007).

[50] D. Vescovi and S. Luding, *Merging fluid and solid granular behavior,* Soft matter **12**, 8616 (2016).

[51] P. G. Rognon, J.-N. Roux, M. Naaïm, and F. Chevoir, *Dense flows of bidisperse assemblies of disks down an inclined plane,* Physics of Fluids **19**, 058101 (2007).

[52] K. Kamrin and G. Koval, *Nonlocal Constitutive Relation for Steady Granular Flow,* Phys. Rev. Lett. **108**, 178301 (2012).

[53] S. Luding, A. Singh, S. Roy, D. Vescovi, T. Weinhart, and V. Magnanimo, *From particles in steady state shear bands via micro-macro to macroscopic rheology laws,* The 7th International Conference on Discrete Element Methods. (2016).

[54] P. A. Cundall and O. D. L. Strack, *A discrete numerical model for granular assemblies,* Géotechnique **29**, 47 (1979).

[55] R. Hartkamp, B. D. Todd, and S. Luding, *A constitutive framework for the non-Newtonian pressure tensor of a simple fluid under planar flows,* The Journal of chemical physics **138**, 244508 (2013).

[56] R. Hartkamp, A. Ghosh, T. Weinhart, and S. Luding, *A study of the anisotropy in a fluid confined in a nanochannel,* J. Chem. Phys. **137**, 44711 (2012).

[57] S. González, A. R. Thornton, and S. Luding, *An event-driven algorithm for fractal cluster formation,* Computer physics communications **182**, 1842 (2011).

[58] F. Radjai and V. Richefeu, *Contact dynamics as a nonsmooth discrete element method,* Mechanics of Materials **In Press,** (2009), 10.1016/j.mechmat.2009.01.028.

[59] S. Luding, *Introduction to discete element methods: Basics of contact force models and how to perform the micro-marco transition to continuum theory.* Euro. J. of Enviro. Civ. Eng. **12**, 785 (2008).

[60] J. Shäfer, S. Dippel, D. E. Wolf, J. Shafer, S. Dippel, and D. E. Wolf, *Force Schemes in Simulations of Granular Materials,* J. Phys. I (France) **6**, 5 (1996).

[61] T. Weinhart, A. R. Thornton, S. Luding, and O. Bokhove, *From discrete particles to continuum fields near a boundary,* Granul. Matter. **14**, 289 (2012).

[62] H. Shi, S. Luding, and V. Magnanimo, *Limestone powders yielding and steady state resistance under shearing with different testers,* in *2nd International Conference on Powder, Granule and Bulk* (2016).

[63] T. Weinhart, R. Hartkamp, A. R. Thornton, and S. Luding, *Coarse-grained local and objective continuum description of three-dimensional granular flows down an inclined surface,* Physics of Fluids **25**, 070605 (2013).

[64] A. Singh, V. Magnanimo, K. Saitoh, and S. Luding, *Effect of cohesion on shear banding in quasistatic granular materials,* Phys. Rev. E **90**, 022202+ (2014).

[65] P. E. Peyneau and J. N. Roux, *Frictionless bead packs have macroscopic friction, but no dilatancy.* Phys. Rev. E **78**, 11307 (2008).

[66] S. Chialvo and S. Sundaresan, *A modified kinetic theory for frictional granular flows in dense and dilute regimes,* Physics of Fluids **25**, 070603 (2013).

[67] V. Ogarko and S. Luding, *Equation of state and jamming density for equivalent bi- and polydisperse, smooth, hard sphere systems,* Journal of Chemical Physics **136** (2012).

[68] V. Ogarko and S. Luding, *Prediction of polydisperse hard-sphere mixture behavior using tridisperse systems,* Soft Matter **9**, 9530 (2013).

[69] N. Kumar, O. I. Imole, V. Magnanimo, and S. Luding, *Effects of polydispersity on the micro-macro behavior of granular assemblies under different deformation paths,* Particuology **12**, 64 (2014).

5

6

STEADY STATE RHEOLOGY OF HOMOGENEOUS AND INHOMOGENEOUS COHESIVE GRANULAR MATERIALS

This chapter aims at understanding the effect of different particle/contact properties like friction, softness and cohesion on the compression/dilation of sheared granular materials. We focus on the local volume fraction in steady state of various non-cohesive, dry cohesive and wet moderately-to-strongly cohesive frictionless-to-frictional soft granular materials. The results from (i) an inhomogeneous, slowly sheared split-bottom ring shear cell and (ii) a homogeneous, stress-controlled simple shear box with periodic boundaries are compared. The steady state volume fractions agree between the two geometries for a wide range of particle properties. While increasing inter-particle friction systematically leads to decreasing volume fractions, the inter-particle cohesion causes two opposing effects. With increasing strength of cohesion for both soft and stiff particles, we report an enhancement of the effect of contact friction by cohesion. For soft granular materials, strong cohesion causes an increase in volume fraction due to significant attractive forces, not visible for stiff particles. This behaviour is condensed into a particle friction – Bond number phase diagram, which can be used to predict non-monotonic sample relative dilation/compression due to the opposing effects.

6.1. INTRODUCTION

Granular materials are omnipresent in our daily life and widely used in various industries such as food, pharmaceutical, agriculture and mining. Interesting granular phenomena

like yielding and flowing [1–5], jamming [6–9], dilatancy [10–12], shear-band localiza-
tion [13–16], history-dependence [17], and anisotropy [18–21] have attracted significant
scientific interest over the past decades. When subjected to external shearing, granular
systems exhibit a non-equilibrium transition (jammed/unjammed) from a static solid-
like to a dynamic, liquid-like state [6, 7] and finally to a steady state [22]. This particu-
lar transition drew much attention for dry and wet granular systems in both dilute and
dense regimes [23–34].

Material's bulk responses like density/shear resistance are influenced strongly by dif-
ferent particle properties such as frictional forces, as well as dry or wet capillary cohe-
sion. How the microscopic particle properties influence the granular rheological flow
behaviour is still a mystery and thus attracted more attention in the last few decades
[35–44]. Although the influence from single particle property is better understood now,
there is still very little known about the combined effect of particle friction and cohesion
on the rheological behaviour of granular flows [45].

For dry cohesive granular media, one needs to account for the dominant van der Waals
force between particles when they are not in contact. This attractive force can be mod-
eled by a reversible linear long range interaction [46], if the interaction energy and dissi-
pation are matched with the true non-linear force.

In contrast, in wet granular media, particles attract each other as liquid bridges cause
capillary forces [47–49]. The capillary bridge force becomes active at first contact, but
then is active up to a certain cut-off distance where the bridge ruptures. This gives asym-
metric loading/unloading behaviour. Recent studies based on Discrete Element Method
(DEM) confirmed that the specific choice of the capillary bridge models (CBMs) has no
marked influence on the hydrodynamics of granular flow [50, 51] for small volumes of
interstitial liquids. In the present paper, our focus is thus to investigate the effect of two
qualitatively different cohesion mechanisms, dry vs. wet, on the bulk density of cohesive
granular materials. We quantify the cohesion associated with different contact models
by the dimensionless Bond number, Bo, which is defined as the ratio of time scales re-
lated to confining stress and adhesive force. In this way, we generalize the existing rheo-
logical models with cohesion dependencies.

For dry, non-cohesive but frictional granular materials, the bulk density decreases with
increasing the particle friction [39], which is shear dilatancy. Cohesive grains are more
sensitive to stress intensity as well as direction, and exhibit much larger variations in
their bulk densities [52]. Dry granular media with median particle size below 30 μm flow
less easily and show a certain bulk cohesion due to strong van der Waals interactions be-
tween particle pairs [53]. Unsaturated granular media with interstitial liquid in the form
of liquid bridges between particle pairs can also display bulk cohesion which can be
strongly influenced by the flow or redistribution of the liquid [54, 55]. Fournier et al. [56]
observed that wet systems are significantly less dense than dry granular materials even
for rather large particles. The packing density is only weakly dependent on the amount
of wetting liquid, because the forces exerted by the liquid bridges are very weakly de-
pendent on the bridge volume [47]. In general, one expects that the steady state local
volume fraction decreases with increasing either particle friction or cohesion [38, 57].
This decrease of volume fraction is related to both structural changes and increasing

bulk friction of the materials [16]. However, Roy et al. [42] reported an opposing increase of local steady state volume fraction proportional with cohesive strength. Whether the particle cohesion enhances or suppresses the frictional effects that causes dilatancy or compression remains still a debate. Therefore, the second focus of this paper is to understand the interplay between particle friction and cohesion on the steady state volume fraction of the granular systems under shear.

Dilatancy or shear dilatancy in classical plasticity and soil mechanics has a specific definition as the ratio of incremental volumetric strain to the shear strain. While the "relative dilatancy" discussed in this work is a dynamic effect that is distinct from the classical dilatancy since in the steady simple shear flow the volumetric strain is zero. Choosing different dynamic steady states based on different inter-particle cohesion, it represents the bulk density change between two different steady states.

The work is structured as follows: in section 6.2.1, we provide information on the two simulation geometries; in section 6.2.2, the two cohesive contact models are introduced; in section 6.2.3 the important dimensionless number and their related time scales are elaborated; and in section 6.2.4, the input parameters are given. Section 6.3 is devoted to the discussion of major findings of rheological modelling with a focus on the combined influences of several particle parameters, while conclusions and outlook are presented in section 6.4.

6.2. Simulation methods

Discrete Particle Method (DPM) or Discrete Element Method (DEM) is a family of numerical methods for simulating the motion of large numbers of particles. In DPM, the material is modeled as consisting of finite number of discrete particles, with given micromechanical properties. The interactions between particles are treated as dynamic processes with states of equilibrium developing when the internal forces balance. As previously stated, granular material is considered as a collection of discrete particles interacting through contact forces. Since the realistic modeling of the deformations of the particles is extremely complicated, the grains are assumed to be non-deformable spheres which are allowed to overlap [58]. The general DPM approach involves three stages: (i) detecting the contacts between elements; (ii) calculating the interaction forces among grains; (iii) computing the acceleration of each particle by numerically integrating the Newton's equations of motion while combining all interaction forces. This three-stage process is repeated until the entire simulation is complete. Based on the fundamental simulation flow, a large variety of modified codes exist and often differ only in terms of the contact model and some techniques used in the interaction force calculations or the contact detection. After the discrete simulations are finished, there are two popular ways to extract continuum relevant quantities for flow description such as stress, density from discrete particle data. The traditional one is ensemble averaging of "microscopic" simulations of homogeneous small samples, a set of independent RVEs [59–61]. A recently developed alternative is to simulate a inhomogeneous geometry where dynamic, flowing zones and static, high-density zones coexist. By using adequate local averaging over equivalent volume (inside which all particles can be assumed to behave similarly), continuum descriptions in a certain parameter range can be obtained from a single set-up

[16, 32, 37, 62].

6.2.1. GEOMETRIES

In this study, we use MercuryDPM [63–65], an open-source implementation of the Discrete Particle Method (DPM) to simulate granular flow in two geometries: homogeneous stress controlled simple shear box (RVEs) and inhomogeneous split bottom shear cell, where the local stress is given by the weight of particles above.

STRESS CONTROLLED SIMPLE SHEAR BOX (SS)
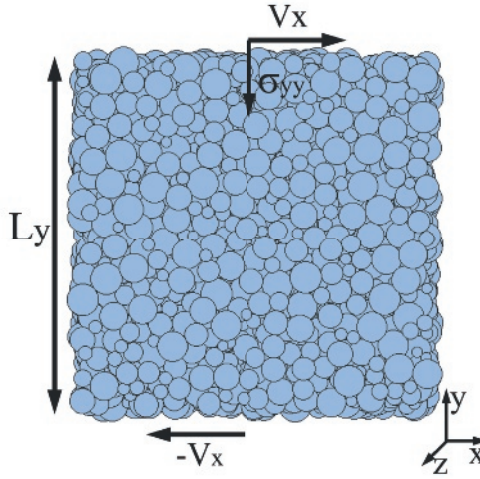
Figure 6.1: Simulation of a 3D system of polydisperse particles simple shear using Lees-Edwards periodic boundary conditions, with L_y controlled to keep the normal stress σ_{yy} constant.

The first simple geometry is a cuboid shear volume with Lees-Edwards periodic boundaries in x and y directions [66] and normal periodic boundaries in z direction as shown in Figure 6.1. The initial length of each box side is set to L, but the box side length in y-direction, L_y, can vary in time. The polydispersed granular sample contains 4096 soft particles. The system is sheared along x direction with a constant velocity V_x by moving all the particles at each time-step to achieve the homogeneous shearing. Meanwhile, the normal stress along y direction, σ_{yy} is kept constant by allowing L_y to dilate/compact, so that it smoothly reaches its steady state [67, 68]. Using this setup, one can keep both shear rate and normal stress constant while measuring the shear stress responses in both transient and steady state. Although this setup is not achievable in reality, it still represents typical lab experiments, sand or/and powders sheared in different shear cells. This setup allows the user to explore two variables (shear rate and stress) independently with low computational cost. Therefore, in the current study, we systematically vary the shear rate $\dot{\gamma} = \partial V_x/\partial y$ and confining stress σ_{yy} to understand the shear flow in both quasi-static and dynamic regimes, as well as the influence of particle softness.
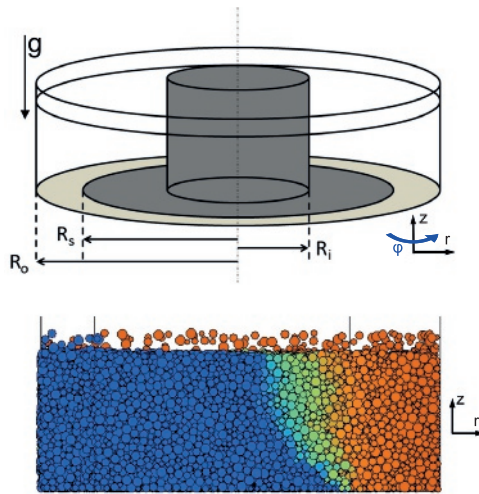
Figure 6.2: 3D Schematic representation of split bottom ring shear cell (top) and side view, showing shear band formation in the simulation (bottom) [69].

SPLIT-BOTTOM RING SHEAR CELL (SB)

In our present study, we also simulate a shear cell with annular geometry and a split bottom, as described in detail in [16, 69]. The geometry of the system consists of an outer cylinder (radius R_o = 110 mm) rotating around a fixed inner cylinder (radius R_i = 14.7 mm). We vary the rotation frequency from Ω = 0.06 to 4.71 rad/s (0.01 to 0.75 rotation/s). The granular material is confined by gravity between the two concentric cylinders, the bottom plate, and a free top surface. The gravity varies from 1 ms^{-2} to 50 ms^{-2}. The bottom plate is split at radius R_s = 85 mm. Due to the split at the bottom, a narrow shear band is formed. It moves inwards and widens towards the free surface. The filling height ($H \approx 40$ mm) is chosen such that the shear band does not reach the inner wall. Figure 6.2 shows the 3D schematic presentation and side view of the split bottom shear cell geometry with colors blue to red indicating low to high kinetic energy of the particles. It is visible that a wide shear band is formed away from the walls, which is thus free from boundary effects.

In earlier studies [16, 32], a quarter of this system ($0° \leq \phi \leq 90°$) was simulated using periodic boundary conditions. All the data corresponding to different gravities and different rotation rates belong to this system. In order to save computation time, we simulate only a smaller section of the system ($0° \leq \phi \leq 30°$) with appropriate periodic boundary conditions in the angular coordinate. No noticeable differences in the macroscopic flow behavior were observed between simulations performed using a smaller (30°) and a larger (90°) section.

6.2.2. FORCE MODELS

In our non-cohesive simulations, we use the linear visco-elastic frictional contact model between particle contacts in both geometries we mentioned above: Simple Shear Box

(SS) and Split Bottom Shear Cell (SB) [70].

The dry cohesive particles are simulated in the geometry SS using a linear reversible visco-elastic adhesive contact model as shown in Figure 6.3(a) , where we combine an at-tractive non-contact force with a linear visco-elastic frictional contact force [70]. This re-versible attractive model is chosen as a (linearized) representation of the van-der-Waals attractive non-contact force.

And in the geometry SB, we simulate wet cohesive particles using an irreversible ad-hesive non-contact force with a linear visco-elastic frictional contact force as shown in Figure 6.3(b), which only differs in the attractive non-contact part compared to the dry cohesive simulations.

Classical linear contact force

When two particles are in contact, the overlap δ can be computed as,

$$\delta = (a_i + a_j) - (\mathbf{r}_i - \mathbf{r}_j) \cdot \mathbf{n} \tag{6.1}$$

with radii a_i and a_j , for the two primary particles, respectively and the unit vector $\mathbf{n} = \mathbf{n}_{ij} = (\mathbf{r}_i - \mathbf{r}_j)/|\mathbf{r}_i - \mathbf{r}_j|$ pointing from j to i.

Thus the normal force f_n between two particles is simply computed when $\delta > 0$ (Fig. 6.3),

$$f_n = k_n \delta + \gamma_n v_n \tag{6.2}$$

with a normal stiffness k_n, a normal viscosity γ_n and the relative velocity in normal di-rection v_n [70].

On top of this simple elastic contact force law, we separately add two types of adhesive forces: reversible adhesive force and jump-in liquid bridge capillary force. The details of these two adhesive forces are elaborated in the following.
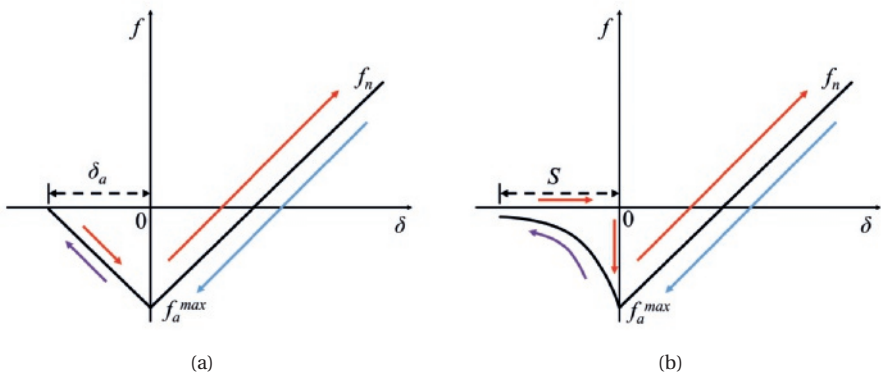

Figure 6.3: a) Reversible adhesive force with linear contact model; b) jump-in (irreversible) adhesive capillary force, combined with a linear visco-elastic contact force as in Eq. (6.2).

REVERSIBLE ADHESIVE FORCE

For the dry granular material, we assume a (linear) van-der-Waals type long-range adhesive force, f_a, as shown in Fig. 6.3(a). The adhesive force law between two primary particles i and j can be written as,

$$f_a = \begin{cases} 0 & \text{if } \delta \leq -\delta_a; \\ -k_c^a \delta - f_a^{max} & \text{if } -\delta_a \leq \delta \leq 0; \\ -f_a^{max} & \text{if } \delta > 0 \end{cases} \tag{6.3}$$

with the range of interaction $\delta_a := f_a/k_c^a$, where k_c^a is the adhesive strength of the material and f_a^{max} is the (constant) adhesive force magnitude, active for the overlap $\delta > 0$ in addition to the contact force.

When $\delta = 0$, the force is $-f_a^{max}$. The adhesive force f_a is active when particle overlap is greater than $-\delta_a$, when it starts increase/decrease linearly along k_c^a, for two particles approaching and separation respectively. In the current study, this contact model is applied in the case of homogeneous stress controlled simple shear box simulations.

JUMP-IN LIQUID BRIDGE CAPILLARY FORCE

The capillary attractive force between two particles in a wet granular bulk is modeled with a discontinuous (irreversible) attractive law as shown in Fig 6.3(b). The jump-in capillary force can be simply written as:

$$f_a = \begin{cases} 0 & \text{if } \delta < 0, \text{ approaching;} \\ \dfrac{-f_a^{max}}{(1+1.05\bar{S}+2.5\bar{S}^2)} & \text{if } -S_c \leq \delta < 0, \text{ separation;} \\ -f_a^{max} & \text{if } \delta \geq 0 \end{cases} \tag{6.4}$$

where $\bar{S} = S\sqrt{(r/V_b)}$ is the normalized the separation distance , $S = -\delta$ being the separation distance, r the reduced radius and V_b the volume of liquid bridges. The maximum capillary force at contact ($S = 0$) is given by $f_a^{max} = 2\pi r\gamma_s \cos\theta$, with the surface tension of the liquid, γ_s, and the contact angle, θ [46].

There is no attractive force before the particles come first into contact; the adhesive force becomes active and suddenly drops to a negative value, $-f_a^{max}$, when $\delta = 0$ (the liquid bridge is formed). Note that this behavior is defined here only during first approach of the particles. We assume the model to be irreversible: the forces will not follow the same path, i.e., the attractive force is active until the liquid bridge ruptures at $\delta = -S_c$. This attractive force is following Willet's capillary bridge model [47], as explained in [46]. Similar to the reversible model, we combine the attractive capillary adhesive model with the linear visco-elastic contact model defined in Sec. 6.2.2 and use this combined model to simulate wet granular materials under shear in the split bottom shear cell.

FRICTION

Introducing the additional cohesive force in the normal direction between the two particles also influences the frictional force in the tangential direction. The tangential force

6

is calculated in a similar fashion like normal force through a "spring-dashpot" model ($f_t = k_t \delta_t$) and coupled to the normal force through Coulomb's law, $f_t \leq f_s^C := \mu_s f^{rep}$, where for the sliding case one has dynamic friction with $f_t \leq f_t^C := \mu_d f^{rep}$. In this study, we use $\mu_p = \mu_s = \mu_d$. If a purely repulsive contact is established, $f^{rep} = f_n > 0$, and the tangential force is active and calculated based on the history in tangential direction. For an adhesive contact, Coulomb's law has to be modified in so far that f^{rep} is replaced by $f_n + f_a^{max}$. In the current model, the reference for a contact is no longer the zero force level, but it is the adhesive, attractive force level [58, 70].

6.2.3. TIME SCALES AND DIMENSIONLESS NUMBERS

Dimensional analysis is often used to define the characteristic time scales for different physical phenomena that the system involves. Even in a homogeneously deforming granular system, the deformation of individual grains is not homogeneous. Due to geometrical and local parametric constraints at grain scale, grains are not able to displace as affine continuum mechanics dictates they should. The flow or displacement of granular materials on the grain scale depends on the timescales for the local phenomena and interactions. Each time scale can be obtained by scaling the associated parameter with a combination of particle diameter d_p and material/particle density ρ_p. While some of the time scales are globally invariant, others are varying locally. The dynamics of the granular flow can be characterized based on different time scales depending on local and global variables. First, we define the time scale related to contact duration of particles which depends on the contact stiffness k_n as given by [32]:

$$t_k = \sqrt{\frac{\rho_p d_p^3}{k_n}} \; . \tag{6.5}$$

In the special case of a linear contact model, this is invariant and thus represents a global time scale too. Two other time scales are globally invariant, the cohesive time scale t_c, i.e., the time required for a single particle to traverse a length scale of $d_p/2$ under the action of an attractive capillary force and the gravitational time scale t_g, i.e., the elapsed time for a single particle to fall through half its diameter d_p under the influence of the gravitational force. The time scale t_c could vary locally depending on the local capillary force f_c. However, the capillary force is weakly affected by the liquid bridge volume while it strongly depends on the surface tension of the liquid γ_s. This leads to the cohesion time scale as a global parameter given by:

$$t_c = \sqrt{\frac{\rho_p d_p^4}{f_c}} \propto \sqrt{\frac{\rho_p d_p^3}{\gamma_s}} \; , \tag{6.6}$$

with surface tension γ_s and capillary force $f_c \approx \pi \gamma_s d_p$.

The global time scales for granular flow are complemented by locally varying time scales. Granular materials subjected to strain undergo constant rearrangement and thus the contact network re-arranges (by extension and compression and by rotation) with a shear rate time scale related to the local strain rate field:

$$t_{\dot\gamma} = \frac{1}{\dot\gamma} \; . \tag{6.7}$$

The time for rearrangement of the particles under a certain pressure constraint is driven by the local pressure p. This microscopic local time scale based on pressure is:

$$t_p = d_p \sqrt{\frac{\rho_p}{p}} \; . \tag{6.8}$$

As the shear cell has an unconfined top surface, where the pressure vanishes, this time scale varies locally from very low (at the base) to very high (at the surface). Likewise, the strain rate is high in the shear band and low outside, so that also this time scale varies between low and high, respectively.

Finally, one has to also look at the granular temperature time scale due to the velocity fluctuations among all the particles which is of significance of determining how "hot" the system is [33, 71, 72]:

$$t_T = \frac{d_p}{\sqrt{T_g}} \; . \tag{6.9}$$

Dimensionless numbers in fluid and granular mechanics are a set of dimensionless quantities that have a dominant role in describing the flow behavior. These dimensionless numbers are often defined as the ratio of different time scales or forces, thus signifying the relative dominance of one phenomenon over another. In general, we expect five time scales (t_g, t_p, t_c, $t_{\dot\gamma}$ and t_k) to influence the rheology of our system. Note that among the five time scales discussed here, there are ten possible dimensionless ratios of different time scales. We propose three of them that are sufficient to define the rheology that describes our results.

The first dimensionless number is Inertial Number, which is the ratio between t_p and $t_{\dot\gamma}$,

$$I = \dot\gamma d_p / \sqrt{p/\rho_p} \tag{6.10}$$

The second Softness characterizes how "soft" the system is and is the square of the ratio between contact collision timescale t_k and pressure timescale t_p,

$$p^* = p d_p / k_n \tag{6.11}$$

The last one which is important to characterize the cohesiveness in the whole system is Bond Number. It is also the square of the ratio between pressure timescale t_p and cohesion timescale t_c,

$$Bo = f_a^{max} / p d_p^2 \tag{6.12}$$

Interestingly, all these three dimensionless ratios are based on the common time scale t_p. Thus, the time scale related to confining pressure is important in every aspect of the granular flow [32, 43].

6.2.4. SIMULATION PARAMETERS

FIXED PARTICLE PARAMETERS

The fixed input parameters for the two different simulation set-ups are summarized in Table 6.1. In the liquid bridge capillary contact model, there are two extra input parameters compared to the dry adhesive model: contact angle and liquid bridge volume. These two parameters are kept constant for all the simulations. Apart from that, the only difference in the inputs is that we use restitution coefficient, $e = 0.8$ to compute the normal viscosity in the dry adhesive model but directly input the normal viscosity in the liquid bridge capillary contact model.

Table 6.1: Summary and numerical values of fixed input particle parameters used in the DPM simulations.

Parameter	Symbol	Simple Shear (dry)	Split-Bottom (wet)
Average Diameter	d_p	2.2 mm	2.2 mm
Polydispersity	$w = r_{max}/r_{min}$	2 and 3	2
Particle Density	ρ_p	2000 kg/m^3	2000 kg/m^3
Normal stiffness	k_n	100 kg/s^2	100 kg/s^2
Tangential stiffness	k_t/k_n	2/7	2/7
Rolling/torsion stiffness	k_r/k_n	2/7	2/7
Coulomb friction static	μ_s	0 to 1	0.01
Coulomb friction dynamic	μ_d	0 to 1	0.01
Rolling friction	μ_r	0	0
Torsion friction	μ_t	0	0
Restitution coefficient	e	0.8	0.8
Normal Viscosity	γ_n	0.002 kg/s	0.002 kg/s
Friction Viscosity	γ_{fr}/γ_n	2/7	2/7
Rolling Viscosity	γ_{ro}/γ_n	2/7	2/7
Torsion Viscosity	γ_{to}/γ_n	2/7	2/7
Adhesion stiffness	k_{adh}/k_n	1	[−]
Contact angle	θ	[−]	20°
Liquid bridge volume	V_b	[−]	75 nl

CONTROL PARAMETERS

Apart from the fixed particle parameters, there are also several control parameters which we vary and explore the influences of those variables, for instance, shear rate, pressure, gravity and cohesion, in which we could explore also our rheology towards different inertia, softness and cohesion regimes. The details of parameter ranges are summarized in Table 6.2.

To study the effect of inertia and contact stiffness on the dry-non-cohesive materials rheology in the geometry SS, we vary the shear rate, $\dot{\gamma}$, between 0.0001 and 1 s^{-1} , as well as the pressure, p, between 125 and 4000 Pa. Thus, we obtain inertial numbers, I, between 0.001 and 1; softness, p^*, between 0.001 and 0.1. While for the dry-cohesive simulations in the same set-up, we keep the shear rate, $\dot{\gamma} = 0.005$ s^{-1}, pressure, $p = 500$ Pa, and vary only the maximum adhesion force, f_a^{max}, between 0 and 0.01 N. This leads to the range of Bond number, Bo, between 0 and 5.

Table 6.2: Summary of variable control parameters used in two geometries: Simple Shear Box (SS) and Split Bottom Shear Cell (SB).

	SS			SB		
	$\dot{\gamma}$ [s^{-1}]	p [Pa]	f_a^{max} [N]	Ω [rad/s]	g [m s^{-2}]	γ_s [N m^{-1}]
Input range	0.0001-1	125-4000	0-0.01	0.063-4.712	1-50	0-0.3
Dimensionless numbers range	I: 0.001-1	p^*: 0.001-0.1	Bo: 0-5	I: 0.001-0.1	p^*: 0.002-0.05	Bo: 0-4

For the dry non-cohesive simulations using the geometry SB, we vary the rotation rate, f, between 0.063 to 4.712 rad/s (0.01 and 0.75 rotation/s), of the outer wall to vary the system inertia and therefore match the case of the simple shear box. And to change the pressure in this free surface system, we achieve low or high pressure by varying the gravity, g, between 1 and 50 m s^{-2}. In the case of wet granular material in SB, we vary the intensity of the maximum capillary force $f_a^{max} = 2\pi r \gamma_s \cos\theta$, by varying the surface tension of the liquid γ_s, while keeping the volume of liquid bridges V_b constant at 75 nl, corresponding to a liquid saturation of 8% of the volume of the pores and the contact angle θ is fixed at 20°. The chosen values of surface tensions are between 0 and 0.3 N m^{-1}. The rotation rate, f = 0.01 rps and the gravity, g = 9.81 m s^{-2} are kept constant for all the wet cohesive simulations.

Note that for all the simulations performed using geometry SB, the inter-particle friction is kept constant at μ_p = 0.01, while for the simulations performed in geometry SS, we vary μ_p between 0 and 1. Therefore, for the comparison between the two geometries, we choose only the data with μ_p = 0.01, and in each simulation performed, the Coulomb friction static and dynamic are always kept the same and referred to by the inter-particle friction, $\mu_p = \mu_s = \mu_d$.

6.3. RHEOLOGY

Our first goal is to check the consistency of bulk densities from two different geometries: SS and SB when using the same non-cohesive contact model. And the second goal is to investigate how different cohesive contact models influence the bulk density at steady state. Therefore, in Sec. 6.3.1, we check whether the shear behaviour of the non-cohesive granular media is the same in the two different geometries, by comparing the steady state volume fractions. And then in Sec. 6.3.2, we compare the rheological behaviours of cohesive granular materials using the reversible adhesive contact model (stress controlled simple shear box) and irreversible liquid bridge capillary contact model (split bottom shear cell). In addition, we also check the validity of existing frictional rheology and consummate it towards cohesive materials. Finally, in order to achieve our second goal, we explain the interplay between particle friction and cohesion in Sec. 6.3.3.

6.3.1. NON-COHESIVE GRANULAR MATERIALS

For dry granular materials, which have large particle size and negligible attractive forces ($Bo \approx 0$), the rheology (i.e., the equations of state for volume fraction and macroscopic friction) depends mainly on the inertial number, I, and the particle softness, p^*, which

are the competition between the time scales $t_p/t_{\dot{\gamma}}$ and t_k/t_p, respectively. The dependence of the macroscopic friction coefficient $\mu = \tau/p$ on p^* and I has been studied earlier [32, 43]. In order to complete the rheology for soft, compressible particles, a relation for the volume fraction, ϕ, as function of pressure and shear rate is still missing for dry non-cohesive materials. In previous work [62], the following dependency was reported:

$$\phi(I, p^*) = \phi_0 g_I(I) g_p(p^*) \tag{6.13}$$

with the critical or steady state volume fraction under shear, i.e., the limit for vanishing pressure and inertial number, $\phi_0(\mu_p = 0.01) = 0.64$, and $g_I(I) = (1 - I/I_\phi)$, $g_p(p^*) = (1 + p^*/p_\phi^*)$. The typical strain rate for which shear dilation would turn to extreme fluidization is $I_\phi = 0.85$, and the typical pressure level for which softness leads to huge densities is $p_\phi^* = 0.33$ [62]. Note that both correction functions are given first order with respect to their higher order Taylor expansions, i.e., they are valid only for sufficiently small arguments. In slow, quasi-static flows in the split bottom shear cell simulations, weak dilation is observed, i.e., no strong dependence of ϕ on the local shear rate [62]. On the other hand, large inertial numbers fully fluidize the system so that the rheology should be that of a granular fluid, for which kinetic theory applies. Small pressure, i.e., small overlaps have little effect, while too large pressure would lead to enormous overlaps, for which the contact model and the particle simulation with pair forces become questionable. Therefore, we focus on the quasi-static to moderate inertial regime ($I < 0.2 \approx I_\phi/4$) and low to moderate overlaps between particles ($p^* < 0.08 \approx p_\phi^*/4$) with only a few data outside this regime [62, 68].

Note that in Eq. (6.13), although the volume fraction depends on inter-particle friction, μ_p, here we do not include μ_p as functional variable. We consider inter-particle friction as a micro-parameter like polydispersity or restitution coefficient, which is different from the state variables in our functions, e.g. shear rate and pressure. However, we did explore this dependency in detail, as explained in Appendix B.

In Fig. 6.4, we plot the volume fraction in steady state as a function of inertial number for both the stress controlled simple shear box (SS) as well as the split bottom shear cell (SB) with the same friction coefficient $\mu_p = 0.01$. For the case of SS, when we we keep softness p^* constant and vary only shear rate (black squares and dashed lines), the volume fractions decrease with inertial number, the increase of inertia (shear rate) leading to higher collisional/dynamic pressure. Correspondingly in the case of SB, when we vary the rotation velocity (red triangles), the volume fraction follows the same trend and data collapse well with the data from SS but with slightly more scatter due to the local, small volumes used for averaging. The red triangles are not following any single of the dashed lines since p^* is small but not constant. When we fix shear rate and vary only pressure (blue circles and solid lines), the large pressure leads to considerable compaction at small I.

In order to focus on the dependency of softness p^*, in Fig. 6.5, we plot the same data as in Fig. 6.4 against softness. For the case of SS, when the shear rate $\dot{\gamma}$ is kept constant while softness p^* is varying (blue circles), we observe an increase of volume fraction with softness. For the corresponding case in SB, when we keep the rotation velocity constant and vary gravity (brown crosses), the volume fractions follow the same trend as in the
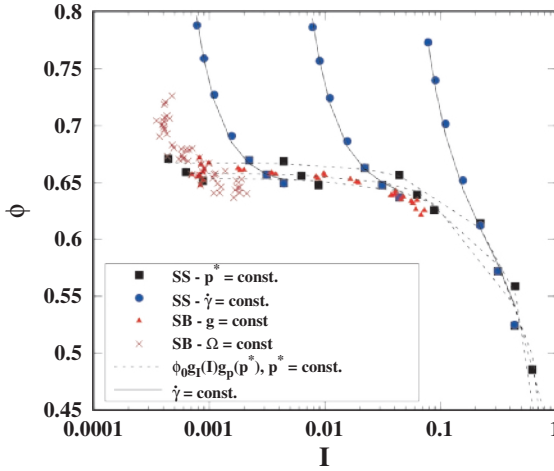
Figure 6.4: Volume fraction, ϕ, plotted against inertial number, I, using stress controlled simple shear box (SS) and split bottom shear cell (SB) with $\mu_p = 0.01$. For SS, two sets of parameters are chosen: i). fix softness at $p^* = [0.0025, 0.005, 0.01]$, vary shear rate $\dot{\gamma}$ between 0.0001 and 1 (black); ii) fix shear rate at $\dot{\gamma} = [0.0005, 0.005, 0.05]$, vary softness p^* between 0.001 and 0.1 (blue). For SB, the range of values of gravity g and rotation frequency Ω are given in Table 6.2 and the cloud of points represent center of shear band data from 12 SB simulations. The lines are the predictions Eq. (6.13), fitted using SS data, with $\phi_0 = 0.65$, $I_\phi = 2.77$ and $p^*_\phi = 0.30$. Solid and dashed lines represent constant $\dot{\gamma}$ and p^*, respectively.

case of SS and increase with softness in a linear relation as specified in [32]. Different gravity data from the split bottom shear cell collapse also well with the simple shear box data but with slightly more scatter. The increase in softness p^* can be due to the pressure increase in the system or the particles becoming softer; in either case the particles will overlap more thus leading to an increase in the volume fraction.

In the same Figs. 6.4 and 6.5, we also plot the prediction of Eq. (6.13) fitted using data from SS and with the details of fitting parameters summarized in Table 6.3. Since the two systems have similar rheological behaviour, one would expect the rheological model developed from SB should capture also the behaviour of SS and vice versa. The prediction of fitted function looks promising and it captures well both the dependencies of system inertia and softness as shown in dashed and solid lines, respectively. All the fitting deviations are within 5%, even for data with relatively high inertia ($I > 0.2$). However, when the volume fraction gets low (below 0.5), the predictions of our rheological model deviates from the simulation data, because the system goes from the dense state towards a loose granular fluid, where our model does not take this into account. Alternative rheological models for the jamming transition are reviewed in [33], while the appropriate model for the fluid/gas state is standard kinetic theory as studied in [73–76]. This indicates the limits of using the rheological model Eq. (6.13); it predicts well moderate to dense granular flows with finite contact stresses, but not dynamic, less dense granular gases. Note that here we have also included the $I_\phi = 0.85$ from [43, 62, 72], which is different from $I_\phi = 2.7699$ obtained from SS setup. This difference is caused by different granular tem-
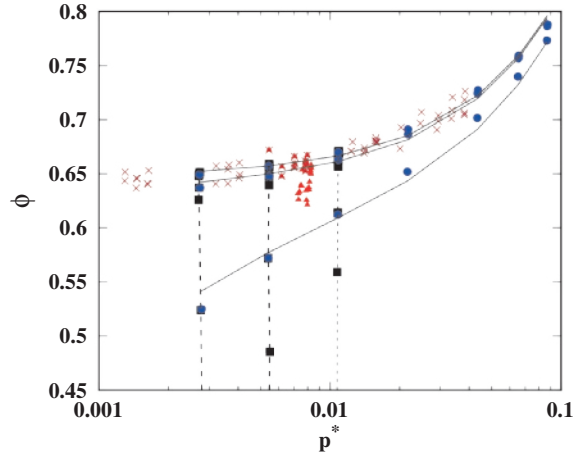
Figure 6.5: Volume fraction, ϕ, plotted against softness, p^*, for the same data as in Fig. 6.4.

peratures inside the two geometries at relatively high Inertial numbers ($I > 0.05$), which is still an ongoing research and will be addressed in a separate study.

Table 6.3: The fitting coefficients of the non-cohesive rheological model for ϕ in Eq. (6.13) for various μ_p. Note that in this study, we use particle density ρ_p in the Inertial number. While bulk density $\rho_b = \rho_p * \phi_0$ is used in different literature [43, 62, 72] and leads to the confusing I_ϕ values (details in the table below) due to this alternative definitions of Inertial number.

μ_p	ϕ_0	I_ϕ	p_ϕ^*
0.00	0.6549	2.5806	0.3044
0.01	0.6535	2.7699	0.3049
0.01 in Ref. [43, 62, 72]	0.65	0.85	0.33
0.05	0.6462	2.9652	0.3016
0.10	0.6372	3.2105	0.2975
0.20	0.6220	3.6174	0.2884
0.30	0.6111	4.1916	0.2809
0.40	0.6027	4.6543	0.2724
0.50	0.5962	5.1727	0.2640
0.70	0.5895	5.5727	0.2594
0.90	0.5845	5.9727	0.2547
1.00	0.5838	6.1727	0.2524

6.3.2. COHESIVE GRANULAR MATERIALS

For cohesive granular materials, attractive forces enhance the local compressive stresses acting on the particles, thus leading to an increase in the volume fraction. On the other hand, rough and frictional particles will display a strong dilatancy, i.e., a reduced volume fraction under shear at steady state, compared to their initial (over-consolidated) volume fraction. We systematically vary the inter-particle friction (μ_p from 0 to 1) and then for each inter-particle friction value we vary cohesion (Bo from 0 to 5) to study the volume

fraction variations in steady state. Then we introduce a generalized rheological model involving cohesion, as based on evidence from the simulations.

The Bond number represents the competition between pressure time scale t_p and cohesion time scale t_c. Low bond number refers to $t_p \ll t_c$ while high Bond number indicates $t_p \gg t_c$. The variation of Bond number in the current study provides a wide estimate of the cohesion intensity by comparing the maximum pressure allowed by the cohesion f_a^{max}/d_p^2 to the actual pressure from the particle contacts.

EFFECTS OF COHESION FOR DIFFERENT PARTICLE FRICTION

In Fig. 6.6, we plot the steady state volume fraction against the Bond number for samples with different inter-particle friction using the SS geometry. For very low inter-particle friction ($\mu_p \leq 0.01$), we observe an overall continuous increase in the volume fraction with Bo. For higher inter-particle friction ($\mu_p \geq 0.05$), dilatancy is observed with increasing Bo up to values above 1. When the Bond number becomes larger, the volume fraction increases with increasing Bo. When we fix the cohesion ($Bo \approx$ const.) and vary the particle friction, we always see the volume fraction decrease with increasing particle friction; this indicates the particle friction will always lead to shear dilation not the compression. Thus, we assume that the change in volume fraction is due to the compression of soft cohesive particles and the dilatancy due to structural changes in the presence of friction. We also added here the predictions of our proposed rheological models as in Eq. (6.16) and Eq. (6.18) with solid and dashed lines, respectively. The predictions of Eq. (6.16) are in very good agreements with the actual data, but the lines of including Eq. (6.18) over-predict the volume fractions at the steady state and deviate more towards higher Bond numbers. The details of how the rheological model is modified/generalized will be discussed in the following.

In cohesive flows, attractive forces enhance the compressive pressure acting on the particles. This can be quantified as follows: the net pressure can be split into two components, $p = p_{rep} - p_{coh}$, denoting the respective contributions of repulsive and cohesive contact forces. The ratio between the total cohesive contribution and the total pressure is given by the local Bond number, $Bo = p_{coh}/p$, and thus $p_{rep} = (1 + Bo)p$. As the geometrical compression (deformation at each contact) is related to the *repulsive* stress, it is the repulsive pressure p_{rep} that has to be considered in the softness factor g_p to correct this cohesion induced bulk density change. However, this $(1 + Bo)$ correction is not considered inside the Inertial number I, because the dominating timescale here is the pressure time scale t_p that correlated to the total pressure p_{total} in the system not the repulsive part p_{rep}. Thus, using Eq. (6.13), the modified softness correction for cohesive systems is given as:

$$g_p = g_p(p^*, Bo) = g_p(p_{rep}^*) = g_p((1 + Bo)p^*) \tag{6.14}$$

For non-cohesive systems, $Bo = 0$, g_p is consistent with the non-cohesive rheological functions. This modified pressure is similar in spirit with the modified inertial number as presented in [77], which takes into account the cohesive contribution in stress. A similar modification of pressure in the Inertial number is also required in the inertial regime
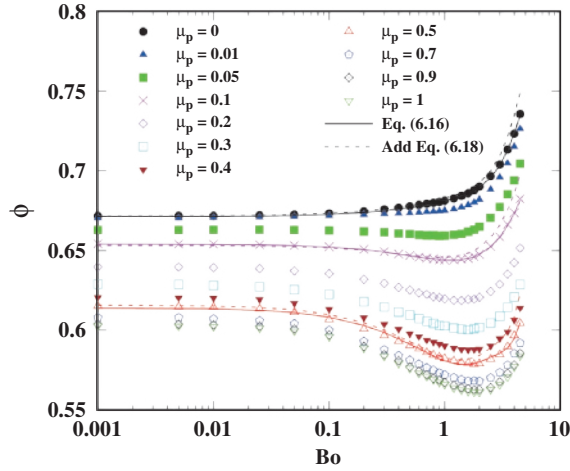
Figure 6.6: The SS volume fraction ϕ as a function of the Bond number Bo for different inter-particle friction coefficients μ_p. The shear rate $\dot{\gamma} = 0.005 \text{ s}^{-1}$ and pressure $p = 500$ Pa are kept constant for all the simulations shown here, so that $I = 0.02$ and $p^* = 0.01$. The solid lines are the predictions of Eq. (6.16) while the dashed lines are the predictions including the μ_p dependency as in Eq. (6.18).

6

but only weakly affects in the quasi-static regime. In other words, the modification of using p^*_{rep} will only make the unmodified situation going towards lower inertia regime, in which no obvious trend of volume fraction ϕ is observed.

In Fig. 6.7, we plot the same data as in Fig. 6.6 to obtain the functional format of the correction g_c: the normalized volume fraction, $g_c = \phi / [\phi_0 g_I(I) g_p(p^*, Bo)]$ as function of the Bond number, Bo, in order to confirm the effect of cohesion on the dilatancy of soft particles. From low to moderate Bo, the correction g_c decreases with increase of Bo. The increase of the repulsive force between two contacting particles leads also to an increase of the limit to sliding and thus increase the non-mobilized tangential force, resulting in an enhancement of the role of friction. For $Bo \geqslant 3$, the g_c increases from its minimum at $Bo \approx 3$. For even larger Bond number (data not shown), the attractive force is so high that sample dilation is suppressed by compression. Note that compression is prevailing for soft particles but is negligible when $p^* \approx 0$, in the limits of low confining stress or infinite stiffness, when the local volume fraction is expected to monotonically decrease with Bo. Some previous studies have confirmed the negligible effect of confining stress p^* when using stiff particles [77, 78].

Here we assume that the frictional contributions are same for both cohesive and non-cohesive materials. Therefore, we use the coefficients of the non-cohesive material: ϕ_0, I_ϕ and p^*_ϕ from Table 6.3. The local volume fraction ϕ is scaled/divided by g_I as in Eq. (6.13) and g_p as modified in Eq. (6.14). In such a way, we hope to remove the effect of particle inertia as well as particle softness.

Thus, cohesion contributes to the initial decrease and subsequent increase in the volume fraction correction of g_c for sheared materials, and depends on the inter-particle

friction. In order to quantify this dependence, the correction function g_c of the Bond number, Bo, is given by a fourth degree polynomial function:

$$g_c(Bo) = p_4 Bo^4 + p_3 Bo^3 + p_2 Bo^2 + p_1 Bo + p_0 \qquad (6.15)$$

where, p_4, p_3, p_2 and p_1 are constants depending on μ_p and $p_0 = 1$. The actual fitted values for g_c with different inter-particle friction, μ_p, are summarized in Table 6.4. With increasing μ_p, the polynomial constants p_1, p_3 decrease, but p_2, p_4 increase.

Table 6.4: The fitting coefficients of 4th degree polynomial.

μ_p	p_4	p_3	p_2	p_1	p_0
0.00	-0.000476	0.00489	-0.01260	-0.00634	1
0.01	-0.000444	0.00430	-0.00855	-0.01691	1
0.05	0.000011	-0.00046	0.00874	-0.04262	1
0.10	0.000212	-0.00288	0.01881	-0.06059	1
0.20	0.000640	-0.00743	0.03593	-0.08948	1
0.30	0.001113	-0.01229	0.05300	-0.11510	1
0.40	0.001433	-0.01543	0.06374	-0.13178	1
0.50	0.001615	-0.01733	0.07046	-0.14242	1
0.70	0.001866	-0.01988	0.07944	-0.15629	1
0.90	0.001565	-0.01728	0.07274	-0.15257	1
1.00	0.001626	-0.01771	0.07366	-0.15412	1

6

The lines in Fig. 6.7 represent Eq. (6.15), where a promising collapse between this prediction and the simulation data is observed. For low particle friction, e.g. $\mu_p = 0.01$, the volume fraction decreases gradually with Bo; while for higher particle friction, e.g. $\mu_p = 0.5$, the volume fraction decreases more sharply with Bo. We note that for frictionless particles ($\mu_p = 0$) under shear, the correction g_c decreases with increasing Bo, which suggests that cohesion contributes to the structural changes that relate to shear dilation. In other words, on top of the effect in g_p, cohesion could make frictionless particles stick together and form clusters, that result in an increase of the bulk shear resistance (data not shown here). The sample has to dilate to reduce its shear resistance to compensate this effect. Thus the role of contact friction in enhancing dilation is not a solitary effect, also cohesion is affecting the system behaviour: one should not neglect the role of either. Frictional particles need at least four mechanical contacts to form a stable structure while frictionless particles need six contacts. The higher the friction, the higher the probability that a stable packing can be formed in lower volume fractions with less average contacts/coordination number. In Fig. 6.6, we observe the steady state volume fraction decreases with increase of the inter-particle friction at fixed cohesion/Bond number, which indicates that the sample with higher inter-particle friction can reach steady state or form stable structure resisting the shear with a much lower volume fraction.

Comparing to the previous works [32, 43], a more complete rheology including the cohesion/Bond number influences on the volume fraction is introduced:

$$\phi(I, p^*, Bo) = \phi_0 g_I(I) g_p((1 + Bo)p^*) g_c(Bo) \qquad (6.16)$$

Table 6.5: List of rheological correction functions on ϕ for application in a continuum model, see Eq. (6.16).

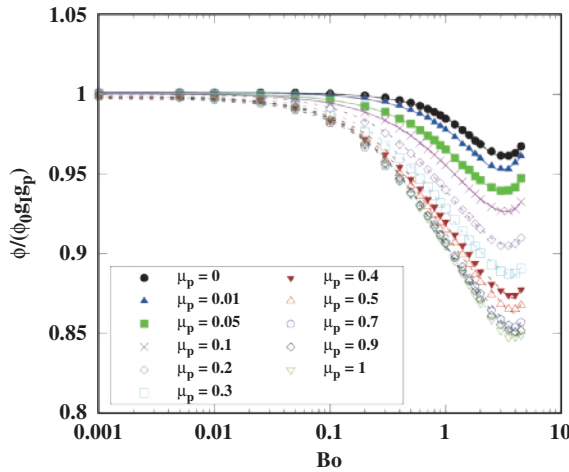| Dimensionless numbers	Corrections
Inertial number (I)	$g_I = 1 - I/I_\phi$
Softness (p^*)	$g_p = 1 + (1 + Bo)p^*/p^*_\phi$
Bond number (Bo)	$g_c = p_4 Bo^4 + p_3 Bo^3 + p_2 Bo^2$ $+ p_1 Bo + 1$

Figure 6.7: The scaled volume fraction $g_c = \phi/(\phi_0 g_I g_p)$ as a function of the Bond number Bo for different inter-particle friction coefficients as shown in the legend. The lines are the predictions of the fitted Eq. (6.15) and the data are the same as in Fig. 6.6.

In case of rigid particles, $p^* \to 0$, Eq. (6.16) reduces to $\phi_{\text{stiff}} = \phi(I,0,Bo) = \phi_0 g_I g_c$. The details of each contribution are summarized in Table 6.5.

GENERALIZED RHEOLOGY

Now we go further and include data from SB with a different contact model to compare with the data from SS. As discussed earlier in Sec. 6.2.2, we use two different contact models for the attractive forces in the two systems, SS and SB. Thus, the question arises whether the two models are influencing the systems in the same way. Since we discuss the granular rheology for soft particles, our second focus would be the effects of cohesion (Bond number) on the volume fraction, which are the increase due to the compression and decrease due to the structural change enhanced by friction. First, we illustrate our data in a slightly different way in Figure 6.8(a), plotting the scaled volume fraction $\phi/[\phi_0 g_I(I)g_c(Bo)]$ as a function of the repulsive pressure $(1 + Bo)p^*$. Unlike the previous section, here we use the function g_c from Eq. (6.15) for the scaling. In such a way, the dilation due to increase in Bond number and inertial effect due to increase in shear rate are isolated. For the case of SS, the scaled volume fraction increases with softness,

the same trend is also observed for the case of SB, regardless of non-cohesive or cohesive data.

The scaled local volume fractions $\phi/[\phi_0 g_I(I) g_c(Bo)]$ increase with the repulsive pressure $(1 + Bo)p^*$, and all the data are found to collapse on a single increasing trend that is g_p. Therefore we plot the predictions of our rheological functions as red and black solid lines in Figure 6.8(a). We see the two lines differ slightly from each other and we associate this to the small difference in the particle size distributions used in the two geometries, the simple shear box has a sample with polydispersity 3 while the split bottom shear cell has a value of 2. Nevertheless, this difference is minimal and the global trend is well captured using our new proposed rheological model. Note here, for the cohesive data of SB, the inertial number I ranges from 0.0004 to 0.0013 and the softness p^* ranges from 0.002 to 0.012, which differ from the cohesive SS data with constant I and p^*. If one expects the correction function g_c is strongly affected by different I and p^*, then these influences would show up in the data of SB where a wide range of inertial number and softness is covered. However, the influence/difference is not observed, therefore, the correction function g_c is not or maybe only very weakly affected by the dimensionless numbers I and p^*, apart from the Bond number Bo.
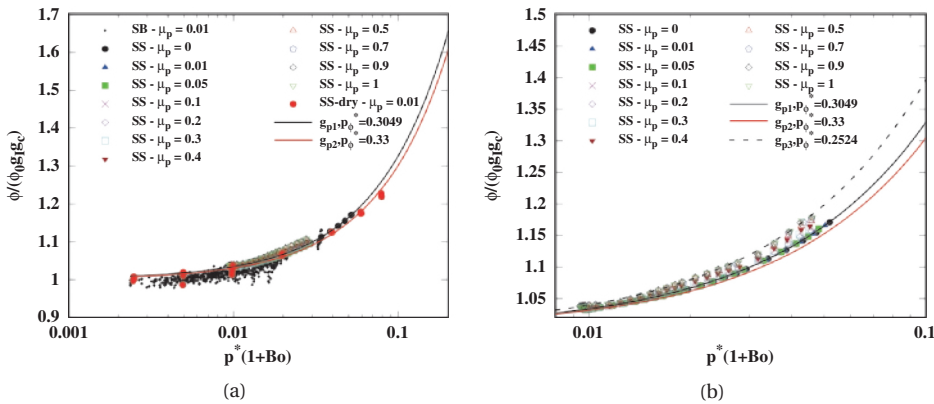

Figure 6.8: (a) The scaled volume fraction $g_p = \phi/(\phi_0 g_I g_c)$ as a function of the softness $p^*(1 + Bo)$ and (b) zoom in to the simple shear data with different inter-particle friction coefficients and Bond numbers. Different symbols represent different particle friction, where small black diamonds represent local data from the split bottom shear cell (SB) for different Bond numbers using wet cohesive capillary bridge force contact model (Fig. 6.3(b)) while all other are from homogeneous stress controlled simple shear box (SS). The red circles are the simple shear data using the normal visco-elastic contact model with no cohesive forces involved but varying shear rate and confining stress. The rest of the SS data are performed with different inter-particle friction coefficients and Bond number using the aforementioned linear reversible adhesive contact model (Fig. 6.3(a)). The black solid and dashed lines are the predictions of our rheological model Eq. (6.14) fitted using SS data with $\mu_p = 0.01$ and 1, respectively. While the red line is using SB data with the same inter-particle friction as reported in [62].

When we look closer at the cohesive data of SS as shown in Figure 6.8(b), we observe that the data deviate more from the black prediction line with increase in $p^*(1 + Bo)$. As we control all the samples having the same p^* for the data shown here, the cause of increase

in volume fraction can only be from the increase of cohesion (Bo), which is the increase
of the attractive forces among the soft particles and thus leads to compression. The re-
pulsive component of pressure is solely contributed by p^* for non-cohesive materials.
For cohesive material, the net repulsive contribution is due to the cohesive (tensile) as
well as the pressure (compressive) forces, and this effect is found to be independent of
inter-particle friction. For the Bond number up to 2, all the data are collapsing on the
single trend with less than 2% deviations, while the high Bond number data are deviat-
ing more from this trend, but still within 5% deviations up to Bond number 5. Here, the
model predictions from this work are given as lines for two values of friction: black solid
line for $\mu_p = 0.01$ and black dashed line for $\mu_p = 1$. Both lines predict the corresponding
dataset very well. The red line is slightly off the data points due to a small difference in
the polydispersity.

6.3.3. THE COMBINED EFFECT OF INTER-PARTICLE FRICTION AND COHE-SION

As mentioned earlier, cohesion among particles can lead to either compression or dila-
tion in steady granular flow relative to its non-cohesive situations. Which mechanism
dominates strongly depends on the interplay between inter-particle friction and cohe-
sion. In order to investigate how the cohesion works with friction and influences the
bulk behaviour, we choose the SS set-up and systematically vary both inter-particle fric-
tion and cohesion to check their combined influences. For each inter-particle friction,
we use the steady state volume fraction $\phi(\mu_p, I, p^*, Bo = 0)$ as reference, and subtract it
from the steady state volume fraction of other Bond numbers, $\Delta\phi = \phi(\mu_p, I, p^*, Bo) -
\phi(\mu_p, I, p^*, 0)$, defining the cohesive effect on the change of steady state volume fraction.
The positive $\Delta\phi$ indicates compression, while negative indicates dilation of the sample.
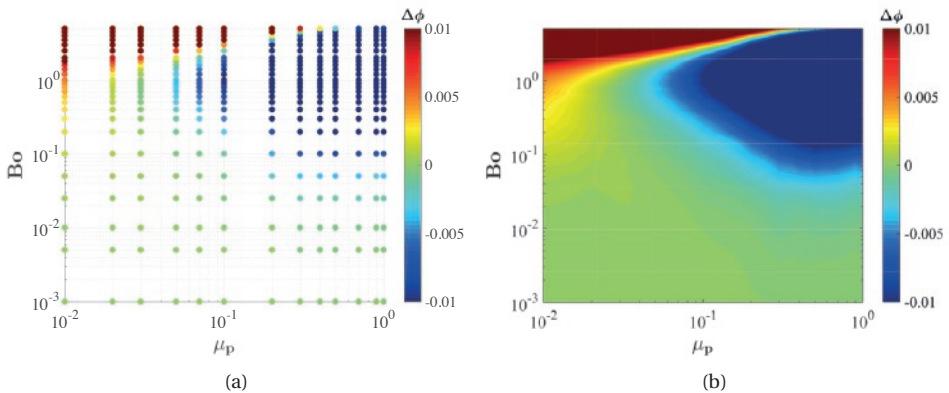
Figure 6.9: (a) The Bond number Bo plotted against inter-particle friction μ_p for change of steady state volume
fraction $\Delta\phi = \phi(\mu_p, I, p^*, Bo) - \phi(\mu_p, I, p^*, 0)$ as shown in the color bar and (b) The phase diagram created from
same data as in (a) with red and blue indicating relative compression and dilation, respectively. The Inertial
number $I = 0.016$ and softness $p^* = 0.01$ are kept constant for all the simulations shown here.

In Figure 6.9(a), we plot the dependence of $\Delta\phi$ on both inter-particle friction and Bond number. Using all points with existing colors indicating relative compression and dilation, we further calculate the isolines of $\Delta\phi$, and obtain the phase diagram as shown in Figure 6.9(b). For low to moderate cohesion, $Bo < 0.1$, volume fraction changes are inconspicuous ($\Delta\phi \approx 0$). For moderate to high cohesion range, $Bo > 0.1$, a clear compression is observed ($\Delta\phi > 0$) while relative dilation is observed ($\Delta\phi < 0$) at intermediate Bond numbers and strong inter-particle friction. However, for close to frictionless particles, when the role of friction is almost negligible, we observe a pure compression effect of the material with increasing Bo. This further confirms that sufficient inter-particle friction leads to relative dilation of cohesive flow, where cohesion plays an important role in enhancing the dilation effect.
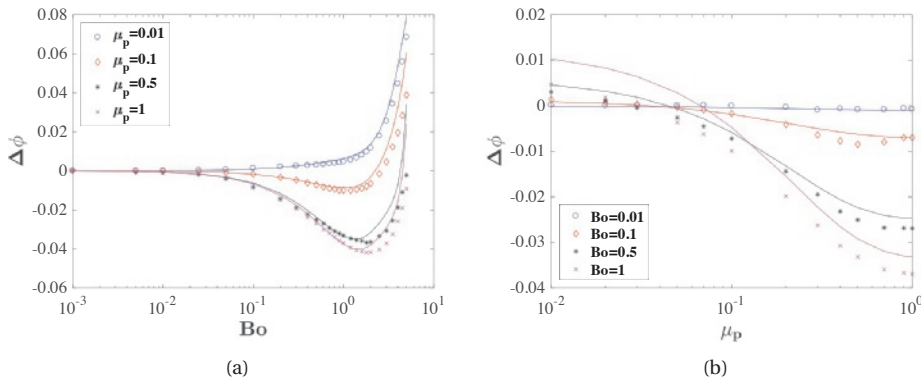

Figure 6.10: The differences of the steady state volume fractions $\Delta\phi$ plotted against (a) Bond number, Bo, for datasets with fixed inter-particle friction, μ_p, and (b) inter-particle friction, μ_p, for datasets with fixed Bond number, Bo, as shown in the legend. Lines are the predictions of our proposed model in Eq. (6.16).

Although the phase diagram offers us a nice overview of the relative compression and dilation behaviour, we further study the data by fixing one parameter and looking at the influence of the second parameter. Therefore, in Fig. 6.10(a) and Fig. 6.10(b), we plot the volume fraction for constant inter-particle friction and Bond number, respectively. When we fix the inter-particle friction and increase Bo, we observe negligible volume fraction change ($\Delta\phi \approx 0$) up to $Bo = 0.01$. If we increase the Bond number further, for low inter-particle friction ($\mu_p = 0.01$), we see a monotonically increasing trend, while for moderate to high inter-particle friction ($\mu_p > 0.01$), we get first a decrease then an increase, where the point of inflection depends on the inter-particle friction: higher inter-particle friction moves this point towards higher Bond number. This could be explained by the influence of friction: higher inter-particle friction with moderate cohesion leads to stronger dilation, but one needs even stronger cohesion to compensate the dilation effect and turn the bulk back into compression. The predictions of the rheological model are plotted as lines. Instead of using the coefficients from μ_p dependency fitting, here the actual fitted model parameters (Tables 6.3 and 6.4) from the actual data fitting are used. For all the inter-particle frictions presented here, the predictions of the model are

quite good up to Bond number around 1, then the model over predicts the difference of the volume fractions. And the over-prediction increases with the inter-particle friction. Nevertheless, our model still predicts the volume fraction values at steady state quite well, the highest deviation between the model prediction and the actual data point is around 0.02, which is roughly 4% of the error in total. Because we focus at a much smaller scale of the volume fraction here (-0.06 to 0.08), the differences between the line and the actual data points look large.

When we fix the Bond number and increase the inter-particle friction as shown in Fig. 6.10(b), we observe the turning point more clearly. If the cohesion between particles is very small ($Bo = 0.01$), the volume fraction is not changing much with inter-particle friction (relative to the $Bo = 0$ case). However, for stronger cohesion between particles ($Bo = 0.1, 1$ and 2), we see relative compression (positive values) for low inter-particle friction, which turns into relative dilation (negative values) with increasing inter-particle friction. Similarly, the predictions of the rheological model are also plotted here. As we pointed out earlier, for large Bond number, the prediction quality gets lower. Our model tends to over-predict the steady state volume fraction at higher Bond numbers, which results in large $\Delta\phi$. Note that here we focus on a even smaller scale of volume fraction ($-0.04 < \Delta\phi < 0.02$) and thus the prediction deviations are acceptable.
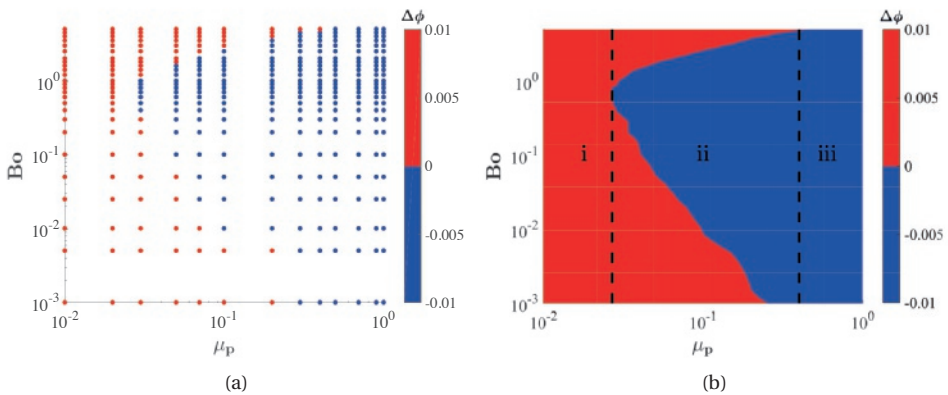
Figure 6.11: (a) The same data as in Figure 6.9(a) plotted with a different color-bar and (b) the phase diagram with a sharp red/blue-relative compression/dilation transition. The vertical lines are the boundaries between zones i-ii and ii-iii, at $\mu_p = 0.027$ and 0.4, respectively.

Although we have shown our data in the above mentioned two possible ways, it is still interesting to look further in this inconspicuous volume fraction change (green) region in Figure 6.9(b) and find out where the transition between relative compression and dilation happens. In Figure 6.11, we narrow down this transition color area between -2×10^{-10} and 2×10^{-10} and apply a two-color map. Using the data shown in Figure 6.11(a), a sharp transition line between relative compression and dilation is reconstructed and highlighted in Figure 6.11(b). In the parameter range ($0 \leq \mu_p \leq 1$ and $0 \leq Bo \leq 5$), three regimes can be identified: i) pure compression or compression for $\mu_p \lesssim 0.027$; ii) relative compression followed by relative dilation for increasing Bo and then com-

pression again for $0.03 \lesssim \mu_p \lesssim 0.40$; iii) pure relative dilation for $\mu_p \gtrsim 0.40$ (this value depends on the reference $Bo \approx 5$ chosen here). In regime i), the friction effect is almost negligible such that cohesion dominates the flow behaviour leading only to relative compression. In regime ii), both friction and cohesion affect the flow behaviour. When cohesion is low, it has a almost negligible relative compression effect, while increasing cohesion, the relative dilation from friction enhanced by cohesion increases. But when cohesion is stronger ($Bo > 1$), the relative compression effect dominates again. In regime iii), the flow shows almost only relative dilation which is mostly contributed by friction, up to $Bo \leqslant 5$. If the cohesion is extremely strong, ($Bo > 5$), we expect that relative compression contributed by cohesion dominates the system again. However, this is beyond the scope of this study and whether our simulations are homogeneous or not with such high cohesion is an open issue.

6.4. CONCLUSION AND OUTLOOK

In this study, we have extended an existing rheological model that predicts the relation between volume fraction, inertial number and softness [43], including friction and cohesion dependencies. We have calibrated this extended model without/with cohesion using two different simulation geometries: a homogeneous stress controlled simple shear box and an inhomogeneous split bottom shear cell. Furthermore, data from two geometries using two different cohesive contact models (dry, reversible vs. wet, irreversible) were compared. We systematically varied the inter-particle friction and cohesion in the stress controlled simple shear box with fixed shear rate and normal stress. We report an interesting interplay between the inter-particle friction and cohesion, as represented in phase diagrams. This allows the prediction of compression-dilation behaviour relative to non-cohesive reference steady states for various inter-particle friction coefficients.

Besides extending the rheological model towards cohesive-frictional granular media, there are two main goals here: i) to understand the relation between microscopic properties such as inter-particle friction or/and cohesion and macroscopic, bulk properties such as volume fraction; ii) to check the validity of our rheological model in both systems i.e., to confirm if the representative element volumes (REVs) could represent the center of a shear band in an inhomogeneous system. For completeness, the rheological model for the macroscopic friction is given in an appendix.

The steady state volume fraction from a homogeneous stress controlled simple shear box and an inhomogeneous split bottom shear cell (local data) in the shear band center collapse well and the rheological model captures their behaviour with varying system inertia, softness [43] and the inter-particle friction. Furthermore, we introduce a reversible van der Waals type cohesive force in the simple shear box and an irreversible liquid bridge type cohesive force in the split bottom shear cell. Independent of the type of cohesive model, if the two systems are in same steady state, e.g., same Inertial number, softness, friction and Bond number, the steady state volume fractions from the two geometries agree well in the range of parameters studied. Our extended rheological model is thus applicable in different systems. The fact that different contact models can be unified by the Bond number indicates that the macroscopic rheological behaviour of the steady state volume fraction depends on cohesion intensity but not on the microscopic

origin of cohesion between particles.

Interestingly, when investigating the effects of cohesive models, we discovered that cohesion can either contribute to a decrease or an increase of the steady state volume fraction of sheared materials, relative to the non-cohesive reference case, depending also on the inter-particle friction of materials. Using the extended rheological model, we can successfully distinguish the two contributions of cohesion: compression from the increase in the normal contact forces and relative dilation from enhancing both frictional forces as well as structural stability.

A phase diagram reveals how the combinations of these two particle parameters lead to sample compression or dilation in steady state shear, relative to a non-cohesive case. In addition, a sharp interface between compression and dilation on our phase diagram allows to categorize the explored parameter space into three regimes: i) pure relative compression for $\mu_p \lesssim 0.027$; ii) non-monotonic behaviours with Bo: relative compression followed by relative dilation for higher Bo and then relative compression again, for $0.03 \lesssim \mu_p \lesssim 0.40$; and iii) pure relative dilation for $\mu_p \gtrsim 0.40$.

The present paper is an extension of former works [32, 43] on rheological modeling, but with a deeper insight on the influence of friction and cohesion. It could be enriched by exploring more closely how the micro-structure [16] is influenced by the combination of inter-particle friction and cohesion. Furthermore, extending the rheological model towards the intermediate to low volume fraction regime, where most dense rheological models fail but kinetic theory works well, is still a great challenge. This will involve the granular temperature as at least one more relevant dimensionless number in the rheology. Moreover, comparing the stress controlled system to a volume controlled system is still ongoing research and will be addressed in the future.

APPENDIX A - MACROSCOPIC FRICTION COEFFICIENT
6.5. MACROSCOPIC FRICTION COEFFICIENT

For a full constitutive law, one also needs to take into account the shear resistance as quantified by the macroscopic friction coefficient, μ. This has been already developed in a previous work, in which the classical $\mu - I$ rheology on hard spheres was generalized for soft, cohesive granular flow [43]. These authors also studied the rheology of both dry [16] and wet [32, 43] granular materials and the trends are combined and shown to collectively contribute to the rheology [43] as multiplicative functions given by:

$$\mu := \mu(\mu_p, I, p^*, Bo) = \mu(I) f_p(p^*) f_{Bo}(Bo) \qquad (6.17)$$

where $\mu(I) = \mu_0 f_I(I)$ (see Table 6.6 or [43]) and all functions depend on one dimensionless number while their coefficients depend on particle friction, see Table 6.7.

The rheological function Eq. (6.17) presented here is slightly different from the more general form in previous work [43], since we have taken out the contributions of f_g and f_q due to absences of gravity and very small inertial numbers in the simple shear box. In particular, they found that the macroscopic friction increases linearly to first order with

Table 6.6: List of rheological correction functions on μ for application in a continuum model, see Eq. (6.17).

Dimensionless numbers	Corrections
Inertial number (I)	$f_I = 1 + \frac{\mu_\infty/\mu_0 - 1}{1 + I_\mu/I}$
Softness (p^*)	$f_p = 1 - [(1 + Bo)\,p^*/p_\mu^*]^{0.5}$
Bond number (Bo)	$f_{Bo} = 1 + \alpha_1 Bo^{\beta_1}$
Bond number (Bo) in [43]	$f_c = 1 + aBo$

Bond number. However, we propose here a new modification for the Bond number contribution with $f_{Bo} = 1 + \alpha_1 Bo^{\beta_1}$, where we claim the increase of macroscopic friction is ruled by a power law. The details of each contribution are explained in Table 6.6.

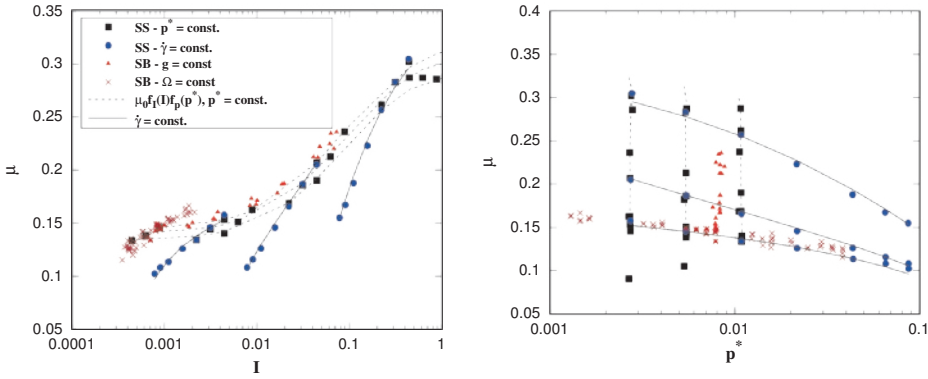### 6.5.1. NON-COHESIVE SLIGHTLY FRICTIONAL MATERIAL

Figure 6.12: The macroscopic friction coefficient, μ, plotted against inertial number, I, using the stress controlled simple shear box and the split bottom shear cell from the same simulations as shown in Fig. 6.4. The lines are the prediction of Eq. (6.17) fitted using SS data, with $\mu_0 = 0.16$, $\mu_{\text{inf}} = 0.34$, $I_\mu = 0.06$ and $p_\mu^* = 0.44$.

First we compare the data for non-cohesive slightly frictional material using the two above mentioned two shear cell setups and the results are shown in Fig. 6.12. We see an inverse trend of macroscopic friction compared to the trend of volume fraction. The macroscopic friction increases with Inertial number but decreases with softness. The lines are the prediction of Eq. (6.17) with Bond number equals to zero. The prediction is accurate when the Inertial number I is less than 0.2, but deviating with large I numbers. This could be explained by the dilation of our constant stress shear box setup. When the system goes to very high inertial regime, the stress contribution from kinetic part increase substantially and the granular bulk has to dilate in order to keep the stress constant, therefore a reduce in bulk density. Furthermore, we also compare the results between the two different setups: SS and SB, the center of shear band data of SB agrees very well with SS data, this further confirms that the shear stress responses are also the same when using the same material (same contact model) excluding the boundary ef-
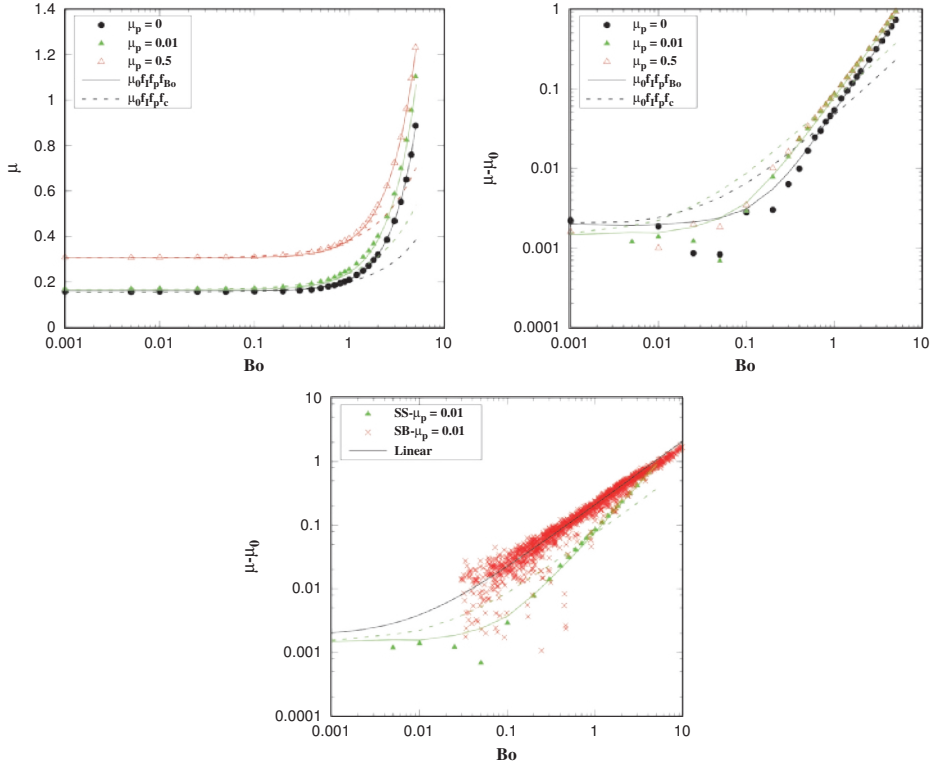
fects.

6.5.2. COHESIVE MATERIALS

Figure 6.13: The macroscopic friction coefficient μ as a function of Bond number Bo for inter-particle friction coefficient $\mu_p = 0, 0.01$ and 0.5. The Inertial number $I = 0.001$ and softness $p^* = 0.01$ are kept constant for all the simulations shown here. Solid line is the prediction of Eq. (6.17) while dashed lines are prediction using the linear form from [43].

In Figure 6.13, we plot the macroscopic friction, μ, against Bond number, Bo, with also the predictions of our proposed rheological model. For the sake of clearness, we only plot data of three inter-particle friction coefficients instead of all the data we have. With increase the cohesion in the system, the macroscopic friction stay almost constant when $Bo < 0.2$, but increase rapidly when the cohesion gets stronger ($Bo > 0.2$). The high attractive force between particles leads to a more stable packing, thus higher resistance to the shear. We have also included the predictions from both our modified rheological model and the model from previous work [43], shown as solid and dashed lines, respectively. The model from previous work can only capture the behaviour at low Bond number ($Bo < 0.1$), while our modified model agree very well with the DPM data. A possible reason that previous model agree well with split bottom shear cell data is they were

fitting the data though a data cloud, which could introduce higher deviations. While the data from simple shear box are cleaner and allow us to take close look at the influence of cohesion more accurately. All the model parameters are summarized in Table 6.7.

If we look at all the friction data (data not shown), we observe that the macroscopic friction increases first with inter-particle friction coefficient, but then decreases again for $\mu_p > 0.3$. This non-monotonic trend might be caused by the friction induced, cohesion enhanced micro-structural anisotropy. The shear stress also shows similar trend as macroscopic friction while the pressure is changing continuously.

The granular temperature time scale, t_T is comparable to the shear time scale $t_{\dot{\gamma}}$ but slightly smaller, while they are both much larger than the pressure time scale t_p, which indicates that neither granular temperature nor shear are the dominating mechanisms for the friction trend.

Table 6.7: The fitting coefficients of rheological model on macroscopic friction.

μ_p	μ_0	μ_{inf}	I_μ	p_μ^*	α_1	β_1	a (this work)	a (in [43])
0.00 (SS)	0.1342	0.3163	0.0445	0.3662	0.3136	1.6475	0.2820	[-]
0.01 (SS)	0.1622	0.3363	0.0621	0.4360	0.4490	1.5218	0.4280	[-]
0.01 (SB)	0.16	0.40	0.07	0.9	[-]	[-]	[-]	1.47
0.50 (SS)	0.3549	0.6333	0.5301	0.4037	0.2551	1.5125	0.2496	[-]

6

APPENDIX B - THE INFLUENCE OF INTER-PARTICLE FRICTION ON THE COEFFICIENTS IN THE RHEOLOGICAL MODEL OF VOLUME FRACTION

For the completeness, one has to also look at the dependency of the inter-particle friction μ_p on the fitting coefficients obtained in our proposed rheological model as presented in Table 6.3 and 6.4. The function used to describe this dependency is as follows:

$$Q = Q_\infty + (Q_0 - Q_\infty)e^{(-\mu_p/\mu_p^0)} \tag{6.18}$$

where Q represents the coefficients obtained from the rheological model, Q_∞ and Q_0 represent the values of the coefficient at zero and infinite μ_p limits, respectively. While μ_p^0 refers to the inter-particle friction at which the change of coefficient is saturating with the increase of μ_p.

For all the model coefficients, our proposed dependency law fit well on most of the data points with very small values of Root-Mean-Square (RMS) Residuals, see the summarized details in Table 6.8. For the sake of brevity, we only plot here two coefficients out of seven due to the similar behaviour among all the coefficients. The results are shown in Figure 6.14 with the dependencies of μ_p on ϕ_0 and p_1 in (a) and (b), respectively. In the case of ϕ_0, it decrease quickly up to μ_p around 0.34, then the decrease becomes weaker and saturates towards large μ_p. While for the cohesive coefficient p_1, the decrease becomes weaker at μ_p around 0.23, and this saturation turning points are very similar for all the other cohesive coefficients p_3, p_2 and p_1 (see Table 6.8).

Table 6.8: The summary of fitting coefficients in Eq. (6.18)

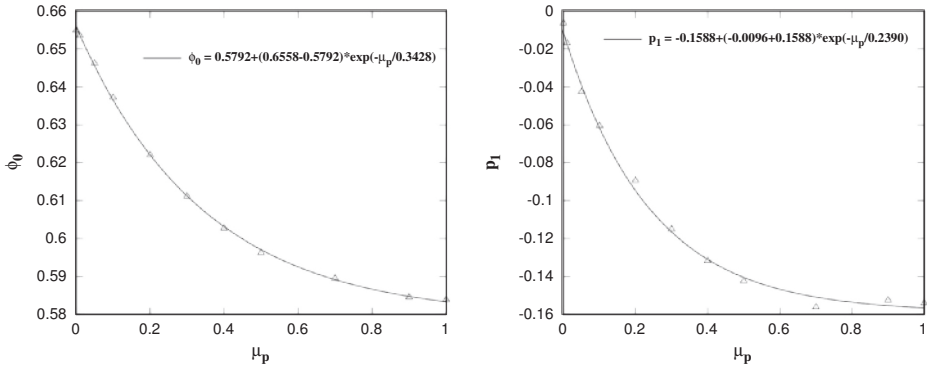| Coefficients	Q_∞	Q_0	μ_p^0	RMS Residuals
ϕ_0	0.5792	0.6558	0.3428	0.00063
I_ϕ	7.3644	2.6130	0.7169	0.09224
p_ϕ^*	0.2404	0.3065	0.5663	0.00189
p_4	0.0018	-0.0005	0.2354	0.00013
p_3	-0.0191	0.0051	0.2323	0.00120
p_2	0.0779	-0.0121	0.2291	0.00345
p_1	-0.1588	-0.0096	0.2390	0.00367

Figure 6.14: The dependency of inter-particle friction, μ_p, on (a) the fitting coefficient from dry cohesive model, ϕ_0, in Eq. (6.13); (b) the fitting coefficient from cohesive model, p_1, in Eq. (6.15). The lines are the prediction of Eq. (6.18) and the details are explained in the legend.

REFERENCES

[1] S. B. Savage and K. Hutter, *The motion of a finite mass of granular material down a rough incline,* J. Fluid Mech. **199**, 177 (1989).

[2] G. D. R. MiDi, *On dense granular flows,* Eur. Phys. J. E **14**, 341 (2004).

[3] J. Tomas, *Product Design of Cohesive Powders – Mechanical Properties, Compression and Flow Behavior,* Chem. Eng. Technol. **27** (2004).

[4] F. Alonso-Marroquin and H. J. Herrmann, *Ratcheting of granular materials,* Phys. Rev. Lett. **92**, 54301 (2004).

[5] S. Luding, *Shear flow modeling of cohesive and frictional fine powder,* Powder Technol. **158**, 45 (2005).

[6] A. J. Liu and S. R. Nagel, *Nonlinear dynamics: Jamming is not just cool any more,* Nature **396**, 21 (1998).

[7] D. Bi, J. Zhang, B. Chakraborty, and R. P. Behringer, *Jamming by shear,* Nature **480**, 355 (2011).

[8] S. Luding, *Granular matter: So much for the jamming point,* Nature **12**, 531 (2016).

[9] N. Kumar and S. Luding, *Memory of jamming–multiscale models for soft and granular matter,* Granular matter **18**, 1 (2016).

[10] M. E. Cates, M. D. Haw, and C. B. Holmes, *Dilatancy, jamming, and the physics of granulation,* Journal of Physics: Condensed Matter **17** (2005).

[11] M. Van Hecke, *Jamming of soft particles: geometry, mechanics, scaling and isostaticity,* Journal of Physics: Condensed Matter **22**, 033101 (2009).

[12] Y. Yang, W. Fei, H.-S. Yu, J. Ooi, and M. Rotter, *Experimental study of anisotropy and non-coaxiality of granular solids,* Granular Matter **17**, 189 (2015).

[13] P. A. Cundall, *Numerical experiments on localization in frictional materials,* Ingenieur-Archiv **59**, 148 (1989).

[14] K. A. Alshibli and S. Sture, *Shear band formation in plane strain experiments of sand,* Journal of Geotechnical and Geoenvironmental Engineering **126**, 495 (2000).

[15] B. Wolf, R. Scirocco, W. J. Frith, and I. T. Norton, *Shear-induced anisotropic microstructure in phase-separated biopolymer mixtures,* Food Hydrocolloids **14**, 217 (2000).

[16] A. Singh, V. Magnanimo, K. Saitoh, and S. Luding, *Effect of cohesion on shear banding in quasistatic granular materials,* Phys. Rev. E **90**, 022202+ (2014).

[17] S. C. Thakur, H. Ahmadian, J. Sun, and J. Y. Ooi, *An experimental and numerical study of packing, compression, and caking behaviour of detergent powders,* Particuology **12**, 2 (2014).

[18] F. Radjai, M. Jean, J. J. Moreau, and S. Roux, *Force Distribution in Dense Two-Dimensional Granular Systems,* Phys. Rev. Lett. **77**, 274 (1996).

[19] F. Radjai, S. Roux, and J. J. Moreau, *Contact forces in a granular packing.* Chaos **9**, 544 (1999).

[20] T. S. Majmudar and R. P. Behringer, *Contact force measurements and stress-induced anisotropy in granular materials,* Nature **435**, 1079 (2005).

[21] S. Luding, *Anisotropy in cohesive, frictional granular media,* J. Phys. Condens. Matter **17** (2005).

[22] A. N. Schofield and C. P. Wroth, *Critical state soil mechanics* (McGraw-Hill, London, 1968).

[23] L. E. Silbert, G. S. Grest, T. C. Halsey, D. Levine, and S. J. Plimpton, *Granular flow down an inclined plane: Bagnold scaling and rheology,* Phys. Rev. E **64** (2001).

[24] P. G. Rognon, J. N. Roux, M. Naaim, and F. Chevoir, *Dense flows of cohesive granular materials,* J. Fluid Mech. **596**, 21 (2008).

6

[25] P. Richard, A. Valance, J. F. Métayer, P. Sanchez, J. Crassous, M. Louge, and R. Delannay, *Rheology of Confined Granular Flows: Scale Invariance, Glass Transition, and Friction Weakening,* Phys. Rev. Lett. **101**, 248002 (2008).

[26] O. Pouliquen and Y. Forterre, *A non-local rheology for dense granular flows,* Philosophical Transactions of the Royal Society of London A: Mathematical, Physical and Engineering Sciences **367**, 5091 (2009).

[27] V. Vidyapati, M. K. Langroudi, J. Sun, S. Sundaresan, G. I. Tardos, and S. Subramaniam, *Experimental and computational studies of dense granular flow: Transition from quasi-static to intermediate regime in a couette shear device,* Powder technology **220**, 7 (2012).

[28] S. Chialvo, J. Sun, and S. Sundaresan, *Bridging the rheology of granular flows in three regimes,* Phys. Rev. E **85**, 021305 (2012).

[29] R. Schwarze, A. Gladkyy, F. Uhlig, and S. Luding, *Rheology of weakly wetted granular materials: a comparison of experimental and numerical data,* Granul. Matter. **15**, 455 (2013).

[30] Y. Gu, S. Chialvo, and S. Sundaresan, *Rheology of cohesive granular materials across multiple dense-flow regimes,* Phys. Rev. E **90**, 032206 (2014).

[31] R. Mari, R. Seto, J. F. Morris, and M. M. Denn, *Shear thickening, frictionless and frictional rheologies in non-brownian suspensions,* Journal of Rheology **58**, 1693 (2014).

[32] A. Singh, V. Magnanimo, K. Saitoh, and S. Luding, *The role of gravity or pressure and contact stiffness in granular rheology,* New J. Phys. **17**, 043028 (2015).

[33] D. Vescovi and S. Luding, *Merging fluid and solid granular behavior,* Soft matter **12**, 8616 (2016).

[34] S. Mandal and D. V. Khakhar, *A study of the rheology of planar granular flow of dumbbells using discrete element method simulations,* Physics of Fluids **28**, 103301 (2016).

[35] K. Mair, K. M. Frye, and C. Marone, *Influence of grain characteristics on the friction of granular shear zones,* J. Geophys. Res. **107**, 2219+ (2002).

[36] Y. Guo and J. K. Morgan, *Influence of normal stress and grain shape on granular friction: Results of discrete element simulations,* Journal of Geophysical Research: Solid Earth **109** (2004).

[37] S. Luding, *The Effect of Friction on Wide Shear Bands,* Particulate Science and Technology **26**, 33 (2007).

[38] J. Härtl and J. Y. Ooi, *Experiments and simulations of direct shear tests: porosity, contact friction and bulk friction,* Granul. Matter. **10**, 263 (2008).

[39] J. Härtl and J. Y. Ooi, *Numerical investigation of particle shape and particle friction on limiting bulk friction in direct shear tests and comparison with experiments,* Powder Technology **212**, 231 (2011).

[40] A. Singh, V. Magnanimo, and S. Luding, *Effect of friction and cohesion on anisotropy in quasi-static granular materials under shear,* AIP Conf. Proc. **1542**, 682 (2013).

[41] K. Kamrin and G. Koval, *Effect of particle surface friction on nonlocal constitutive behavior of flowing granular media,* Computational Particle Mechanics **1**, 169 (2014).

[42] S. Roy, S. Luding, and T. Weinhart, *Effect of cohesion on local compaction and granulation of sheared soft granular materials,* in *EPJ Web of Conferences,* Vol. 140 (EDP Sciences, 2017) p. 03065.

[43] S. Roy, S. Luding, and T. Weinhart, *A general(ized) local rheology for wet granular materials,* New Journal of Physics **19**, 043014 (2017).

[44] C. Ness, J. Y. Ooi, J. Sun, M. Marigo, P. McGuire, H. Xu, and H. Stitt, *Linking particle properties to dense suspension extrusion flow characteristics using discrete element simulations,* AIChE Journal **63**, 3069 (2017).

[45] P. Rognon, J. N. Roux, D. Wolf, M. Naaim, and F. Chevoir, *Rheophysics of cohesive granular materials,* Europhys. Lett. **74**, 644 (2006).

[46] S. Roy, A. Singh, S. Luding, and T. Weinhart, *Micro-macro transition and simplified contact models for wet granular materials,* Computational particle mechanics **3**, 449 (2016).

[47] C. D. Willett, M. J. Adams, S. A. Johnson, and J. Seville, *Capillary bridges between two spherical bodies,* Langmuir **16**, 9396 (2000).

[48] T. Weigert and S. Ripperger, *Calculation of the Liquid Bridge Volume and Bulk Saturation from the Halflling Angle,* Particle Particle Systems Characterization **16** (1999).

[49] F. Soulié, F. Cherblanc, M. S. El Youssoufi, and C. Saix, *Influence of liquid bridges on the mechanical behaviour of polydisperse granular materials,* Int. J. Numer. Anal. Meth. Geomech. **30**, 213 (2006).

[50] A. Gladkyy and R. Schwarze, *Comparison of different capillary bridge models for application in the discrete element method,* Granular Matter **16**, 911 (2014).

[51] P. Lambert, A. Chau, A. Delchambre, and S. Régnier, *Comparison between two capillary forces models,* Langmuir : the ACS journal of surfaces and colloids **24**, 3157 (2008).

[52] A. Santomaso, P. Lazzaro, and P. Canu, *Powder flowability and density ratios: the impact of granules packing,* Chemical Engineering Science **58**, 2857 (2003).

[53] H. Shi, R. Mohanty, S. Chakravarty, R. Cabiscol, M. Morgeneyer, H. Zetzener, J. Y. Ooi, A. Kwade, S. Luding, and V. Magnanimo, *Effect of particle size and cohesion on powder yielding and flow,* KONA Powder and Particle Journal **35**, 226 (2018).

6

[54] V. Richefeu, M. S. Youssoufi, and F. Radjai, *Shear strength properties of wet granular materials,* Phys. Rev. E **73** (2006), 10.1103/physreve.73.051304.

[55] S. Roy, S. Luding, and T. Weinhart, *Liquid redistribution in sheared wet granular media,* Phys. Rev. E **98**, 052906 (2018).

[56] Z. Fournier, D. Geromichalos, S. Herminghaus, M. M. Kohonen, F. Mugele, M. Scheel, M. Schulz, B. Schulz, C. Schier, R. Seemann, and A. Skudelny, *Mechanical properties of wet granular materials,* J. Phys.: Condens. Matter **17**, S477 (2005).

[57] J. Tomas, *Fundamentals of cohesive powder consolidation and flow,* Granul. Matter **6**, 75 (2004).

[58] S. Luding, *Introduction to discete element methods: Basics of contact force models and how to perform the micro-marco transition to continuum theory,* Euro. J. of Enviro. Civ. Eng. **12**, 785 (2008).

[59] S. Masson and J. Martinez, *Effect of particle mechanical properties on silo flow and stresses from distinct element simulations,* Powder Technol. **109** (2000), 10.1016/S0032-5910(99)00234-X.

[60] S. Luding, *From microscopic simulations to macroscopic material behavior,* Computer Physics Communications **147**, 140 (2002).

[61] M. J. Jiang, J. M. Konrad, and S. Leroueil, *An efficient technique for generating homogeneous specimens for DEM studies,* Computers and Geotechnics **30**, 579 (2003).

[62] S. Luding, A. Singh, S. Roy, D. Vescovi, T. Weinhart, and V. Magnanimo, *From particles in steady state shear bands via micro-macro to macroscopic rheology laws,* The 7th International Conference on Discrete Element Methods. (2016).

[63] T. Weinhart, A. R. Thornton, S. Luding, and O. Bokhove, *From discrete particles to continuum fields near a boundary,* Granul. Matter. **14**, 289 (2012).

[64] A. Thornton, T. Weinhart, S. Luding, and O. Bokhove, *Modeling of particle size segregation: calibration using the discrete particle method,* Int. J. Mod. Phys. C **23**, 1240014 (2012).

[65] T. Weinhart, D. Tunuguntla, M. van Schrojenstein-Lantman, A. Van Der Horn, I. Denissen, C. Windows-Yule, A. de Jong, and A. Thornton, *Mercurydpm: A fast and flexible particle solver part a: Technical advances,* in *International Conference on Discrete Element Methods* (Springer, 2016) pp. 1353–1360.

[66] A. W. Lees and S. F. Edwards, *The computer study of transport processes under extreme conditions,* J. Phys. C: Solid State Phys. **5**, 1921 (1972).

[67] H. Shi, D. Vescovi, A. Singh, S. Roy, V. Magnanimo, and S. Luding, *Granular flow: From dilute to jammed states,* in *Granular Materials,* edited by M. Sakellariou (InTech, 2017).

[68] H. Shi, S. Luding, and V. Magnanimo, *Steady state rheology from homogeneous and locally averaged simple shear simulations,* in *EPJ Web of Conferences*, Vol. 140 (EDP Sciences, 2017) p. 03070.

[69] S. Roy, S. Luding, and T. Weinhart, *Towards hydrodynamic simulations of wet particle systems,* Procedia Engineering **102**, 1531 (2015).

[70] S. Luding, *Cohesive, frictional powders: contact models for tension,* Granul. Matter **10**, 235 (2008).

[71] S. Gonzalez, A. R. Thornton, and S. Luding, *Free cooling phase-diagram of hard-spheres with short-and long-range interactions,* The European Physical Journal Special Topics **223**, 2205 (2014).

[72] S. Luding, *From particles in steady state shear bands via micro-macro to macroscopic rheology laws,* Proceedings of the 5th International Symposium on Reliable Flow of Particulate Solids (RELPOWFLO V) (2017).

[73] M. Alam, J. T. Willits, B. O. Arnarson, and S. Luding, *Kinetic theory of a binary mixture of nearly elastic disks with size and mass disparity,* Physics of Fluids **14**, 4087 (2002).

[74] J. T. Jenkins and C. Zhang, *Kinetic Theory for Identical, Frictional, Nearly Elastic Spheres,* Physics of Fluids **14**, 1228 (2002).

[75] I. Goldhirsch, *Rapid granular flows,* Annu. Rev. Fluid Mech. **35**, 267 (2003).

[76] D. Berzi and D. Vescovi, *Different singularities in the functions of extended kinetic theory at the origin of the yield stress in granular flows,* Physics of fluids **27**, 013302 (2015).

[77] N. Berger, E. Azéma, J. F. Douce, and F. Radjai, *Scaling behaviour of cohesive granular flows,* EPL (Europhysics Letters) **112**, 64004 (2016).

[78] S. Khamseh, J.-N. Roux, and F. Chevoir, *Flow of wet granular materials: A numerical study,* Physical Review E **92**, 022201 (2015).

6

7

CONCLUSIONS AND OUTLOOK

The general focus of this thesis is to study the deformation behaviour of a wide range of granular materials from free flowing to cohesive under different stress, strain and dynamic conditions. Main goal is to bridge the gap between the micro-mechanical parameters and macroscopic bulk mechanical responses, for granular flow in a rotating drum/shear cell or during tabletting. This interesting, complex challenge is approached both by experimental laboratory tests and numerical investigation using discrete element method.

The mechanical properties of dry cohesive powders are important both for practical and fundamental reasons. Bulk flow/failure behaviour of powders are quantified by bulk friction/cohesion, which are intrinsically connected to the micro-mechanical properties, i.e., inter-particle friction/cohesion. Powders have been studied since decades with many different tests, from low to high stress regime and from slow to high deformation rates. Most of these studies are either material specific in order to compare different devices or device specific in order to compare sample differences. In the latter case, most samples are having very different chemical compositions and thus different micro-mechanical properties, which makes it impossible to isolate single physical influencing factors. Given that very little was explored focusing on both influence from devices and materials together, the first part of this thesis focuses on the shear flow behaviour of a wide size range of limestone powders with the same chemical composition in various experimental devices, in order to access also a wide confining pressure range which can not be realized in a single device.

In Chapter 2 of this thesis, we have systematically examined the flow behaviour of limestone powder samples with varying median particle sizes in different shear testers at different confining pressure levels. Both factors, median particle size and confining pressure, are found to influence the bulk flow significantly. When we look at the dependence of the macroscopic flow on the median particle size, two regimes can be distinguished, above and below about 150 μm. The competition between contact cohesion and geometrical effects can explain the transition between the two regimes. The interlocking

between particles due to the surface roughness and shape dominates the bulk behaviour of coarse samples, while cohesion is the key contribution that governs the shear strength of fine powders.

Using the same set of the limestone powders, we have further investigated the micro-macro link of the powder deformations towards either very high or very low confining pressures, or even free surface conditions. In Chapters 3 and 4, we have showcased how our powders behave in high load compaction/tabletting process and low stress rotating drum/angle of repose, respectively. With increasing the pressure to very high levels during compaction, the powder bed experienced tremendous deformations with reducing the free space between primary particles, the volume of each particle due to contact plastic deformation and fractures (particle's shape becomes irrelevant). This results in a huge increase in the bulk density, the smaller the particle size, the larger the increase. After tablets are formed by compaction, their tensile strengths follow a monotonic decreasing trend with median particle size, but not for powders with very small particle sizes. This indicates that the microscopic cohesion between primary particles does not always lead to an increase in the bulk strength; in other words, microscopic cohesion for small particles will weaken the strength of the tablet at a given compaction pressure.

When we look at very low confining pressure using same cohesive powder in Chapter 4, the static angle of repose and dynamic friction angle both increase with decrease in median particle size. The macroscopic friction of powder bed is dominated by the microscopic cohesion. The increase in the cohesion results also an increase in the shear resistance, thus macroscopic friction. Choosing the low speed limit of a dynamic drum test and the low stress limit for quasi-static shear test, the drum flowing angle and the shear cell friction angle are converging for both free flowing and cohesive limestone powders. This connection between different tests opens new perspectives in the field of powder flow characterization for measurement interpretation and also for a better link with powder behavior in industrial process lines. Furthermore, the geometrical interlocking effect we found in Chapter 2 for intermediate confining pressure seems to become irrelevant in both very high and very low confining pressure regimes.

Using the same spirit of micro-macro mapping, we focus on the numerical study of dry, cohesive granular flows in the second part of this thesis. Instead of trying a classical calibration-validation approach to match our numerical results to real experiment case-wisely, we choose to investigate the influences from both micro-mechanical particle properties and state variables systematically to get a better understanding of how they cross-correlate to each other. As a result, we propose a generalized rheological model to describe the density and macroscopic friction of granular flow in a wide range of varying system inertia, pressure, microscopic inter-particle friction and cohesion.

Chapter 5 provides a few methods and some phenomenology with two popular theories that can describe well dilute and dense granular flow respectively. Various recent works attempted to combine those limit-cases and provide first combined, generalized theories that go beyond the classical states. However, due to dissipation, friction, cohesion, non-sphericity of realistic materials, this poses still plenty of challenges. Therefore, in Chapter 6, we extended an existing rheological model that predicts the volume fraction depending on the inter-particle friction and the softness of materials and cali-

brated with/without cohesion using two different simulation geometries: homogeneous stress controlled simple shear box and inhomogeneous split bottom shear cell. In addition, two adhesion contact models representing van der Waal's force and liquid bridge force are also compared. The maximum adhesive force associated with the confining stress is found to be one key parameter that determines the steady state volume fraction, while the shape of the force-displacement curve determines the qualitative behaviour of the final shear resistance at the steady state. Furthermore, the interplay between inter-particle friction and cohesion can either cause a decrease or an increase in the steady state volume fraction of sheared materials relative to the non-cohesive reference case. This interesting effect is summarized by plotting the change of steady state volume fractions on a phase diagram and gives a further insight into the role of cohesion and geometrical interlocking that we found in Chapter 2.

Finally, some important messages and conclusions from this thesis:

1. The median particle size pre-determines the microscopic cohesion and geometrical interlocking, which are the key dominating elements to the bulk density and bulk friction of powder flow at intermediate confining stress.

2. At high pressure, the geometrical interlocking effect becomes irrelevant due to high plastic deformation indicating possibly fracture of primary particles so that microscopic cohesion becomes the dominating factor to the stress-strain responses.

3. In very low to almost zero confining pressure situations, the microscopic cohesion dominates again the bulk flow behaviour, whereas the geometrical interlocking effect is negligible because primary particles have large free space to move.

4. Good agreement is found among static angle of repose tests, quasi-static ring shear tests and dynamic rotating drum tests, by stretching the rotating drum to low speed limit and the ring shear test to low confining stress limit.

5. The existing constitutive model that includes shear rate, softness, and other dimensionless control parameters is further generalized including the influences of micro-mechanical properties such as friction and cohesion on the local volume fraction and bulk friction, which forms the basis of continuum modeling of general granular flows.

OUTLOOK

1. The systematic shear tests over a wide range of limestone powders are the beginning of a collection of experimental data that, in future, can be enriched with more materials of both industrial and academic interest. Furthermore, this experimental database can be used as a source for design (e.g. silo) procedures, as a benchmark for further experimental studies, and for the calibration/validation of the DEM contact models.

2. Our speculations on the interesting bulk cohesion and friction behaviour with increasing particle size is only based on one type of material. This could be further verified with additional materials.

3. After the investigation of the high load compaction of our limestone powders, we realized that there is still a gap to connect the macroscopic responses, e.g. bulk density or tablet tensile strength to the micro-mechanical forces. Further study focusing on the modeling of powder compaction and identifying the micro-mechanical origins are still challenges to be addressed.

4. The connections among static, quasi-static and dynamic tests are based on empirical relations and extrapolations. There is still a need to conduct more accurate studies to find the true relations at and beyond the limits of different types of tests, either directly or indirectly.

5. Our generalized phenomenological rheology takes into account the effect of different micro-mechanical mechanisms via dimensionless numbers of the state variables and material properties, which can capture multiple effects of varying confining pressure, flow inertia, particle softness and cohesion at the same time. However, the effect of kinetic energy of the particles' random motion quantitatively by the granular temperature is still missing and needs to be included.

6. The current general rheological model only focuses on dense granular flow with a limited range of softness/pressure. A more generalized rheology towards the intermediate to low volume fraction regime, where the standard kinetic theory rules, as well as covering a wider range of shear rate and pressure is still a great challenge.

7. Another prospective domain that still lacks clarity is to study the combined effects of inter-particle friction and cohesion on the micro-structure inside granular flows, such as the fabric and contact anisotropy.

8. Our goal here was to define the rheology of granular materials in a continuum framework. Now, the overall constitutive relations mentioned above are to be implemented in continuum solvers to recover or even predict flow phenomena such as shear bands and patterns, allowing for the practically relevant simulation of large systems where DEM simulations are no longer possible due to too large number of particles.

ACKNOWLEDGEMENTS

"I listen and I forget, I see and I remember, I do and I understand." - Chinese Proverb

The whole adventure of my PhD journey started from the first meeting with Prof. Stefan Luding in March 2014 on a local Germany conference ProcessNet in Magdeburg. Back then I was only finishing my master thesis focusing on the mechanical behaviour of a single particle. Now I am so confident in doing modeling of bulk behaviours of many particles in a process, on both micro and macro scale levels. Regarding my interest towards research, I own a big "thank you" to Dr. Alexander Russell, who guided me through the whole experimental work of my master thesis and brought the position information to me and encouraged me to apply for it. Prof. Dr. Jürgen Tomas plays an equally important role in inspiring me to think about the career in doing science. It is a great loss to all of us that he passed away in 2015. Probably, he is happy in the heaven seeing his student carrying on the research work further.

After four and half years work, I reach this moment of writing the dissertation. It would never happen without the accompanies and supports from the people surrounding me. It is a great pleasure that I have now the opportunity to express my gratitude to all of them.

First and foremost, I would like to thank my supervisor and promoter, Prof. Stefan Luding for accepting me in his group. Being under your tutelage for these years has given me an opportunity to learn how to open the granular world in a right way, how to unfold the unknown physical problems logically and elegantly. You have also given me many chances to travel to international conferences and see how the world looks like, which has broaden my view so much. The discussions, comments, advices and iterations on our works have taught me how to conduct scientific work with integrity and patience. You are very easygoing, patient and know how to make me feel cosy working and learning with you. There is a Chinese proverb: "When you touch black, you become black, when you touch red, you become red." I think this describe perfectly how you have influenced me, both on ways of exploring unknown questions and the tricks to manage well between the work and the personal life. It is my luck to have you as my main supervisor, if anyone ever asks me about my PhD supervisor Stefan Luding, I would reply back: "He is awesome!". I would also like to thank your wife Gerlinde, who told us many interesting stories of your past time and made us feel less homesick here in the Netherlands, and also showing the nice sewing work she has done, which inspired my wife to also do the nice sewing work at home.

Dr. Vanessa Magnanimo, my co-supervisor, your day-to-day advice and supervision has been really invaluable to me. I want to say a big Thank You. It is undoubtedly that you are the best person as a daily supervisor. You always brought the questions and com-

ments from the engineering point of view which broadened my visions and approaches in dealing with various problems. You put always a lot of efforts on giving comments, suggestions and criticisms to let me improve the way of interpreting my scientific results, especially how to present all logically connected results. Without your help and suggestions, this thesis would never have been as ready as now. Apart from the scientific guidance, you also care about my family and personal life and ask me frequently how is it going with everything. I really appreciate that you understand well my personal difficulties and take out or shift some work related pressures for my sake. You also brought me into this FFNT in UT and I had a chance to see how the other people do the work-life balance, which helped me in applying to my own situation.

Dr. Thomas Weinhart, although you are not my direct supervisor, I also want to say a great ""thank you to you as you guided and helped me so much on the numerical simulation part of my PhD. It is very nice to talk and discuss with you my scientific work as well as the general life here. You brought me into light whenever I seem to have stuck in a dark corner while I am coding, which is the skill I am not good at. Your mathematician ways of answering questions always brought in the new perspective to the solutions and inspired me to also think outside the box. I am really fortunate to have you by my side for the entire journey. Thomas, I want to also extend my thanks to your wife Raquel for the nice family meetings. She is always happy to help around and bring Emma and Lukas to play with Iris, I really appreciate this point which makes us feel less lonely here abroad.

I would like to extend my thanks to Dr. Anthony Thornton for offering the new position after my PhD and nice memories we had during conferences, traveling and also inside the office. Anthony, although I could not understand you well in the first 3 months after my arrival in the group, I am now more confident in discussing both scientific work and life with you. Your way of expressing things sounds always interesting/difficult to me, but yet very cheerful into my mood. You have a very wide knowledge in every aspect and I have learned a lot from you.

Sylvia, you are the light for the group, the same light that led me towards the end of my PhD. It could never been achieved like this without your help. You are always trying to help us no matter what problem we encounter and arrange the group in such a nice way. I have also got to know your husband Han, he is also such a nice man who always brings us energy and happiness after we have talked to each other. To both of you, I want to say a big thank you.

Thank you, Dr. Wouter den Otter for the novel ideas always on our seminars and discussions. Also my sincere thank to Wouter den Breeijen for your support on the technical side of the hardware and software and contributions to this dissertation. Furthermore, I want to extend my gratitude towards my colleagues here in the group and in the other groups. I would like to thank Durai, Giuseppe, Abhi, Kay, Nishant, Ahmed, Bert, Sudeshna, Mitchel, Deepak, Kuni, Dalila, Marnix, Irana, Hongyang, Sampann, Thejas, Ranisha and Beybin for your nice collaborations and discussions. Durai, you are the first colleague I have met here in the group and we were neighbors for the first year inside the campus, we had so many nice memories together, cooking, eating, watching movies, traveling and many other things. Thank you so much for accompanying me through this period. Now you move to Bangalore and start a new career and life there, I wish you

all the best and you are always my best friend, no matter where you are on this earth. Bert, you are the first Dutch colleague I talked to the most. You are always there helping me, explain the difficult Dutch cultures and also translating Dutch documents for me, especially for the "Samenvatting" in this dissertation, it could not be finished without you. You also helped me a lot outside the work, e.g. before I moved to the apartment, you helped me installing the lights and curtains. I want to say thank you from my heart. Ahmed, you are the best/humorous/talented person I have ever met. You are always with me and sitting besides me through my dark time. We work on the experiments together and hopefully we will have a paper together soon. You also helped me design such a nice cover page, thank you for all the efforts and time you were with me, I could never reach what I am now without your contribution.

It is also equally important to mention the persons I met beyond the University of Twente, I would like to thank Dr. Pablo García Triñanes and Prof. Geoffory Lumay for your time on collaborating with me and also all the people in T-MAPPP project, especially to Ramon Cabiscol. Ramon, you are always nice and helpful to me. It is a great luck that I have you as my collaborator, you put so much efforts in doing experiments for me and also arrange the devices for me to use. Half of this dissertation has your contribution and I own you a very very big thank you!

I would like to thank all my committee members for their interests in my research. I am grateful to Dr. Michel Duits who took all the efforts to make a careful assessment of my thesis. Thanks to Prof. Arno Kwade, Prof. Jin Ooi, Prof. Ruud van Ommen and Prof. Devaraj van der Meer for your kind appreciations of my work.

Finally, I'd like to thank my family. To my mum, Hua and my mother in law, Anjin, this achievement would not have been possible without you taking care of my daughters. I say a special thanks to my Dad for your loose education policy to make me what I am today. Most importantly, I appreciate the sacrifice and support of my lovely wife, Yidan and our daughters Jingshu (Iris) and Jiayue (Daisy). Yidan, you are the love of my life. You brought us the two little angels and supported me finishing this work. It is the destiny that ties us together and there is no one else could be better than you as my partner, thank you! To Jingshu (Iris), thank you for bringing me back from work and making me determined that I have to learn Dutch in my life. To Jiayue (Daisy), you are the second lovely little princess in our family and thank you for coming to us, I wish you grow up as well as your sister. I love you all!

To everyone who I unfortunately forgot to include above but contributed to my life, you mean no less to me. I appreciate you all.

<div align="right">Hao Shi</div>

University of Twente
March, 2019

CURRICULUM VITAE

Hao Shi

05-25-1989   Born in Donghai, China.

EDUCATION

2007–2011   B. E. in Refrigeration and Air-conditioning Engineering
Nanjing Institute of Technology, Nanjing

2011–2013   M. Sc. in Chemical and Energy Engineering
Otto-von-Guericke University Magdeburg, Magdeburg

2014–2019   PhD candidate at the Multi Scale Mechanics group
University of Twente, Netherlands
Thesis: Deformation of Cohesive Granular Materials:
Micro influences Macro
Promotor: Prof.dr.rer.-nat. S. Luding
Co-Promotor: Dr. V. Magnanimo

INDUSTRIAL EXPERIENCES

Utility Design Assistant in Roquette China Co., LTD., Lianyungang, China.

(July 2011- September 2011)

Research Engineer in MercuryLab B.V., Enschede, the Netherlands.

(September 2018 - Now)
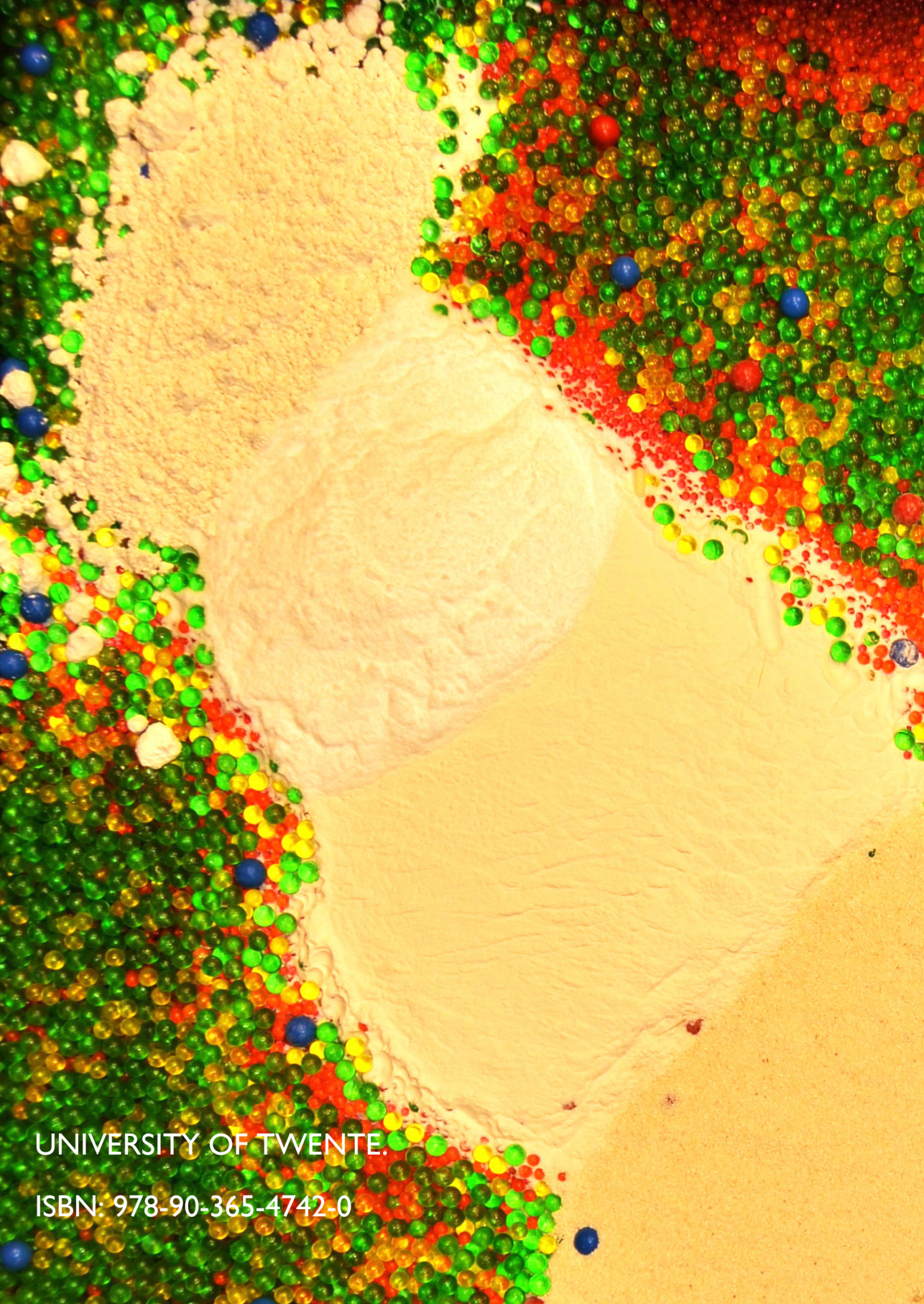
LIST OF PUBLICATIONS

JOURNAL PUBLICATIONS

- **Shi, H.**, Mohanty, R., Chakravarty, S., Cabiscol, R., Morgeneyer, M., Zetzener, H., Ooi, J.Y., Kwade, A., Luding, S. & Magnanimo, V. (2018). Effect of Particle Size and Cohesion on Powder Yielding and Flow. KONA Powder and Particle Journal, **35**, 226-250.

- **Shi, H.**, Roy, S., Weinhart, T., Magnanimo, V. & Luding, S. (2019). Steady State Rheology of Homogeneous and inhomogeneous cohesive granular materials. (*submitted in Aug. 2018*).

- **Shi, H.**, Lumay, G. & Luding, S. Stretching the limit of dynamic and quasi-static flow testing on limestone powders. (*Chapter 4, to be submitted*).

- Cabiscol, R., **Shi, H.**, Finke, J. H., Luding, S. & Kwade, A. Effect of particle size on powder compaction and tablet strength using limestone. (*Chapter 3, to be submitted*).

- Jarray A., **Shi, H.**, Scheper, B.J., Habibi, M. & Luding, S. Segregation in cohesive dry granular systems. (*to be submitted*).

- Ilhan B., **Shi, H.**, Duits, M.H.G. & Luding, S. Discontinuous shear thickening does not need hydrodynamic contributions. (*in preparation*).

- Triñanes, P. G., **Shi, H.**, Garg, V. & Luding, S. Tensile strength of cohesive powders. (*in preparation*).

CONFERENCE PROCEEDINGS

- **Shi, H.**, Singh, A., Luding, S., & Magnanimo, V. (2015). Numerical and experimental investigation of yielding for cohesive dry powder. In 8th International Conference for Conveying and Handling of Particulate Solids (CHOPS), Tel-Aviv, Israel.

- **Shi, H.**, Luding, S., & Magnanimo, V. (2016). Limestone Powders Yielding and Steady State Resistance under shearing with different testers. In 2nd International Conference on Powder, Granule and Bulk, Jaipur, India.

- **Shi, H.**, Luding, S., & Magnanimo, V. (2017). Steady state rheology from homogeneous and locally averaged simple shear simulations. In EPJ Web of Conferences (Vol. **140**, p. 03070). EDP Sciences.

- T. Weinhart, D. R. Tunuguntla, M. P. van S. Lantman, I. F. C. Denissen, C. R. Windows-Yule, H. Polman, J. F. M. Tsang, B. Jin, L. Orefice, K. van der Vaart, S. Roy, **H. Shi**, A. Pagano, W. den Breeijen, B. Scheper, S. Luding, A. Thornton. (2017). MercuryDPM: Fast, flexible particle simulations in complex geometries Part II: Applications, V International Conference on Particle-based Methods - Fundamentals and Applications, PARTICLES 2017.

BOOK CHAPTER

- **Shi, H.**, Vescovi, D., Singh, A., Roy, S., Magnanimo, V., & Luding, S. (2017). Granular Flow: From Dilute to Jammed States. In Granular Materials, edited by M. Sakellariou. InTech Open.